

Research on Rational Synthesis and Luminescence Properties of Oligo-Nuclear Complexes Using Linear Multidentate Ligands

都合, 達男

<https://doi.org/10.15017/1931707>

出版情報 : Kyushu University, 2017, 博士 (理学) , 課程博士
バージョン :
権利関係 :

Research on Rational Synthesis and Luminescence Properties of Oligo-Nuclear Complexes Using Linear Multidentate Ligands

Tatsuo Togo

March 2018

Department of Chemistry
Graduate School of Science
Kyushu University

Contents

General Introduction	1
Chapter 1	25
Structural Conversion and Selective Synthesis of Di- and Octa-nuclear Mn(II), Co(II) and Zn(II) Complexes	
Chapter 2	47
Synthesis and Luminescence Properties of Trinuclear Lanthanide Complexes with Linear Multidentate Ligands	
Chapter 3	79
Synthesis and Multi-Emission Properties of Lanthanide-Boron Hetero-Nuclear Complexes	
Concluding Remarks	139
Acknowledgement	141
List of Publications	142

General Introduction

1. Oligo-nuclear metal complex

1.1 Oligo-nuclear metal complex

Oligonuclear complexes contain multimetal ions. The distance between the metal ions is comparatively narrow. Hence, unique properties such as multi-electron transfer and large spin moment are expected due to strong metal to metal interactions. Oligonuclear complexes were first reported in the 1950s^{1,2} Eventually, this theme was developed by the report of metal-metal bonds³ and the confirmed theory of mixed valence complexes.⁴ Nowadays, the oligonuclear complexes are one of the most important research fields in coordination chemistry, and their magnetic properties have become a major research area. Manganese 12 nuclear complex bridged with a carboxylic acid is the first reported example of a single molecular magnet (SMM) by Novac⁵⁻⁷ (Fig. 1) This compound has a large spin moment $S=10$ and long relaxation time. Therefore, it acts as an SMM. After this discovery, many oligonuclear complexes have been reported as SMMs.

In addition, oligonuclear complexes may act as catalysts for intricate reactions such as multi-electron transfers. For example, in nature, it is known that a tetranuclear cluster comprising three manganese ions and one calcium ion acts as an active center for the oxygen generation reaction during photosynthesis in plants. Other examples include the generation of ammonia from nitrogen in the air by certain rhizobia. They contain enzymes called nitrogenase, which is involved in the generation of ammonia. The active center of nitrogenase is a tetranuclear iron cluster.

Oligonuclear complexes are also expected to be luminescent materials. It is reported that they develop luminescent properties owing to the formation of metal-metal bonds, and exhibit multicolor emission because of changing interactions. Ma et al. reported a platinum binuclear complex (BFPtPZ) that showed dual-emission.⁸ (Fig. 2) BFPtPZ has two stable excited states, where the Pt-Pt distances were different owing to structural conversion. These excited states have different energy gaps due to changing Pt-Pt interactions. Hence, this compound shows dual-emission.

In recent years, oligonuclear complexes have been used as sub-building units (SBUs) in metal organic frameworks (MOFs). Zhou et al. reported various kinds of functional MOFs composed of hexa-nuclear zirconium clusters as SBUs.⁹⁻¹³ Hexa-nuclear zirconium clusters have high stability. Furthermore, its bridged carboxylic acids

coordinate with regularity; therefore, it is easy to form rational structures and to add certain functions through ligand designs.

As described above, oligonuclear complexes are expected to be applicable in a variety of applications. Hence, this field has much scope for further development. Oligonuclear complexes can be grouped into two types based on the number of the kind of metal ions. A homo-oligonuclear complex is composed of only one kind of metal ion, while a hetero-oligonuclear complex is formed by two or more kinds of metal ions. Hetero-oligonuclear complexes are especially sought for various functional applications because each metal ions plays a different role in introducing specific properties such as electron transfer and photophysical properties.

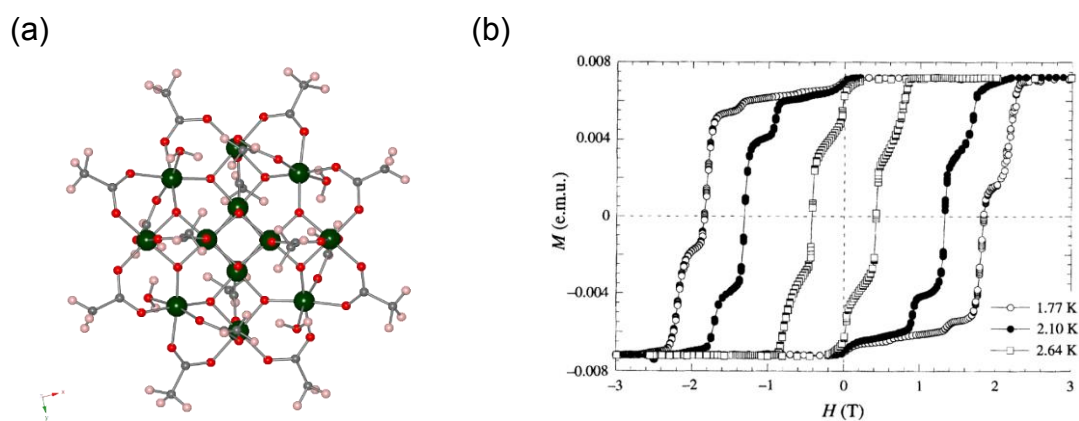


Fig. 1 (a) Crystal structure of $[\text{Mn}_{12}(\text{CH}_3\text{COO})_{16}(\text{H}_2\text{O})_4\text{O}_{12}]$ (b) Magnetization hysteresis loops with a SQUID magnetometer⁵⁻⁷.

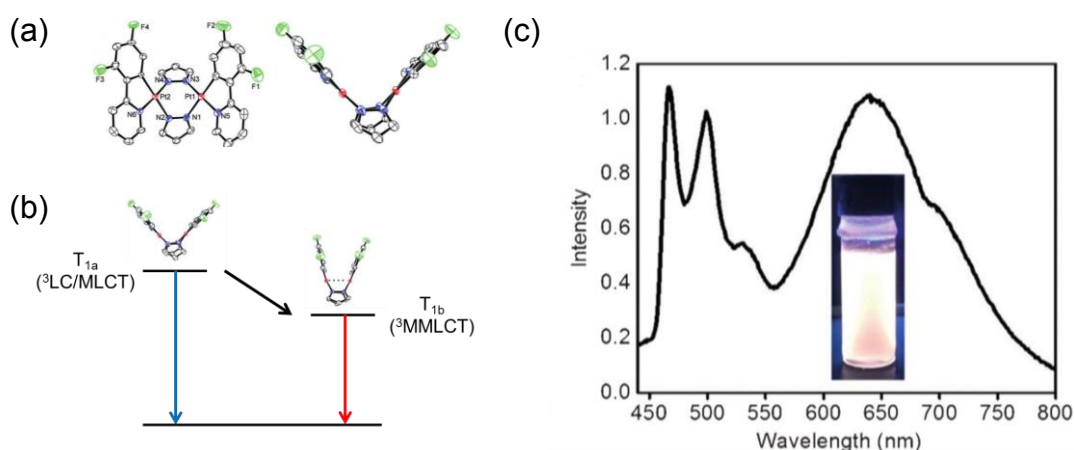


Fig. 2 (a) Molecular structure of BFpPtPZ. (b) Potential-energy curves and transitions for the molecular butterfly BFpPtPZ involving a photo-induced structural change owing to photo-induced Pt–Pt distance shortening, and the generation of dual emission. (c) The

normalized emission spectrum of BF₄PtPZ in CH₂Cl₂ at -77 °C. Inset: Photograph of the sample⁸.

In traditional research, oligonuclear complexes were synthesized by multidentate ligands that can form bridges. Their structure was then characterized by single crystal X-ray diffraction. This scheme was the general way for oligonuclear complexes research. However, developing functional oligonuclear complexes requires the formation of optional oligonuclear complex structures that enable the strict control of metal to metal distance. For creating rational structures of oligonuclear complexes, three kinds of methods have been reported. The first involves macrocyclic ligands. The second way is by using complex ligands. The third method is via bracket type ligands. These methods have been explained in detail in the subsequent sections.

1.2. Rational synthesis methods of oligonuclear complexes

1.2.1. Macrocyclic/macroacyclic ligand

Macrocyclic/macroacyclic ligand contains some circular multidentate sites. The macrocyclic ligand coordinates with metal ions in an enclosing manner and occupies almost all the coordination sites of the metal ions. Furthermore, macrocyclic ligands have some multidentate sites; hence, such ligands can encapsulate multimetal ions in one ligand. Rational synthesis of oligonuclear complexes is possible with this type of ligand. The reported macrocyclic ligands are usually Schiff-base frameworks such as salene derivatives¹⁴ and binuclear complexes with salene derivative ligands. Macrocyclic ligands have been reported since the 1980s. Vigato et al. wrote an extensive review about macrocyclic/macroacyclic ligands and their complexes¹⁴. The advantage of a macrocyclic ligand is that it is easy to predict the structure of the oligonuclear complex based on the structure of the macrocyclic ligand. However, these ligands have disadvantages as well. It is difficult to form tri- or more nuclear complexes, and multistep synthesis for macrocyclic ligands is necessary.

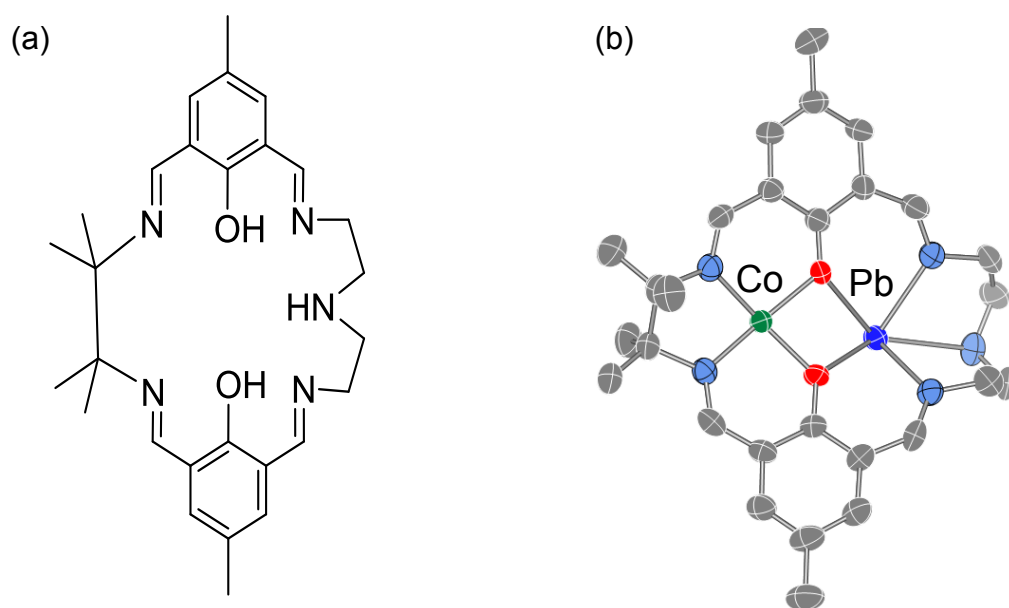


Fig. 3 (a) Macrocyclic ligand and **(b)** structure of a heterobinuclear complex $[\text{CoPb}(\text{L})]^{2-}$

15

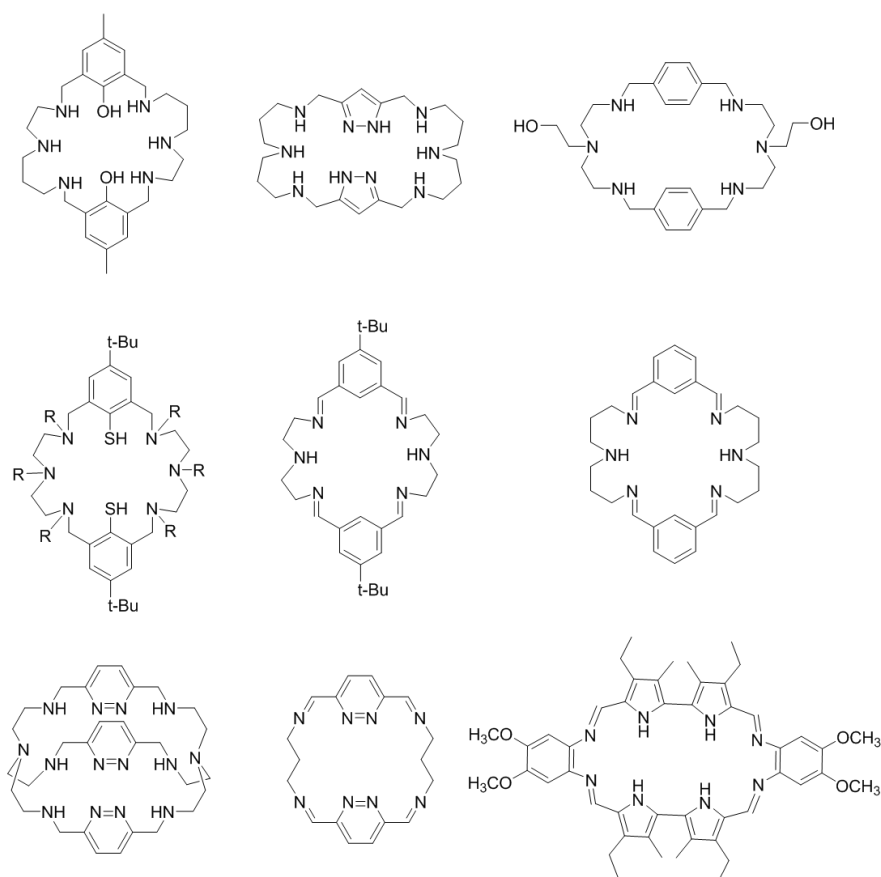


Fig. 4 Multinucleated macrocyclic Ligands¹⁴

1.2.2. Complex ligand

A complex ligand has extra coordination sites. Therefore, it can coordinate with other metal ions and form oligonuclear complexes. A copper complex was the first complex ligand to be reported, by Lippard in 1980.¹⁶ This complex has an imidazole site as the extra coordination site and coordinates with other copper ions to form binuclear complexes. Matsumoto et al. reported the synthesis of a supramolecular structure with complex ligands¹⁷⁻¹⁹ (Fig. 5). The synthesis of oligonuclear complexes with complex ligands is a multistep reaction. Therefore, it is easy to synthesize heterometal oligonuclear complexes. Sakai et al. reported platinum-ruthenium heterometal complexes and photohydrogen evolving reactions with single molecular structures²⁰ (Fig. 6). The ruthenium complex works as a photosensitizer and the platinum complex works as a hydrogen generation catalyst. Ruthenium and platinum complexes form a coupled photocatalyst system by connecting with each other.

The metal to metal distance in oligonuclear complexes formed with complex ligands is very large because this type of oligonuclear complex results from the gathering of mononuclear complexes rather than cluster complexes. Therefore, this type of oligonuclear complex tends to have weak metal to metal interactions.

Moreover, in this paper, complex ligands include all coordination compounds, not just metal ions, but also non-metal ions.

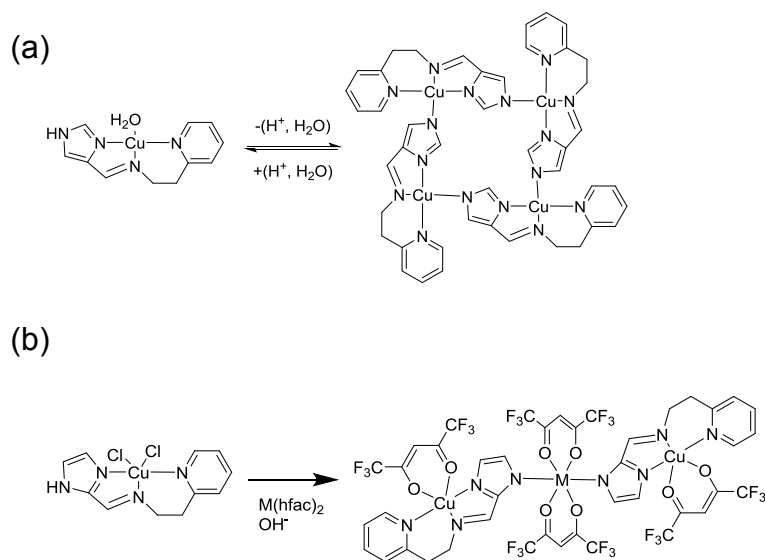


Fig. 5 (a) (b) Reaction scheme of Cu(II) complexes as a ligand complex to form oligonuclear complexes¹⁸.

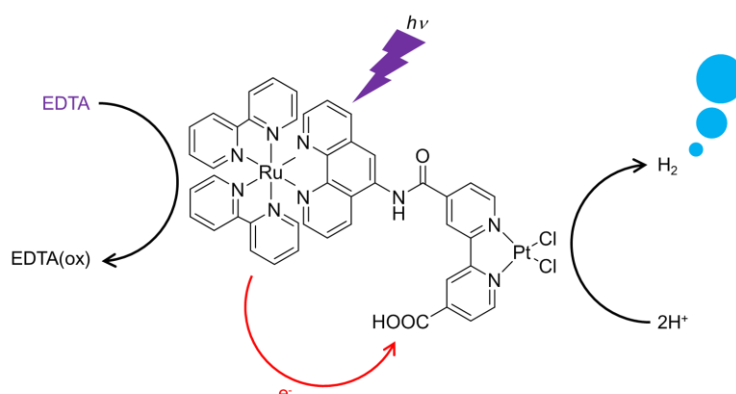
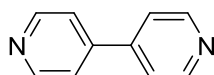


Fig. 6 Scheme of catalytic hydrogen generating reaction with Pt-Ru binuclear complex²⁰.

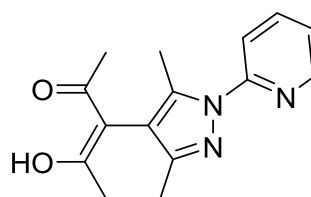
1.2.3. Bracket type ligand

A bracket type ligand has multicoordination sites and the angle between each coordination sites is fixed so as to form a bracket-like structure similar to those used for fixing between wooden frames in DIY models. This ligand coordinates with multiple metal ions because of multiple coordination sites. In addition, rational designs and the formulation of complicate structures is possible, such as a macroacyclic complex, cage type complex, grid type complex, and cluster type complex with apposite metal ions, on account of the fixed angle between each coordination site.

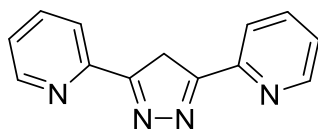
$n = 180^\circ$



$n = 120^\circ$



$n = 36^\circ$



$n = 0^\circ$

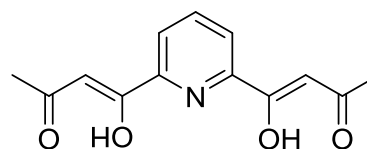


Fig. 7 Bracket type ligands²⁵⁻³⁰

Fijita et al. reported octahedron type palladium hexa-nuclear complex and its ability for guest encapsulation²¹. This complex was formed from palladium ion, the coordination site of which has square planar geometry and a tripyridyl ligand with a

triazine core. The angle between each pyridine site is fixed at 120° . Hence, they formed an octahedron structure. In addition to this, Fujita et al. also reported several kinds of polymorphic structures such as cage²², bowl,²³ and prism²⁴ with palladium ion and bracket type ligands.

Among the bracket type ligands, the ligand whose angle between each coordination site is fixed at 0° is called linear multidentate ligand. This type of ligand is expected to accommodate multiple metal ions spontaneously. Furthermore, one linear multidentate ligand cannot occupy the entire coordination site of the metal ions; consequently, one metal ion coordinates with two or more linear multidentate ligands. Therefore, it is easy to form bi- or multinuclear complexes with linear multidentate ligands.

Masaoka and Kawata et al. reported iron pentanuclear complex with 3,5-di(2-pyridyl) pyrazole and its oxygen revolution ability²⁵.

Ohba et al. reported 3d-4f-3d heterotrinnuclear complexes with linear multidentate ligands and its magnetic properties²⁶⁻³⁰ (Fig. 8). This ligand provides two kinds of metal binding sites, one is a central 2,6-diacetylpyridine site, one is two β -diketone sites at each end. This structure is available for arranging metal centers in difference coordination environments; therefore, 3d-4f-3d heterotrinnuclear complexes were selectively prepared using different ionic radii.

In Chapter 1, we present the rational synthesis of 3d oligonuclear complexes with linear multidentate ligands and their structural conversion. Here, one linear multidentate ligand H₂L was used. H₂L was previously reported by Ohba et al. In addition to the above characteristics, b-diketone sites can control their coordination ability by protonating or deprotonating. Hence, the structure of complexes can be controlled by controlling the pH. In acidic conditions, binuclear complexes were produced. However, in basic conditions, octa-nuclear complexes were produced. In addition, binuclear complexes were transformed to octa-nuclear complex by adding the basic solution. In Chapter 1, we discuss the structure and structural conversion in detail.

In Chapter 2, we report the synthesis of lanthanide trinnuclear complexes with ligand H₂L and its analogue and their luminescence properties. With respect to the lanthanide, we explain node 4 in detail.

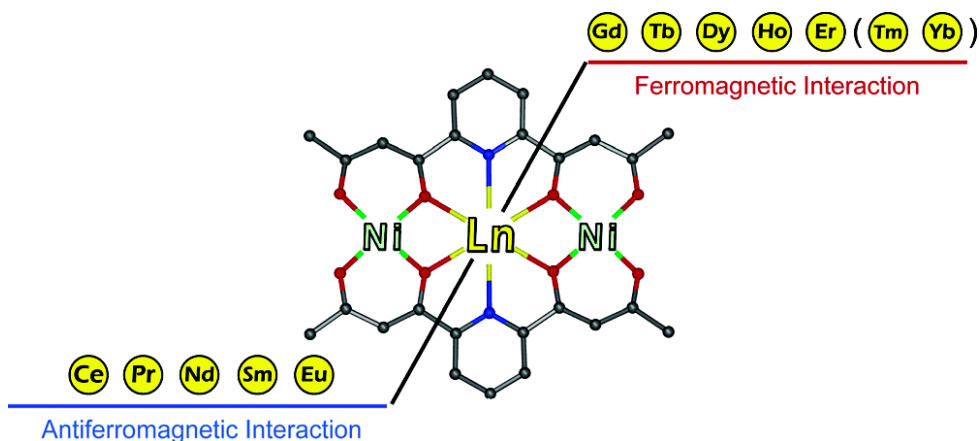


Fig. 8 Series of 3d-4f-3d heterotrimeric complexes²⁶⁻³⁰.

2. Luminescence

Luminescence is a phenomenon where a material that is given energy irradiates that energy as the light. Luminescence is classified by the given energy, such as electroluminescence (electron), photoluminescence (light), chemiluminescence (chemical reaction), bioluminescence (enzyme reaction, one kind of chemiluminescence in biosis), and radio luminescence (radioactivity).

All luminescence mechanisms are explained as follow. First, matter is supplied with energy. The energy state of this matter changes from ground state to excited state by obtaining that energy. The excited state is unstable for matter; hence, the energy state of matter goes back to ground state. Thereby, a portion of the energy is irradiated as light. This is a physical phenomenon; therefore, luminescence is in accordance with the law of conservation of energy. This is why irradiation energy is lower than the supplied energy.

The luminescence mechanism is classified into three types by transition processes. When matter is given energy, and goes to its excited state, and then goes back to ground state directly, the direction of the excited spin is same as ground state. At this condition, the spin angular momentum (S) is 0. This luminescence is a single transition process from singlet excited state to singlet ground state, called fluorescence. The characteristics of

fluorescence are high quantum yield because fluorescence is permitted transition, short emission lifetime (~nanosecond order) because this transition occurs quickly, and small Stokes shift, i.e., the difference between the positions of the peak top of absorption and emission spectra, because structural conversion by this transition is small.

Conversely, the other process is that the excited spin turns around, and then goes back to ground state. This transition process is a reaction, wherein a singlet excited state goes through triplet excited state by intersystem crossing, and then the electron goes back to the singlet ground state. This luminescence process is called phosphorescence. The quantum yield of phosphorescence is relatively low because the transition from the triplet excited state to the singlet ground state is a forbidden process. However, this tendency does not apply in the case of complexes or inorganic materials with heavy metal ions such as lanthanide, rhenium, and iridium. Therefore, it is difficult to turn the direction of the spin. Hence, the emission lifetime is long (~millisecond order). In addition to these characteristics, the Stokes shift is long as spin multiplicity is changed during the transition process, and structural conversion by this transition is large.

Finally, the third luminescence process is called delayed fluorescence. This process is the combination of fluorescence and phosphorescence. First, the electron is excited to singlet excited state, and then translated to triplet excited state by intersystem crossing as in phosphorescence. After this, electron goes back to the singlet excited state by thermal activation. Then, the electron returns to the singlet ground state. Superficially, the emission mechanism appears to be fluorescence, but this process goes through the triplet excited state once. Hence, this transition process is classified as the third emission process. The emission lifetime of delayed fluorescence is longer than that of fluorescence.

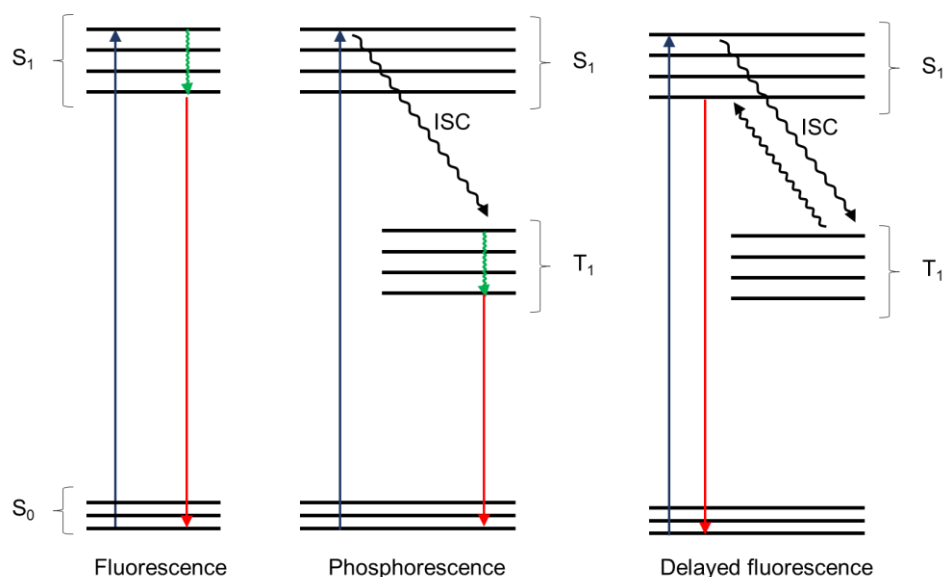


Fig. 9 Mechanism scheme of fluorescence, phosphorescence, and delayed fluorescence.

Not just humans, rather most species obtain much of the information through their eyes. The eye is a sensory apparatus that receives light. Specifically, light is the easiest stimulation for us. Hence, luminescence materials are applied in various fields. For example, for portraying information, liquid crystal displays or neon lights are applied in the information industry. In particular, owing to increased demand for smartphones in recent years, the development of a light emitting diode based on organic compound (OLED) has been initiated. Adachi et al. reported quite high efficiency Electro Luminescence (EL) materials with delayed fluorescence³¹. Moreover, for identifying the location of cancers or monitoring their growth, luminescence materials are applied in medicine or biotechnology. This technology was developed immensely via the research pertaining to green fluorescent protein (GFP)³²⁻³⁴ by Shimomura, Chalfie, and Taisen et al. This research received a noble prize in 2008.

GFP was isolated from *Aequorea Victoria*. As evidenced by this example, several kinds of species apply luminescence in their lives. The well-known male firefly exhibits luminescence in its own body to communicate with the female. Some football fish keep luminous bacteria at the end of the illicium (like a fish rod). They use luminescence to get food such as fish. Some fish use luminescence to protect themselves. One fish demonstrated emission at the bottom of their bodies to simulate the light of the sun. Other fish used luminescence as a dazzler to escape. Thus, luminescence is important for animals as well.

There are many kinds of luminescent material such as organic, inorganic compounds, coordination compounds (organic-inorganic hybrids), carbon materials (graphene, fullerene), quantum dots, proteins, and so on. In this paper, we focus on luminescent molecules like organic compounds, and molecularly coordination compounds. The advantage of luminescent molecular materials is availability in numerous states such as powder, thin film, and solution. Furthermore, its luminescent property is controllable by molecular design and modification.

3. Sensing with luminescence

3.1. Chromism

Chromism is a process by which photophysical properties (absorption wavelength, emission wavelength, and so on) are changed by some external stimuli. Chromism was classified based on external stimuli as photochromism (light)³⁵, thermochromism (temperature, heat)^{36, 37}, electrochromism (electron)^{38, 39}, mechanochromism (mechanical force such as grinding, crushing and milling)⁴⁰⁻⁴², solvatochromism (solvent molecular)⁴³⁻⁴⁵, piezochromism (pressure)^{46, 47}, vapochromism (vapor of organic compounds or gas),⁴⁸⁻⁵⁰ ionochromic (ions)⁵¹, and halochromism (pH)⁵².

Chromic materials change the appearance color or emission color by external stimuli. Hence, the change of external stimuli is intuitively recognizable by observing the color change. Thus, chromic materials are applicable for sensing or imaging materials. For example, relating to luminous chromic materials, Hasegawa et al. reported lanthanide luminous thermochromic coordination polymer (CP)³⁷. This lanthanide CP showed green emission below 250 K, yellow emission below 300 K, orange emission below 350 K, and red emission above 400 K (Fig. 10 (a)). Additionally, Ito et al. reported mechanochromic gold complexes⁴⁰. This complex changed emission colors from blue to yellow by scratching or grinding (Fig. 10 (b)).

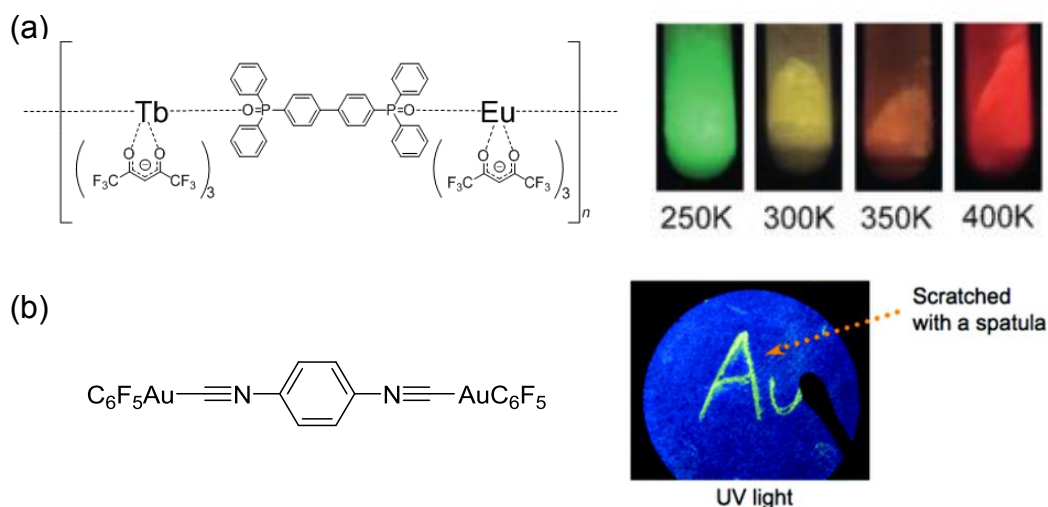


Fig. 10 (a) Lanthanide coordination polymer with thermochromic property. **(b)** Gold complex with mechanochromic property^{37,40}.

3.2. Sensing with luminous materials

Sensing with luminous materials is applied in various fields, especially medicine and analysis. Nowadays, two types of luminous sensing are applied. One is the evaluation with emission intensity. The other is the evaluation with emission color showing luminous chromism. To evaluate using emission color change with chromic materials is much easier than to evaluate using the change of emission intensity. However, previously reported chromic materials mainly exhibited low color change. Therefore, chromic materials that can change their colors dramatically are desired

4. Luminous compounds

4.1. Lanthanide complexes

4.1.1. Lanthanide

Lanthanides are a series of the chemical elements that constitutes fifteen metallic chemical elements with atomic numbers between 57 through 71, i.e., from lanthanum to lutetium. Lanthanide has been labeled as group 3 element in the periodic table. The lanthanide ion is generally stable as a trivalent cation. The general electron configuration is expressed as below.

$$\text{Ln}^{3+} = [\text{Kr}](4d)^{10}(4f)^n(5s)^2(5p)^6 \quad (n = 0-14)$$

It is clear from the electron configuration of lanthanide trivalent ion that the

unoccupied 4f orbital is shielded by the occupied 5s and 5p orbitals. This is the most important characteristic which determines the physical properties of lanthanide ions. The radius of the 4f orbital is smaller than those of 5s and 5p orbitals. However, the energy of the 4f orbital is higher than the energies of the 5s and 5p orbitals. Therefore, the 5s and 5p orbitals are filled before the 4f orbital. Owing to this shielding effect by the occupied 5s, 5p orbitals, the 4f orbital is insulated from the influence of the surrounding environment such as ligands, solvents, and gases. Lanthanide ions have two physical properties due to the shielding effect. One is that the electronic interaction of the ligand is larger than the orbital interaction when lanthanide forms the coordination bonds. The other is that physical properties of lanthanide ions such as photophysical properties and magnetic properties are not changed by the surrounding environment.

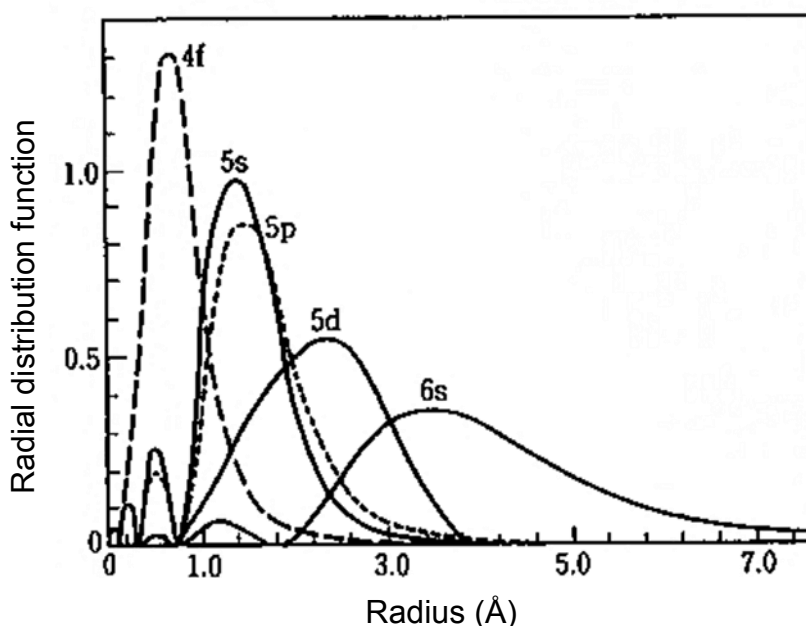


Fig. 11 Radius of 4f, 5s, 5p, 5d, and 6s orbital⁵³

4.1.2. Luminescence property of lanthanide ion

The excitation process and electron transition related to the luminescent process of trivalent lanthanide ion is caused in the 4f orbital. In other words, this process is an f-f transition. The structural conversion between ground state and excited state is small because the f-f transition is caused in only the 4f orbital. Therefore, Stokes shift of the

f-f transition is quite small. In addition, the half width of the luminescence spectrum is very small, less than 10 nm, the shape of spectrum is sharp, and color purity is high. Furthermore, the 4f orbital is not split by changing the surrounding environment, such as the coordination fields, owing to the shielding effect. Hence, emission wavelength has a specific value for each kind of lanthanide ions. Dieke et al. reported about the energy terms of lanthanide ions⁵⁴. They researched the energy levels of lanthanide chloride. The table below is called Dieke's diagram, which is one of the important sources of information to identify photophysical properties of lanthanide ions (Fig. 12).

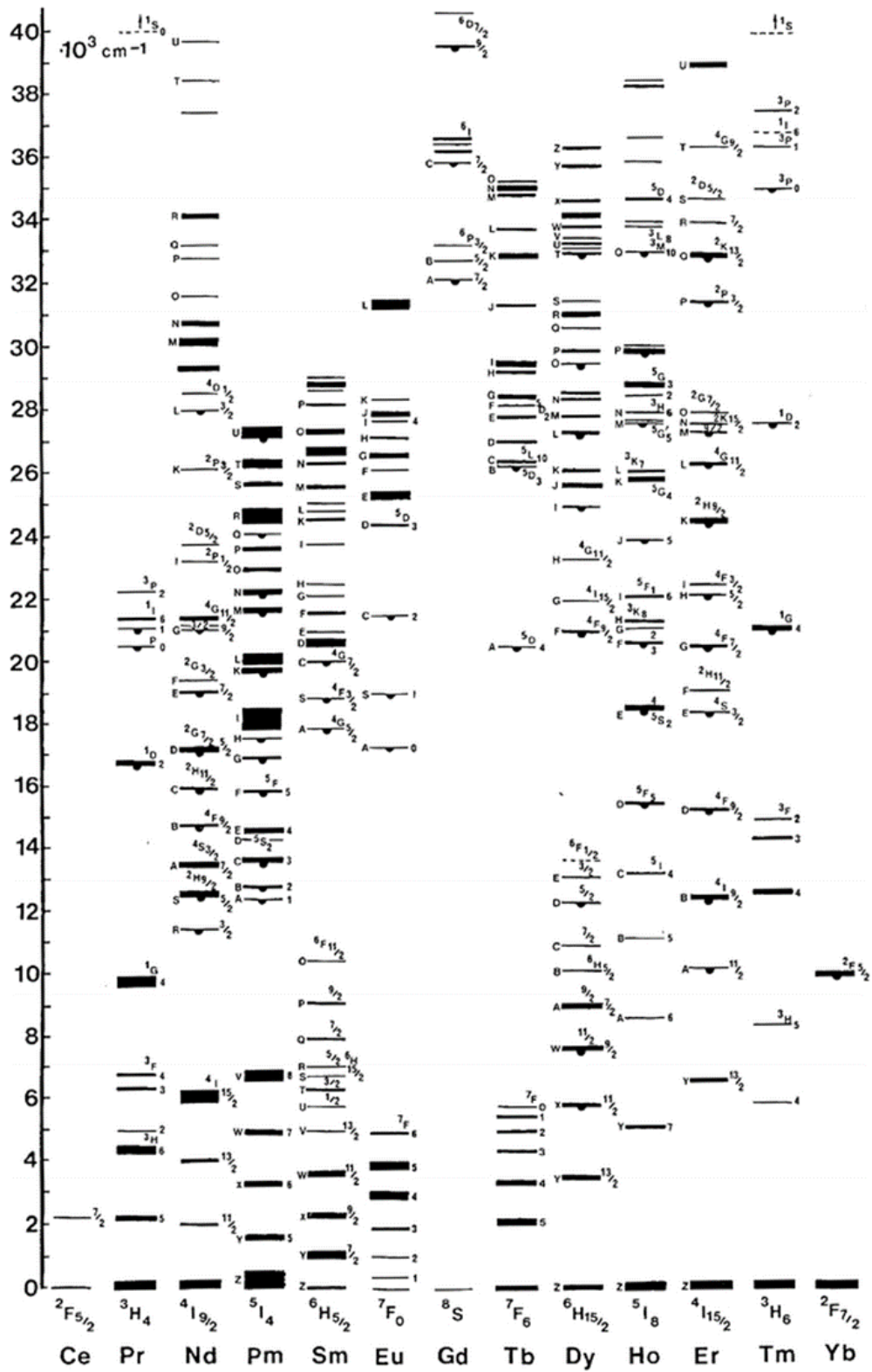


Fig. 12 Dieke's Diagram⁵⁴

4.1.3 Luminescent properties of lanthanide complex

The emission wavelengths of lanthanide complexes have specific values for each kind of lanthanide ions due to the shielding effect. However, the luminescence efficiency of lanthanide complexes is generally much higher than that of lanthanide ions with photoluminescent properties. The reason behind the increased luminescence efficiency is due to the difference of absorption efficiency between lanthanide ions and organic compounds. The molar absorptivity of lanthanide ions is less than $10 \text{ M}^{-1} \text{ cm}^{-1}$. In contrast, the molar absorptivity of organic compound is $10^3\text{--}10^5 \text{ M}^{-1} \text{ cm}^{-1}$. Organic ligands receive energy which gains with photon absorption by lanthanide ions by energy transfer in lanthanide complexes. Lanthanide complexes showed strong emission because the absorption efficiency of an organic ligand is higher and the excited energy is transferred from the organic ligand to the lanthanide ion. This effect is called antenna effect. Owing to antenna effect, the emission peak top of lanthanide complex is different from its absorption peak top. Therefore, unlike lanthanide ions, the Stokes shift of lanthanide complex is large.

The emission process of lanthanide complexes in photoluminescence is explained below. First, an organic ligand whose absorption efficiency is high is excited to its singlet excited state by photoabsorption. Then, the energy state transfers to the triplet excited state by intersystem crossing in energy level of the ligand. The transition rate of intersystem crossing is generally low because this transition is a forbidden process. However, this rate in lanthanide complexes is high owing to the heavy atom effect of lanthanide ions. After intersystem crossing, the energy is transferred from the triplet excited states of the ligand to the triplet excited states of lanthanide ion. At last, the excited energy goes back to the ground state, thereby the lanthanide complex displays luminescence. In this process, two non-radiative transitions are expected. One is from the excited states of the ligand. The organic compound has a lot of covalent bond. Some covalent bond, such as C-H and O-H vibrate at low energy. Therefore, excited energy is consumed by bond vibration. The other non-radiative transition is the energy transfer process from ligand to lanthanide. If the energy gap between triplet excited state of the ligand and that of the lanthanide ion is small, back energy transfer from lanthanide ion to ligand is caused. Therefore, the emission of lanthanide is quenched.

To inhibit these quenching mechanisms, the luminescence efficiency of lanthanide complex is controllable. Yanagita et al. reported Nd(III) complexes with rigid β -diketone ligands⁵⁵. Nd(III) ion showed emission in infrared regions; therefore, Nd(III) complex had shown no emission in organic solvents. This rigid ligand was composed of low vibrational C-D and C-F bonds. Consequently, this Nd(III) complexes showed emissions

in organic solvent (Fig. 13 (b)).

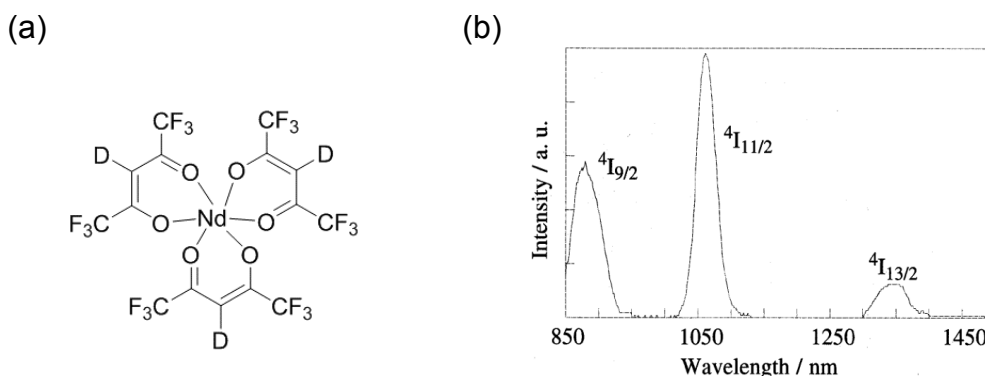


Fig. 13 (a) Chemical structure of Nd(III) complex with rigid β -diketone ligands. **(b)** Emission spectra of Nd(III) complex in acetone- d_6 ; excitation at 585 nm⁵⁵.

In Chapter 2, we discussed the rational synthesis of the trinuclear lanthanide complexes and controlling their luminescent property by ligand design. We used the same ligand H₂L as in Chapter 1 and synthesized tri-nuclear lanthanide complexes. Furthermore, we synthesized another ligand H₂L^F modified H₂L of CH₃ moieties to CF₃ moieties at the end of β -diketone sites. Similar trinuclear structure was formed with H₂L^F and trivalent europium ions. The emission efficiency of europium complex with H₂L^F is much higher than that of europium complex with H₂L, so as to inhibit the non-radiative transition in the ligand. In Chapter 2, we explained the detailed structure and luminescent properties of trinuclear lanthanide complexes.

4.2. Boron complex

4.2.1. Boron

Boron is a chemical element with atomic number 5, and is a group 3 element. The electronic configuration of boron atom is expressed as below.

$$B = [\text{He}](2s)^1(2p)^1$$

Boron atom has an unoccupied p orbital. Therefore, the covalent boron compounds called organoboron compounds have reported some interesting luminescence or electronic properties owing to the extension of the conjugated π -orbitals by unoccupied p orbitals. However, organoboron compounds have problem related to stability.

4.2.2. Boron complex

Trivalent boron ions form coordination bonds with bidentate ligands. This boron complex is reported to have high stability to moisture, oxygen, and photons. Furthermore,

the boron complex is also reported to show excellent optical properties owing to the extension of the π conjugated bonds and forming rigid π frameworks. A typical boron complex is BODIPY with a dipyrromethene framework and its analogs. BODIPY dyes have high quantum yields (normally between 60 and 90%), large molar absorptivity (typically being in the region of $40000\text{--}110000\text{ M}^{-1}\text{ cm}^{-1}$), sharp bands in the absorption spectra, small Stokes shift, low solvatochromic property because of electric dipole moment and dipole transition are at right angles to each other, and excellent chemical and photochemical stability in any state. In addition, its optical properties are controllable by modifying dipyrromethene frameworks⁵⁶⁻⁵⁸.

BODIPY has been reported on applied research such as introduction into living cells as well as photophysical properties because of its excellent stabilities.⁵⁹ Similarly, other type of boron complexes, i.e., boron complexes with β -diketonate analogs, such as β -diketonate, ketoiminate, and diiminate have been also reported⁶⁰. These compounds demonstrated excellent optical properties. Furthermore, their frameworks are easier to synthesize than BODIPY frameworks. Thus, boron complexes with β -diketonate and its analogs have been extensively researched in recent years.

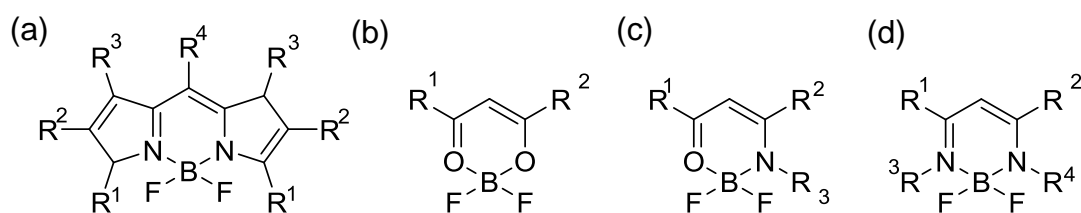


Fig. 14 Chemical structure of (a) F-bodipy, (b) boron diketonate, (c) boron ketoiminate, and (d) boron diiminate frameworks⁵⁶⁻⁶⁰

4.2.3. Boron complex ligand

A boron complex which has extra coordination sites is known as a boron complex ligand. Already, certain BODIPY compounds with coordination sites have been reported. However, these BODIPY compounds were applied as ion sensors by changing the optical property of BODIPY with coordination. However, metal ions or complexes also have unique physical properties such as emission and redox. Therefore, the boron metal heteronuclear complex has potential for new luminescence materials. Unique optical properties such as multiemission and emission color change are anticipated by designing structures to combine both excellent optical properties of the boron complex and metal complex.

Some preceding examples of boron metal hetero-oligonuclear complexes with boron complex ligand were reported. Marder et al. reported Rh(III) or Ir(III) complexes with boron complex containing 2,2'-bipyridine moieties as coordination sites⁶¹. These chromophores exhibit large third-order polarisabilities at 1.55 μm , while retaining good film-forming properties and linear optical transparency in the near infrared region.

Chujo et al. reported a platinum-boron heterobinuclear complex⁶². This complex was synthesized such that the platinum binuclear complex replaced one platinum ion with one boron ion. This heterobinuclear complex showed dual emission properties due to the platinum and boron complexes.

Furthermore, Neamati et al. reported that ferrocenyl chalcone difluoridoborates worked as an inhibitor for HIV-1 integrase⁶³. Maeda et al. reported ion pairs with platinum complexes and boron complexes⁶⁴.

As described above, boron metal heteronuclear complexes with boron complex ligands are new materials that are expected to provide unique properties.

In Chapter 3, we proposed new concepts of the boron metal heteronuclear complex. We chose lanthanide ions as the metal ions, and prepared boron lanthanide heteronuclear complexes. These complexes showed dual emission from lanthanide ions and boron complexes. Furthermore, these compounds showed concentration and solvent dependent luminescent properties. Boron lanthanide heteronuclear complexes are novel color tunable materials. In Chapter 3, we describe the synthesis, characteristics, and luminescence properties of boron lanthanide heteronuclear complexes.

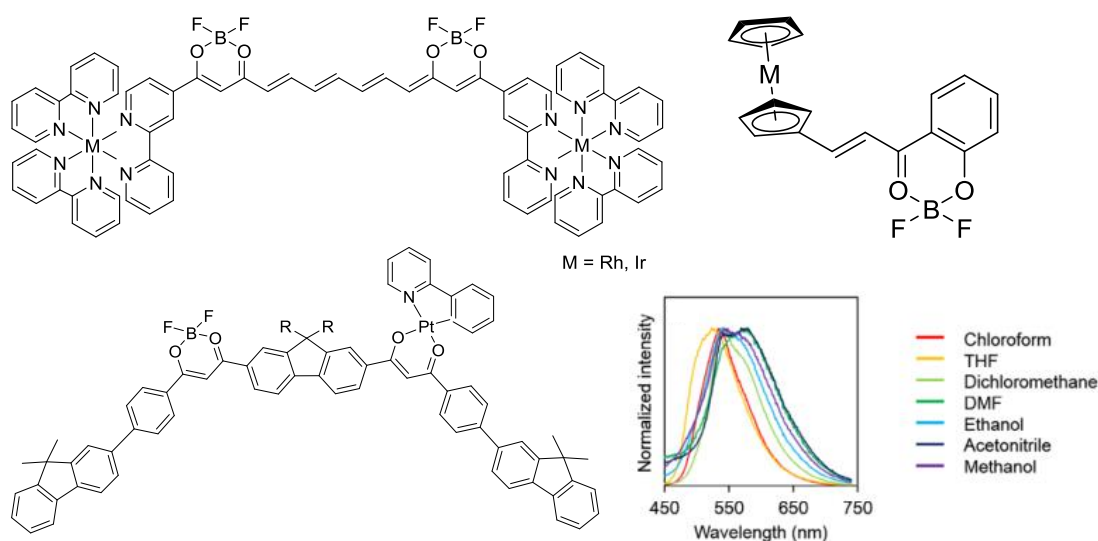


Fig. 15 Boron-metal hetero nuclear complexes and luminescence spectra of Boron-Pt hetero nuclear complex⁶¹⁻⁶⁴

References

1. J. Chatt and F. A. Hart, *Nature*, 1952, **169**, 673-674.
2. J. Chatt, L. A. Duncanson, F. A. Hart and P. G. Owston, *Nature*, 1958, **181**, 43-44.
3. F. Taha and G. Wilkinson, *Journal of the Chemical Society (Resumed)*, 1963, 5406-5412.
4. M. B. Robin and P. Day, in *Advances in Inorganic Chemistry and Radiochemistry*, eds. H. J. Emeléus and A. G. Sharpe, Academic Press, 1968, vol. 10, pp. 247-422.
5. R. Sessoli, D. Gatteschi, A. Caneschi and M. A. Novak, *Nature*, 1993, **365**, 141.
6. L. Thomas, F. Lioni, R. Ballou, D. Gatteschi, R. Sessoli and B. Barbara, *Nature*, 1996, **383**, 145-147.
7. T. Lis, *Acta Crystallographica Section B-Structural Science*, 1980, **36**, 2042-2046.
8. M. G. Han, Y. Tian, Z. Yuan, L. Zhu and B. W. Ma, *Angew. Chem. Int. Ed.*, 2014, **53**, 10908-10912.
9. Y. Bai, Y. Dou, L.-H. Xie, W. Rutledge, J.-R. Li and H.-C. Zhou, *Chemical Society Reviews*, 2016, **45**, 2327-2367.
10. Z. Wei, Z.-Y. Gu, R. K. Arvapally, Y.-P. Chen, R. N. McDougald, J. F. Ivy, A. A. Yakovenko, D. Feng, M. A. Omary and H.-C. Zhou, *J. Am. Chem. Soc.*, 2014, **136**, 8269-8276.
11. B. Wang, X.-L. Lv, D. Feng, L.-H. Xie, J. Zhang, M. Li, Y. Xie, J.-R. Li and H.-C. Zhou, *J. Am. Chem. Soc.*, 2016, **138**, 6204-6216.
12. S. Yuan, L. Zou, H. Li, Y.-P. Chen, J. Qin, Q. Zhang, W. Lu, M. B. Hall and H.-C. Zhou, *Angew. Chem. Int. Ed.*, 2016, **55**, 10776-10780.
13. J. Park, Q. Jiang, D. Feng and H.-C. Zhou, *Angew. Chem. Int. Ed.*, 2016, **55**, 7188-7193.
14. P. Guerriero, S. Tamburini and P. A. Vigato, *Coord. Chem. Rev.*, 1995, **139**, 17-243.
15. H. Furutachi, S. Fujinami, M. Suzuki and H. Okawa, *Journal of the Chemical Society, Dalton Transactions*, 2000, 2761-2769.
16. R. N. Katz, G. Kolks and S. J. Lippard, *Inorg. Chem.*, 1980, **19**, 3845-3847.
17. N. Matsumoto, K. Inoue, H. Okawa and S. Kida, *Chemistry Letters*, 1989, **18**, 1251-1254.
18. Y. Sunatsuki, Y. Motoda and N. Matsumoto, *Coord. Chem. Rev.*, 2002, **226**, 199-209.
19. N. Matsumoto, Y. Mizuguchi, G. Mago, S. Eguchi, H. Miyasaka, T. Nakashima and J.-P. Tuchagues, *Angewandte Chemie International Edition in English*, 1997,

- 36**, 1860-1862.
20. H. Ozawa, M. A. Haga and K. Sakai, *J. Am. Chem. Soc.*, 2006, **128**, 4926-4927.
 21. M. Fujita, D. Oguro, M. Miyazawa, H. Oka, K. Yamaguchi and K. Ogura, *Nature*, 1995, **378**, 469.
 22. M. Tominaga, K. Suzuki, M. Kawano, T. Kusukawa, T. Ozeki, S. Sakamoto, K. Yamaguchi and M. Fujita, *Angew. Chem. Int. Ed.*, 2004, **43**, 5621-5625.
 23. M. Fujita, S.-Y. Yu, T. Kusukawa, H. Funaki, K. Ogura and K. Yamaguchi, *Angew. Chem. Int. Ed.*, 1998, **37**, 2082-2085.
 24. K. Kumazawa, K. Biradha, T. Kusukawa, T. Okano and M. Fujita, *Angewandte Chemie*, 2003, **115**, 4039-4043.
 25. M. Okamura, M. Kondo, R. Kuga, Y. Kurashige, T. Yanai, S. Hayami, V. K. K. Praneeth, M. Yoshida, K. Yoneda, S. Kawata and S. Masaoka, *Nature*, 2016, **530**, 465.
 26. T. Shiga, M. Ohba and H. Ōkawa, *Inorg. Chem. Commun.*, 2003, **6**, 15-18.
 27. T. Shiga, T. Nakanishi, M. Ohba and H. Ōkawa, *Polyhedron*, 2005, **24**, 2732-2736.
 28. T. Shiga, N. Ito, A. Hidaka, H. Ohkawa, S. Kitagawa and M. Ohba, *Inorg. Chem.*, 2007, **46**, 3492-3501.
 29. T. Shiga, H. Okawa, S. Kitagawa and M. Ohba, *J. Am. Chem. Soc.*, 2006, **128**, 16426-16427.
 30. T. Shiga, M. Ohba and H. Okawa, *Inorg. Chem.*, 2004, **43**, 4435-4446.
 31. H. Uoyama, K. Goushi, K. Shizu, H. Nomura and C. Adachi, *Nature*, 2012, **492**, 234.
 32. O. Shimomura, F. H. Johnson and Y. Saiga, *Journal of cellular and comparative physiology*, 1962, **59**, 223-239.
 33. M. Ormö, A. B. Cubitt, K. Kallio, L. A. Gross, R. Y. Tsien and S. J. Remington, *Science*, 1996, **273**, 1392-1395.
 34. M. Chalfie, Y. Tu, G. Euskirchen, W. Ward and D. Prasher, *Science*, 1994, **263**, 802-805.
 35. M. Irie, *Chemical Reviews*, 2000, **100**, 1685-1716.
 36. D. R. Bloomquist and R. D. Willett, *Coord. Chem. Rev.*, 1982, **47**, 125-164.
 37. K. Miyata, Y. Konno, T. Nakanishi, A. Kobayashi, M. Kato, K. Fushimi and Y. Hasegawa, *Angew. Chem. Int. Ed.*, 2013, **52**, 6413-6416.
 38. P. M. Beaujuge and J. R. Reynolds, *Chemical Reviews*, 2010, **110**, 268-320.
 39. H. Sun, S. Liu, W. Lin, K. Y. Zhang, W. Lv, X. Huang, F. Huo, H. Yang, G. Jenkins, Q. Zhao and W. Huang, *Nature communications*, 2014, **5**, 3601.
 40. H. Ito, T. Saito, N. Oshima, N. Kitamura, S. Ishizaka, Y. Hinatsu, M. Wakeshima,

- M. Kato, K. Tsuge and M. Sawamura, *J. Am. Chem. Soc.*, 2008, **130**, 10044-10045.
41. Z. Chi, X. Zhang, B. Xu, X. Zhou, C. Ma, Y. Zhang, S. Liu and J. Xu, *Chemical Society Reviews*, 2012, **41**, 3878-3896.
 42. F. Ciardelli, G. Ruggeri and A. Pucci, *Chemical Society Reviews*, 2013, **42**, 857-870.
 43. F. Terenziani, A. Painelli, C. Katan, M. Charlot and M. Blanchard-Desce, *J. Am. Chem. Soc.*, 2006, **128**, 15742-15755.
 44. E. Buncel and S. Rajagopal, *Acc. Chem. Res.*, 1990, **23**, 226-231.
 45. K. M.-C. Wong and V. W.-W. Yam, *Acc. Chem. Res.*, 2011, **44**, 424-434.
 46. X. Zhang, Z. Chi, H. Li, B. Xu, X. Li, W. Zhou, S. Liu, Y. Zhang and J. Xu, *Chem. Asian J.*, 2011, **6**, 808-811.
 47. M. S. Kwon, J. Gierschner, S.-J. Yoon and S. Y. Park, *Adv. Mater.*, 2012, **24**, 5487-5492.
 48. O. S. Wenger, *Chemical Reviews*, 2013, **113**, 3686-3733.
 49. X. Zhang, B. Li, Z.-H. Chen and Z.-N. Chen, *J. Mater. Chem.*, 2012, **22**, 11427-11441.
 50. M. Kojima, H. Taguchi, M. Tsuchimoto and K. Nakajima, *Coord. Chem. Rev.*, 2003, **237**, 183-196.
 51. I. Welterlich and B. Tieke, *Macromolecules*, 2011, **44**, 4194-4203.
 52. J.-Y. Jaung, *Dyes and Pigments*, 2006, **71**, 245-250.
 53. G. Adachi, *Science of Rare Earths*, 1999.
 54. G. H. Dieke and H. M. Crosswhite, *Appl. Opt.*, 1963, **2**, 675-686.
 55. Y. Hasegawa, M. Iwamuro, K. Murakoshi, Y. Wada, R. Arakawa, T. Yamanaka, N. Nakashima and S. Yanagida, *Bulletin of the Chemical Society of Japan*, 1998, **71**, 2573-2581.
 56. G. Ulrich, R. Ziessel and A. Harriman, *Angew. Chem. Int. Ed.*, 2008, **47**, 1184-1201.
 57. N. Boens, V. Leen and W. Dehaen, *Chemical Society Reviews*, 2012, **41**, 1130-1172.
 58. A. Loudet and K. Burgess, *Chemical Reviews*, 2007, **107**, 4891-4932.
 59. A. Kamkaew, S. H. Lim, H. B. Lee, L. V. Kiew, L. Y. Chung and K. Burgess, *Chemical Society Reviews*, 2012, **42**, 77-88.
 60. K. Tanaka and Y. Chujo, *NPG Asia Mater.*, 2015, **7**, e223.
 61. H.-C. Lin, H. Kim, S. Barlow, J. M. Hales, J. W. Perry and S. R. Marder, *Chem. Commun.*, 2010, **47**, 782-784.
 62. A. Hirose, K. Tanaka, K. Tamashima and Y. Chujo, *Tetrahedron Letters*, 2014, **55**,

6477-6481.

63. J.-P. Monserrat, R. I. Al-Safi, K. N. Tiwari, L. Quentin, G. G. Chabot, A. Vessi res, G. Jaouen, N. Neamati and E. A. Hillard, *Bioorganic & Medicinal Chemistry Letters*, 2011, **21**, 6195-6197.
64. R. Sekiya, Y. Tsutsui, W. Choi, T. Sakurai, S. Seki, Y. Bando and H. Maeda, *Chem. Commun.*, 2014, **50**, 10615-10618.

Chapter 1

Structural Conversion and Selective Synthesis of Di- and Octa-nuclear Mn(II), Co(II) and Zn(II) Complexes

Abstract

A linear multidentate type ligand (H_2L) was prepared two types of oligo-nuclear complexes, di-nuclear complexes ($M_2(HL)_2$) and octa-nuclear complexes (M_8L_6) with divalent 3d transition ions ($M = Mn, Zn, \text{ and } Co$). These compounds were synthesized selectively by adjusting pH. Di-nuclear complex was obtained in acidic condition. Octa-nuclear complex was obtained in basic condition. The structure of $M_2(HL)_2$ was consist of two metal ions, two half-deprotonated ligands (HL^-), two nitrate anions, and two coordination solvents. The structure of M_8L_6 was composed of eight metal ions and six full-deprotonated ligands (L^{2-}). All compounds were characterized by FT-IR spectrum, UV-vis spectrum, elemental analysis, and single X-ray diffraction. $M_2(HL)_2$ was transformed to M_8L_6 by adding the base in solution state. Moreover, irreversible conversion of $M_2(HL)_2$ to M_8L_6 in response to the base addition in solution state was confirmed with UV-vis spectra.

Introduction

Oligo-nuclear complexes have attracted significant attention because of their catalytic^{1, 2}, magnetic³⁻⁶, and emission⁷ properties. Oligo-nuclear complexes consist of multi metal ions, and each metal ions interact with other metal ions. Therefore, some of them exhibit interesting physical properties not found in mono-nuclear complexes, for example exchange interaction, multi electron transfer, generation of mixed valence complexes, and intermetallic energy transfer.

M.A. Novak et.al. reported Mn₁₂ cluster complex had large spin angular moment ($S=10$) and showed SMM properties.^{3, 4, 8} These unique properties of oligo-nuclear complexes are strongly correlated to their structures. However, structures of oligo-nuclear complexes are complicated; hence it is difficult to construct the desired structures.

To control the arrangement of metal ions, several rational synthetic methods have been reported that use macrocyclic ligands⁹, complex ligands¹⁰, and multidentate ligands¹¹⁻¹⁴.

This paper suggests a new rational method for designing oligo-nuclear complexes and structural control. Using the linear multidentate ligands. This ligand has some multidentate sites linearly, so has an ability to coordinate with some metal ions. Furthermore, metal ions which are coordinate with a linear multidentate ligand have some uncoordinated sites, then coordinate with another ligands and rational synthesis of oligo-nuclear complex are expected. In front of this paper, one kinds of linear multidentate ligand called H₂L, which has two β -diketone sites and one 2,6-diacetylpyridine site. There are two kinds of coordination sites in one ligand, therefor hetero oligo-nuclear complexes were reported.¹⁵⁻¹⁸ In addition, coordination ability of β -diketone was controllable with elimination-addition of proton. Selective structure control and interconversion were expected by control of pH.

Octa-nuclear complex (**M₈L₆**) and di-nuclear complex (**M₂(HL)₂**) were synthesized with divalent 3d metal ions ($M = \text{Mn, Co, and Zn}$) and H₂L in basic and acidic condition, respectively. Furthermore, bi nuclear complex was transformed to octa nuclear complex by adding the base.

Experiment

X-ray structure Determination.

All Single-crystal X-ray diffraction data were collected on a Bulker SMART APEX II ULTRA CCD-detector Diffractometer, a rotating-anode (Bruker Turbo X-ray source) with graphite-monochromated MoK α radiation ($\lambda = 0.71073 \text{ \AA}$) was used. A single crystal was mounted on a polymer film with liquid paraffin and the temperature kept constant under flowing N₂. All of the structures were solved by a standard direct method (XSELL V6.3.1 crystallographic software package of the Bruker AXS) and expanded using Fourier techniques. Fullmatrixleast-squares refinements were carried out with anisotropic thermal parameters for all non-hydrogen atoms. All of the hydrogen atoms were placed in the measured positions and refined using a riding model.

Elemental analysis and Spectroscopic Measurements.

Elemental analyses of carbon, hydrogen and nitrogen were carried out by the staff of technical support division graduate school of science, Kyushu University. X-ray fluorescence analysis was carried out on a Rigaku ZSX-100S. Infrared spectra were measured with a JASCO FT/IR-4200 using ATR method. UV-Vis absorption spectra were measured by JASCO V-630. ¹H-NMR spectra were obtained with JEOL 600MHz.

Materials

All chemicals were purchased of reagent grade and used without further purification.

Preparation of compounds

2,6-Pyridinedicarboxylic acid, dimethyl ester (Pmm)

Sulfuric acid (0.99 g) was added slowly into methanol suspension of pyridine-2,6-dicarboxylic acid (1.67 g, 10 mmol). The mixture was refluxed for 2.5 hour, then the resulting colorless solution was cooled in the freezer to obtain white crystals of 2,6-Pyridinedicarboxylic acid dimethyl ester. The crystals were filtered, washed with cold MeOH and recrystallized from MeOH. Yield: 1.51 g (80.6 %)

¹H-NMR (DMSO-d₆), δ : 8.57 ~ 8.68 ppm (3H; pyridine group), δ : 3.24 ppm (6H; CH₃ groups)

IR(v/cm⁻¹): 2964 b(v_{C-H}), 1614 s(v_{C=O}), 1559 s(v_{C=C})

2,6-di(acetoacetyl)pyridine (H₂L)

The preparation of H₂L was carried out by a modification of a previously published method¹⁹. Pmm (7.70 g, 46 mmol) and sodium methoxide (14.3 g, 260 mmol) were mixed in diethyl ether. Acetone was added in this suspension and the resulting mixture was refluxed for 3 hours. Yellow powder was filtered, and dissolved in hydroxy chloride solution (2M). The mixture was stirred for 6 hours at room temperature. Yellow solid of H₂L was filtered, washed with water and cold MeOH, and recrystallized from MeOH. Yield: 4.92 g (56.0 %).

¹H-NM (CDCl₃), δ: 7.97 ~ 8.19 ppm (3H; pyridine group), δ: 6.87 ppm (2H; CH₂ in β-diketone) δ: 2.29 ppm (6H; CH₃ group)

IR(v/cm⁻¹): 2964 b(v_{C-H}), 1614 s(v_{C=O}), 1559 s(v_{C=C})

[Mn₂(HL)₂(NO₃)₂(solv)₂] (Mn₂(HL)₂)

A methanolic solution of Mn(NO₃)₂·6H₂O (285 mg, 1.0 mmol in 5 ml) was added to a solution of H₂L (245 mg, 1.0 mmol) in methanol (5 ml). The resulting solution was left to stand without addition of base. Yellow crystals were obtained by slow evaporation of the solution at room temperature. Yield: 92 mg (30.8 %).

IR(v/cm⁻¹): 2964 b(v_{C-H}), 1620 s(v_{C=O}), 1509 s(v_{C=C}), 1458 s (v_{NO₃})

Found (%): C, 41.37; H, 3.88; N, 6.96

Calcd (%): C, 41.77; H, 3.89; N, 7.22

[Co₂(HL)₂(NO₃)₂(solv)₂] (Co₂(HL)₂)

Orange crystals of Co₂(HL)₂ were prepared by the same method as Mn₂(HL)₂ with using Co(NO₃)₂·6H₂O instead of Mn(NO₃)₂·6H₂O. Yield: 90 mg (29.5 %).

IR(v/cm⁻¹): 2964 b(v_{C-H}), 1629 s(v_{C=O}), 1518 s(v_{C=C}), 1455 s (v_{NO₃})

Found (%): C, 40.28; H, 3.72; N, 6.98

Calcd (%): C, 40.54; H, 3.66; N, 7.27

[Zn₂(HL)₂(NO₃)₂(solv)₂] (Zn₂(HL)₂)

Yellow crystals of Zn₂(HL)₂ were prepared by the same method as Mn₂(HL)₂ with using Zn(NO₃)₂·6H₂O instead of Mn(NO₃)₂·6H₂O. Yield: 102 mg (34.2 %).

IR(v/cm⁻¹): 2964 b(v_{C-H}), 1619 s(v_{C=O}), 1509 s(v_{C=C}), 1454 s (v_{NO₃})

Found (%): C, 40.19; H, 3.21; N, 7.20

Calcd (%): C, 39.87; H, 3.60; N, 7.15

[Mn₈L₆(μ₃-O)₂] (Mn₈L₆)

A methanolic solution of Mn(NO₃)₂·6H₂O (582 mg, 2.0 mmol in 10 ml) was added to the solution of H₂L (382 mg, 1.5 mmol) in methanol (10 ml). Triethylamine was added to the resulting solution to adjust the pH to 8. Yellow crystals were obtained by slow evaporation of the solution at room temperature. Yield: 261 mg (53.0 %).

IR(v/cm⁻¹): 1615 s(ν_{C=O}), 1581 s(ν_{C=C})

Found (%): C, 48.58; H, 3.21; N, 4.56

Calcd (%): C, 48.22; H, 3.42; N, 4.33

[Co₈L₆(μ₃-O)₂] (Co₈L₆)

Red crystals of Co₈L₆ were prepared by the same method as Mn₈L₆ with using Co(NO₃)₂·6H₂O instead of Mn(NO₃)₂·6H₂O. Yield: 301 mg (61.3 %). Yield: 301 mg (61.3 %).

IR(v/cm⁻¹): 1615 s(ν_{C=O}), 1581 s(ν_{C=C})

Found (%): C, 47.60; H, 3.59; N, 4.51

Calcd (%): C, 47.44; H, 3.37; N, 4.26

[Zn₈L₆(μ₃-O)₂] (Zn₈L₆)

Yellow crystals of Zn₈L₆ were prepared by the same method as Mn₈L₆ with using Zn(NO₃)₂·6H₂O instead of Mn(NO₃)₂·6H₂O. Yield: 289 mg (57.5 %).

IR(v/cm⁻¹): 1615 s(ν_{C=O}), 1581 s(ν_{C=C})

Found (%): C, 45.11; H, 3.66; N, 4.37

Calcd (%): C, 46.23; H, 3.28; N, 4.15

Results and discussion

X-Ray Structural Characterization

X-ray crystallographic analysis reveals that Mn₂(HL)₂, Co₂(HL)₂, and Zn₂(HL)₂ are isomorphic, respectively. Crystal parameters for complexes are summarized in Table 1. The selected bond lengths and angles for complexes are described in Table 2-4. Mn₂(HL)₂ crystallizes in monoclinic system with space group *P*2₁/*n*. The asymmetric unit consists of one M²⁺ ion and one HL⁻. The HL⁻ coordinated to two different M²⁺ ions

with one 1,3-diketone and one 2,6-diacetylpyridine sites, and one 1,3-diketone site was protonated and coordination-free, forming the enolate-bridged dinuclear structure. M^{2+} ions are in seven-coordinated pentagonal-bipyramidal geometry with one monodentate nitrate and one water molecule at the axial sites. Selected bond distances and angles are listed in Tables S2–4. In the equatorial pentagonal plane, the bond distances of M1-O1, M1-O2 and M1-O2# (#: symmetry operation 1-x, 1-y, 1-z) are in the range of 2.1558(16)–2.2178(16) Å for Mn, 2.062(2)–2.146(2) Å for Co, and 2.151(4)–2.213(3) Å for Zn. The other equatorial bonds, M1-N1 and M1-O3#, are elongated to 2.311(2) and 2.349(2) Å for Mn, 2.206(2) and 2.385(2) Å for Co, and 2.307(4) and 2.346(4) Å for Zn. The protonated enol oxygen O3 formed relatively weak bonds with metal ions. Two metal ions are linked by two enolate-bridges with the bridging angle of 105.52(6)° for Mn, 108.05(7)° for Co, and 105.7(1)° for Zn.

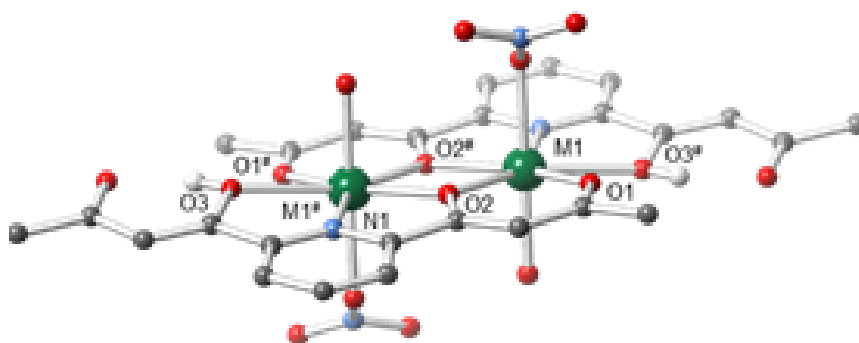


Fig. 1 Structure of $M_2(HL)_2$

Octa-nuclear complexes Mn_8L_6 , Co_8L_6 , and Zn_8L_6 are also isomorphous (Figure 2, Tables 5–8). The asymmetric unit consists of four M^{2+} and three L^{2-} , including a terminal mononuclear unit $[M(L)_3]^{4-}$ with the 1,3-diketone site and an oxo-bridged trinuclear unit $[M_3(\mu_3-O)]^{4+}$ with the 2,6-diacetylpyridine site, which forms a tetranuclear unit (Figure 3). Two tetrad units are interdigitated through the 1,3-diketone sites (blue color in Figure 3) and form an octa-nuclear cluster structure. Selected bond distances and angles are listed in Tables 6–8. The mononuclear unit fixed three L^{2-} like a tripod and formed a space to accommodate the trinuclear unit. In the trinuclear unit, all metal ions are in a distorted octahedral geometry with short M- μ_3 -O bonds (average bond length: 2.045 Å for Mn, 1.977 Å for Co, and 1.957 Å for Zn) and bonds with L^{2-} (bond length range: 2.140(7)–2.374(4) Å for Mn, 2.018(8)–2.352(8) Å for Co, and 2.068(3)–2.370(4) Å for Zn).

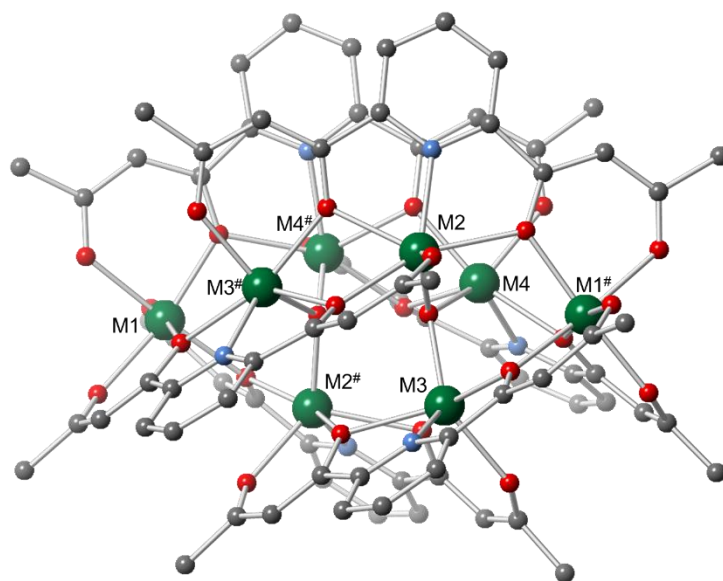


Fig. 2 Structure of **M₈L₆**

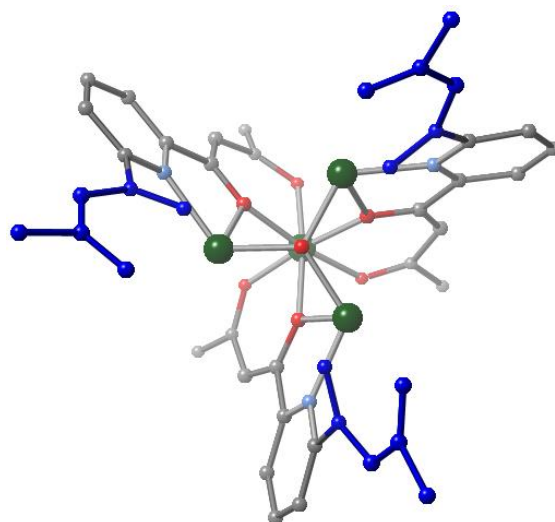


Fig. 3 The asymmetric unit of **M₈L₆**

Table 1 Crystal parameter of **M₂(HL)₂**

Name	Mn₂(HL)₂	Co₂(HL)₂	Zn₂(HL)₂
Empirical formula	C ₂₆ H ₂₈ O ₁₆ Mn ₂ N ₄	C ₂₆ H ₂₂ Co ₂ N ₄ O ₁₆	C ₂₆ H ₂₈ N ₄ O ₁₆ Zn ₂
Crystal system	monoclinic	monoclinic	monoclinic
Space group	P2 ₁ /n	P2 ₁ /n	P2 ₁ /n
<i>a</i> /Å	9.925(3)	9.986(3)	9.921(4)
<i>b</i> /Å	13.733(3)	13.577(4)	13.726(5)
<i>c</i> /Å	10.768(3)	10.653(3)	10.757(4)
<i>α</i> °	90	90	90
<i>β</i> °	93.675(3)	94.118(4)	93.716(4)
<i>γ</i> °	90	90	90
<i>Volume</i> /Å ³	1464.7(6)	1440.6(7)	1461.7(9)
<i>Z</i>	2	2	2
<i>GOF</i>	0.828	1.035	1.041
<i>R</i> <i>I</i>	0.0355	0.0358	0.0668
<i>wR</i>	0.1183	0.0914	0.2166

Table 2 Selected bond distances and angles for **Mn₂(HL)₂**

Bond Distances(Å)			
<i>equatorial</i>		<i>axial</i>	
Mn1-O1	2.1558(16)	Mn1-O5	2.2197(17)
Mn1-O2	2.2051(15)	Mn1-O8	2.1821(16)
Mn1-O2 [#]	2.2178(16)		
Mn1-O3 [#]	2.3491(16)		
Mn1-N1 [#]	2.3107(18)		
Bond Angles (°)			
O1-Mn1-O2	80.04(6)	O2 [#] -Mn1-O3 [#]	135.22(6)
O1-Mn1-O2 [#]	154.51(6)	O2 [#] -Mn1-O5	89.26(6)
O1-Mn1-O3 [#]	70.23(6)	O2 [#] -Mn1-O8	87.95(6)
O1-Mn1-O5	89.92(7)	O2 [#] -Mn1-N1 [#]	69.88(6)
O1-Mn1-O8	93.16(6)	O3 [#] -Mn1-O5	94.38(6)
O1-Mn1-N1 [#]	135.28(6)	O3 [#] -Mn1-O8	86.68(6)
O2-Mn1-O2 [#]	74.48(6)	O3 [#] -Mn1-N1 [#]	66.22(6)
O2-Mn1-O3 [#]	149.85(6)	O5-Mn1-O8	176.92(6)
O2-Mn1-O5	90.41(6)	O5-Mn1-N1 [#]	83.78(6)

[#]: symmetry operation 1-x, 1-y, 1-z

Table 3 Selected bond distances and angles for **Co₂(HL)₂**

Bond Distances(Å)*equatorial*

Co1-O1	2.0621(17)
Co1-O2	2.1458(17)
Co1-O2 [#]	2.1243(17)
Co1-O3 [#]	2.3854(18)
Co1-N1 [#]	2.207(2)

axial

Co1-O5	2.1671(18)
Co1-O8	2.0996(17)

Bond Angles (°)

O1-Co1-O2	81.74(7)	O2 [#] -Co1-O3 [#]	137.98(6)
O1-Co1-O2 [#]	153.63(7)	O2 [#] -Co1-O5	90.69
O1-Co1-O3 [#]	68.25(7)	O2 [#] -Co1-O8	87.39(7)
O1-Co1-O5	88.56(7)	O2 [#] -Co1-N1 [#]	73.28(7)
O1-Co1-O8	94.69(7)	O3 [#] -Co1-O5	95.92(7)
O1-Co1-N1 [#]	132.59(8)	O3 [#] -Co1-O8	83.26(7)
O2-Co1-O2 [#]	71.95(7)	O3 [#] -Co1-N1 [#]	66.61(7)
O2-Co1-O3 [#]	148.64(6)	O5-Co1-O8	176.07(7)
O2-Co1-O5	91.97	O5-Co1-N1 [#]	82.47(7)

[#]: symmetry operation 1-x, 1-y, 1-z

Table 4 Selected bond distances and angles of **Zn₂(HL)₂**

Bond Distances(Å)			
<i>equatorial</i>		<i>axial</i>	
Zn1-O1	2.151(4)	Zn1-O5	2.217(4)
Zn1-O2	2.203(4)	Zn1-O8	2.183(4)
Zn1-O2 [#]	2.213(4)		
Zn1-O3 [#]	2.346(4)		
Zn1-N1 [#]	2.307(4)		
Bond Angles (°)			
O1-Zn1-O2	80.13(14)	O2 [#] -Zn1-O3 [#]	135.30(13)
O1-Zn1-O2 [#]	154.45(14)	O2 [#] -Zn1-O5	89.34(14)
O1-Zn1-O3 [#]	70.19(14)	O2 [#] -Zn1-O8	87.75(14)
O1-Zn1-O5	90.10(15)	O2 [#] -Zn1-N1 [#]	70.02(13)
O1-Zn1-O8	93.06(15)	O3 [#] -Zn1-O5	94.47(15)
O1-Zn1-N1 [#]	135.24(14)	O3 [#] -Zn1-O8	86.75(15)
O2-Zn1-O2 [#]	74.33(15)	O3 [#] -Zn1-N1 [#]	66.20(13)
O2-Zn1-O3 [#]	149.90(13)	O5-Zn1-O8	176.84(14)
O2-Zn1-O5	90.38(14)	O5-Zn1-N1 [#]	83.77(14)

[#]: symmetry operation 1-x, 1-y, 1-z

Table 5 Crystal parameter of **M₈L₆**

Name	Mn₈L₆	Co₈L₆	Zn₈L₆
Empirical formula	C ₇₈ H ₆₆ Mn ₈ N ₆ O ₂₆	C ₇₈ H ₆₆ Co ₈ N ₆ O ₂₆	C ₇₈ H ₆₆ Zn ₈ N ₆ O ₂₆
Crystal system	monoclinic	monoclinic	monoclinic
Space group	<i>C2/c</i>	<i>C2/c</i>	<i>C2/c</i>
<i>a</i> /Å	34.450(16)	33.98(3)	31.810(4)
<i>b</i> /Å	12.581(6)	12.359(11)	12.4337(17)
<i>c</i> /Å	25.153(11)	25.07(2)	25.690(4)
<i>α</i> /°	90	90	90
<i>β</i> /°	127.904(5)	127.564(13)	120.3410(10)
<i>γ</i> /°	90	90	90
<i>Volume</i> /Å ³	8602(7)	8345(12)	8769(2)
<i>Z</i>	4	4	4
<i>GOF</i>	1.044	0.989	1.117
<i>RI</i>	0.648	0.732	0.0542
<i>wR</i>	0.1716	0.1622	0.1353

Table 6 Selected bond distances and bridging angles for **Mn₈L₆**

Bond Distances(Å)			
Mn1-O1	2.181(5)	Mn3-O2 [#]	2.273(4)
Mn1-O2	2.155(4)	Mn3-O3 [#]	2.265(4)
Mn1-O5	2.145(5)	Mn3-O7	2.167(4)
Mn1-O6	2.203(4)	Mn3-O8	2.168(5)
Mn1-O9	2.120(5)	Mn3-O13	2.051(4)
Mn1-O10	2.180(5)	Mn3-N1 [#]	2.204(5)
Mn2-O3	2.153(5)	Mn4-O10 [#]	2.164(5)
Mn2-O4	2.139(4)	Mn4-O11	2.212(5)
Mn2-O6 [#]	2.293(4)	Mn4-O11 [#]	2.035(4)
Mn2-O7 [#]	2.374(4)	Mn4-O12	2.309(4)
Mn2-O13	2.049(4)	Mn4-O13	2.304(5)
Mn2-N2 [#]	2.215(5)	Mn4-N3 [#]	2.216(6)
Bond Angles (°)			
Mn1-O6-Mn2 [#]	114.1(2)	Mn2-O13-Mn3	115.1(2)
Mn1-O2-Mn3 [#]	110.9(2)	Mn2-O13-Mn4	116.9(2)
Mn1-O10-Mn4 [#]	113.7(2)	Mn3-O13-Mn4	115.1(2)
Mn2-O3-Mn3	105.1(2)	Mn4-O11-Mn4 [#]	104.5(2)
Mn2 [#] -O7-Mn3	101.1(2)		

[#]: symmetry operation 1-x, y, 3/2-z

Table 7 Selected bond distance and bridging angles for **Co₈L₆**

Bond Distances(Å)			
Co1-O1	2.082(8)	Co3-O2 [#]	2.150(8)
Co1-O2	2.059(9)	Co3-O3 [#]	2.298(10)
Co1-O5	2.047(8)	Co3-O7	2.019(8)
Co1-O6	2.081(8)	Co3-O8	2.110(8)
Co1-O9	2.035(10)	Co3-O13	2.003(8)
Co1-O10	2.062(8)	Co3-N1 [#]	2.077(10)
Co2-O3	2.019(9)	Co4-O10 [#]	2.199(9)
Co2-O4	2.026(9)	Co4-O11	2.075(11)
Co2-O6 [#]	2.169(7)	Co4-O11 [#]	2.353(10)
Co2-O7 [#]	3.172	Co4-O12	2.108(9)
Co2-O13	1.983(8)	Co4-O13	1.950(7)
Co2-N2 [#]	2.088(9)	Co4-N3 [#]	2.107(11)
Bond Angles (°)			
Co1-O6-Co2 [#]	117.9(4)	Co2-O13-Co3	113.0(4)
Co1-O2-Co3 [#]	114.7(4)	Co2-O13-Co4	115.3(4)
Co1-O10-Co4 [#]	117.7(4)	Co3-O13-Co4	114.6(4)
Co2-O3-Co3	110.9(4)	Co4-O11-Co4 [#]	108.2(5)
Co2 [#] -O7-Co3	101.9(3)		

[#]: symmetry operation 1-x, y, 3/2-z

Table 8 Selected bond distances and bridging angles for **Zn₈L₆**

Bond Distances(Å)			
Zn1-O1	2.089(3)	Zn3-O2 [#]	2.251(3)
Zn1-O2	2.064(3)	Zn3-O3 [#]	2.274(4)
Zn1-O5	2.074(3)	Zn3-O7	2.118(4)
Zn1-O6	2.079(3)	Zn3-O8	2.068(3)
Zn1-O9	2.079(3)	Zn3-O13	1.959(3)
Zn1-O10	2.085(3)	Zn3-N1 [#]	2.109(4)
Zn2-O3	2.107(4)	Zn4-O10 [#]	2.243(3)
Zn2-O4	2.071(3)	Zn4-O11	2.140(4)
Zn2-O6 [#]	2.242(3)	Zn4-O11 [#]	2.278(5)
Zn2-O7 [#]	2.369(4)	Zn4-O12	2.076(4)
Zn2-O13	1.963(3)	Zn4-O13	1.949(3)
Zn2-N2 [#]	2.095(4)	Zn4-N3 [#]	2.103(4)
Bond Angles (°)			
Zn1-O6-Zn2 [#]	118.6(1)	Zn2-O13-Zn3	114.4(2)
Zn1-O2-Zn3 [#]	117.3(2)	Zn2-O13-Zn4	115.3(2)
Zn1-O10-Zn4 [#]	117.3(2)	Zn3-O13-Zn4	116.0(2)
Zn2-O3-Zn3	107.2(2)	Zn4-O11-Zn4 [#]	106.9(2)
Zn2 [#] -O7-Zn3	103.5(2)		

[#]: symmetry operation 1-x, y, 3/2-z

Absorption properties of Co complexes

Fig. 4 shows UV-Vis spectra of **Co₂(HL)₂** and **Co₈L₆**. To make conditions equal, vertical scale is absorptivity of each Co(II) ion. The spectrum of **Co₂(HL)₂** had the peak around $\lambda=330$ nm which was π - π^* transition from HL- ligands. On the other hand, the absorption peak of **Co₈L₆** was around $\lambda=350$ nm. This red shift was caused by deprotonation of the L^{2-} ligands. Fig. 5 shows UV-vis spectra expanded vertical scale of **Co₂(HL)₂** and **Co₈L₆**. Both spectra have broad band which assigned as d-d transitions. The band of **Co₂(HL)₂** located around $\lambda=500$ nm. The band of **Co₈L₆** located around $\lambda=600$ nm, longer wavelength than that of **Co₂(HL)₂**.

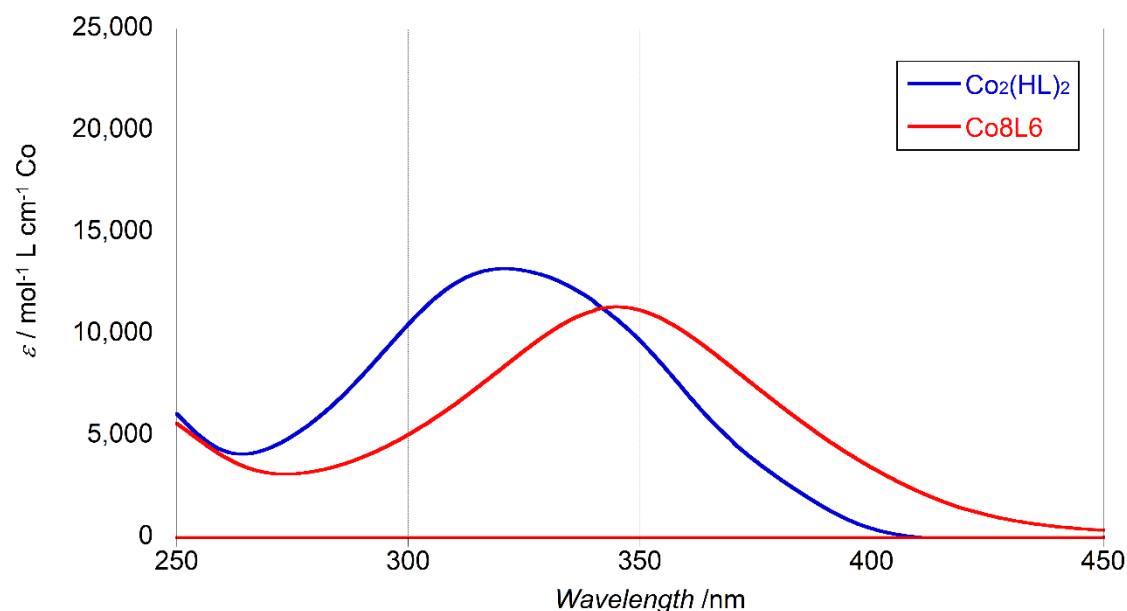


Fig. 4 UV-vis absorption spectra of Co complexes. Absorptivity was normalized with Co(II) ion.

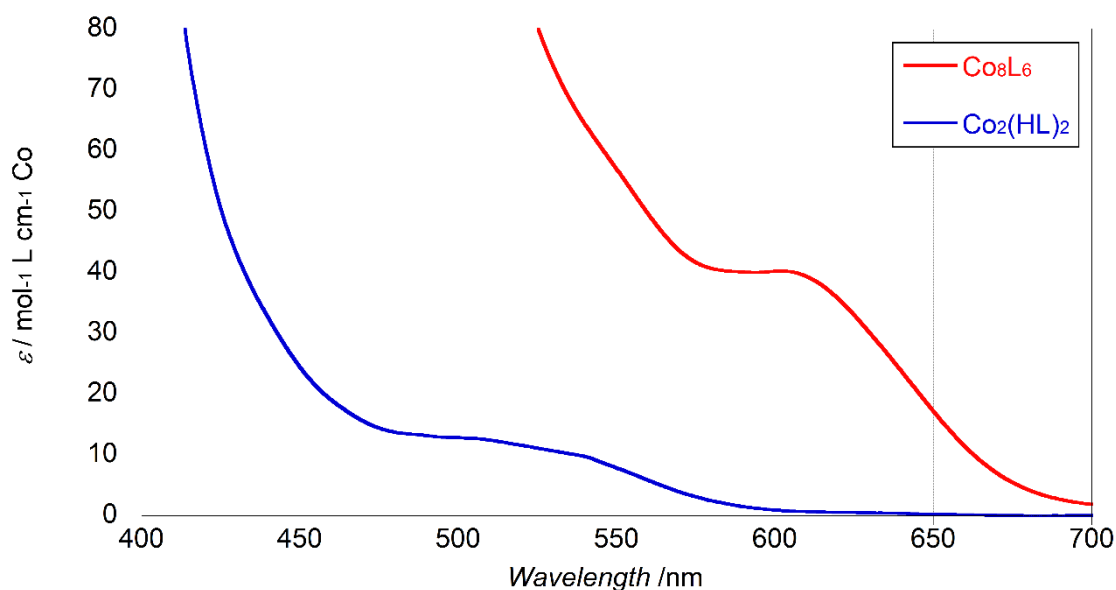
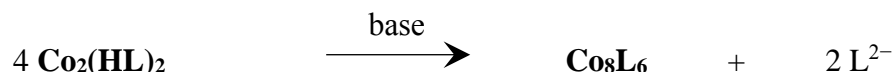


Fig. 5 UV-vis absorption spectra of Co complexes. Absorptivity was normalized with Co(II) ion.

Structural conversion from di-nuclear to octa nuclear complex.

Because the dinuclear complexes $\mathbf{M}_2(\mathbf{HL})_2$ have two protonated and coordination-free 1,3-diketone sites, structure change is expected by deprotonation. To confirm the structure change, UV-vis spectra of methanolic solution of $\mathbf{Co}_2(\mathbf{HL})_2$ was traced with changing pH

Fig. 6 and 7 show the UV-vis spectra of $\mathbf{Co}_2(\mathbf{HL})_2$ with 0-3 equivalents of triethylamine added as a base. Methanolic solution of $\mathbf{Co}_2(\mathbf{HL})_2$ exhibits a peak of $\pi-\pi^*$ transition of \mathbf{HL}^- (λ_L) near 320 nm and a broad peak of d-d transition of Co(II) (λ_{Co}) near 520 nm. After the addition of 0.1 eq. base, λ_L shifted to near 345 nm with increased absorption coefficient ε_L . With the increased amount of base, ε_L increased without a change of λ_L ; in contrast, λ_{Co} gradually shifted to 620 nm with increasing ε_{Co} . The resulting λ_L and λ_{Co} agreed with those of free \mathbf{L}^{2-} and $\mathbf{Co}_8\mathbf{L}_6$, but value of ε_L after adding base was much higher than that of $\mathbf{Co}_8\mathbf{L}_6$. These results suggested the following reaction occurred by the addition of base:



In this reaction, four $\mathbf{Co}_2(\mathbf{HL})_2$ are transformed to one $\mathbf{Co}_8\mathbf{L}_6$ with the release of two

deprotonated ligands, L^{2-} . The release of L^{2-} was supported by the increase of ϵ_L near 345 nm. According to the reaction scheme, UV-vis absorption spectra of the resulting solutions were well regenerated as a summation of spectra of Co_8L_6 and L^{2-} (Fig. 8)

To the contrary, Co_8L_6 was not converted by the addition of L^{2-} and nitric acid. Although the spectra showed a small blue-shift of λ_{Co} and decrease in ϵ_L , it did not recover the spectrum of $Co_2(HL)_2$ (Fig. 9). The irreversible conversion is related to the structural stability of Co_8L_6 interdigitated by six L^{2-} . The structure is clearly more stable than that of $Co_2(HL)_2$ including two pentahedral bipyramidal Co(II) with two protonated HL^- . Mn_8L_6 and Zn_8L_6 were also obtained from the basic methanolic solution of $Mn_2(HL)_2$ and $Zn_2(HL)_2$, respectively.

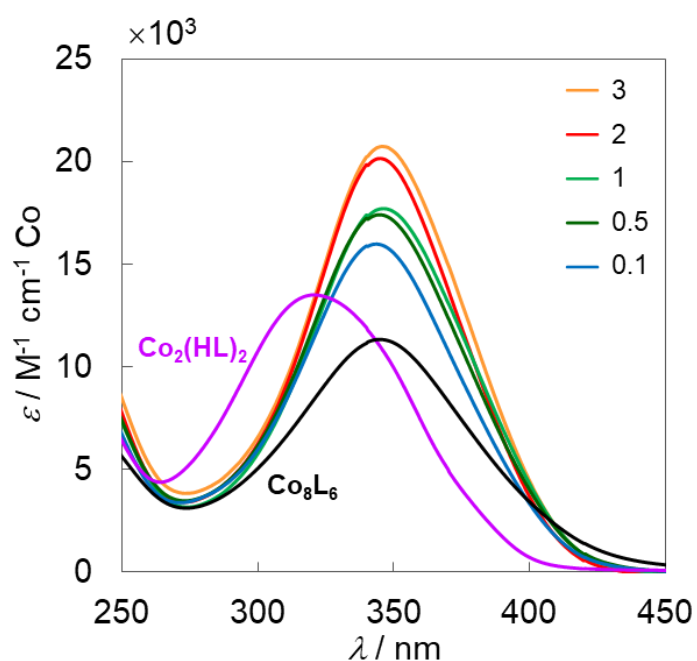


Fig. 6 UV-vis spectra of $Co_2(HL)_2$ with 0.1-3 eq. of NEt_3 added and Co_8L_6 .

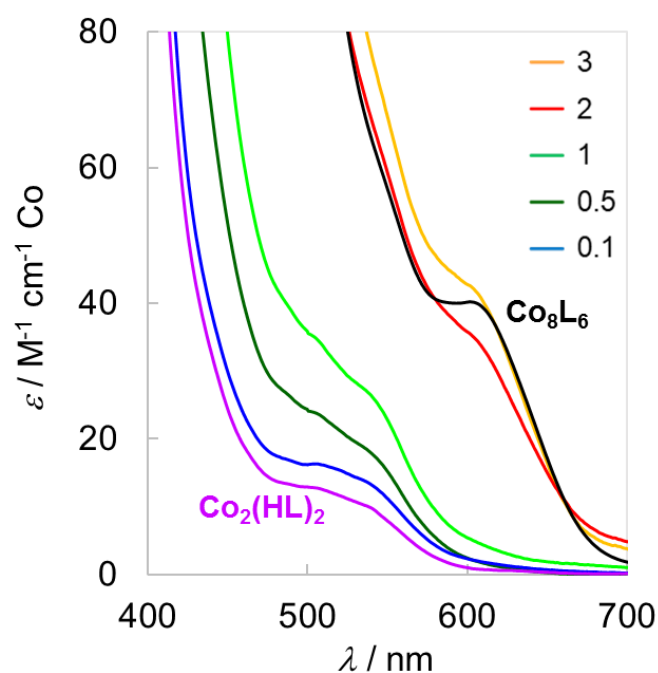


Fig. 7 UV-vis spectra of $\text{Co}_2(\text{HL})_2$ with 0.1-3 eq. of NEt_3 added and Co_8L_6 .

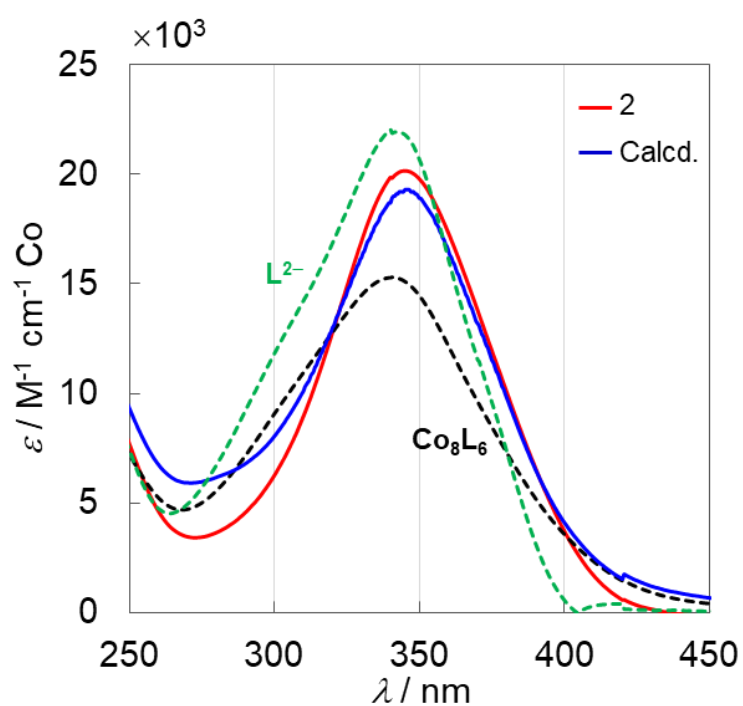


Fig. 8 Calculated UV-vis spectrum of Co_8L_6 and L^{2-} (blue) and UV-vis spectra of $\text{Co}_2(\text{HL})_2$ and H_2L with 2 eq. of NEt_3 (red and dashed green lines, respectively) and Co_8L_6 (dashed black).

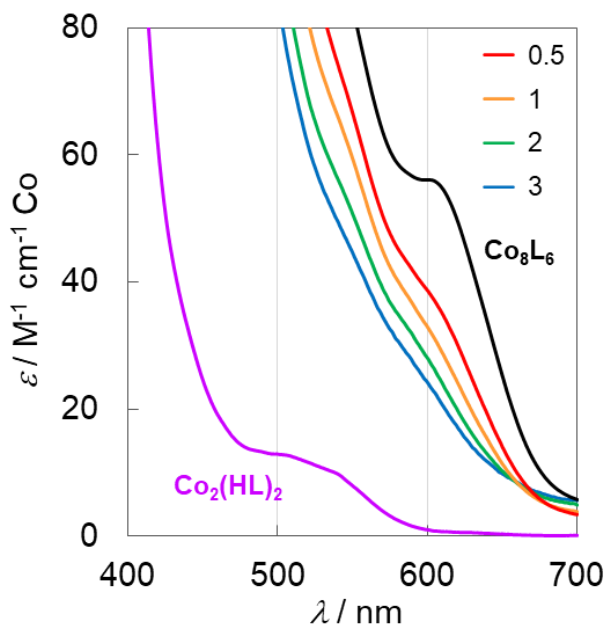


Fig. 9 UV-vis spectra of **Co₈L₆** with 2 eq. of L^{2-} and 0.1-3 eq. of nitric acid added.

Magnetic properties

$\chi_M T$ vs. T plots of all compounds are shown in Figure 3. At room temperature, all compounds Co(II) ($S = 3/2$) and Mn(II) ($S = 5/2$) complexes showed antiferromagnetic behavior. In the case of **Co₂(HL)₂** and **Co₈L₆**, the magnetic behavior included the contribution of the spin-orbit coupling of single Co(II) ions. Detailed magnetic analysis was difficult for these compounds except for **Mn₂(HL)₂**. Magnetic simulation of **Mn₂(HL)₂** was carried out with a simple isotropic $S = 5/2 + 5/2$ model with spin Hamiltonian $H = -2JS_1 \cdot S_2$, and yielded $J = -1.03 \text{ cm}^{-1}$ and $g = 2.00$. Weak antiferromagnetic interaction operated between the two Mn(II) ions through two enolate-bridges. No signal was observed at 2 K in AC magnetization measurements for all compounds.

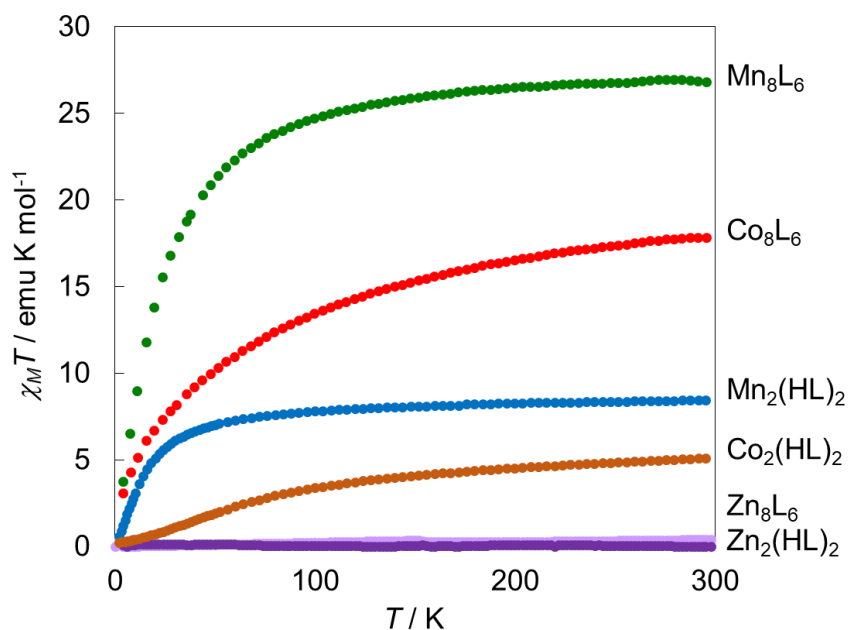


Fig. 10 $\chi_M T$ vs. T plots of **M₂(HL)₂** and **M₈L₆**.

Conclusion

In summary, di-nuclear complexes **M₂(HL)** and octa-nuclear complexes **M₈L₆** were selectively prepared by adjusting pH with a linear multidentate diprotic ligand H₂L. **M₂(HL)** having protonated 1,3-diketone sites were irreversibly transformed to **M₈L₆** by the addition of base. The unique structural conversion yields significant information about the formation process of the cluster structure in solution. The appropriate combination between metal ions and ligands and control of the assembled structure are useful for drawing out the performance of the catalytic reaction, magnetic properties, optical properties, and other aspects.

Reference

1. M. Okamura, M. Kondo, R. Kuga, Y. Kurashige, T. Yanai, S. Hayami, V. K. K. Praneeth, M. Yoshida, K. Yoneda, S. Kawata and S. Masaoka, *Nature*, 2016, **530**, 465.
2. H. Ozawa, M. A. Haga and K. Sakai, *J. Am. Chem. Soc.*, 2006, **128**, 4926-4927.
3. R. Sessoli, D. Gatteschi, A. Caneschi and M. A. Novak, *Nature*, 1993, **365**, 141.
4. L. Thomas, F. Lioni, R. Ballou, D. Gatteschi, R. Sessoli and B. Barbara, *Nature*, 1996, **383**, 145-147.
5. R. Sessoli and A. K. Powell, *Coord. Chem. Rev.*, 2009, **253**, 2328-2341.
6. D. Gatteschi and R. Sessoli, *Angew. Chem. Int. Ed.*, 2003, **42**, 268-297.
7. M. G. Han, Y. Tian, Z. Yuan, L. Zhu and B. W. Ma, *Angew. Chem. Int. Ed.*, 2014, **53**, 10908-10912.
8. T. Lis, *Acta Crystallographica Section B-Structural Science*, 1980, **36**, 2042-2046.
9. A. Yoshino, H. Matsudaira, E. Asato, M. Koikawa, T. Shiga, M. Ohba and H. Okawa, *Chem. Commun.*, 2002, 1258-1259.
10. H. Tamaki, Z. J. Zhong, N. Matsumoto, S. Kida, M. Koikawa, N. Achiwa, Y. Hashimoto and H. Okawa, *J. Am. Chem. Soc.*, 1992, **114**, 6974-6979.
11. M. U. Anwar, L. K. Thompson, L. N. Dawe, F. Habib and M. Murugesu, *Chem. Commun.*, 2012, **48**, 4576-4578.
12. H. Oshio, M. Nihei, S. Koizumi, T. Shiga, H. Nojiri, M. Nakano, N. Shirakawa and M. Akatsu, *J. Am. Chem. Soc.*, 2005, **127**, 4568-4569.
13. H. Oshio, N. Hoshino and T. Ito, *J. Am. Chem. Soc.*, 2000, **122**, 12602-12603.
14. K. Yoneda, K. Adachi, K. Nishio, M. Yamasaki, A. Fuyuhiko, M. Katada, S. Kaizaki and S. Kawata, *Angew. Chem. Int. Ed.*, 2006, **45**, 5459-5461.
15. T. Shiga, M. Ohba and H. Ōkawa, *Inorg. Chem.*, 2004, **43**, 4435-4446.
16. T. Shiga, M. Ohba and H. Ōkawa, *Inorg. Chem. Commun.*, 2003, **6**, 15-18.
17. T. Shiga, M. Ohba and H. Okawa, *Inorg. Chem.*, 2004, **43**, 4435-4446.
18. T. Shiga, N. Ito, A. Hidaka, H. Ohkawa, S. Kitagawa and M. Ohba, *Inorg. Chem.*, 2007, **46**, 3492-3501.
19. D. E. Fenton, J. R. Tate, U. Casellato, S. Tamburini, P. A. Vigato and M. Vidali, *Inorg. Chim. Acta.*, 1984, **83**, 23-31.

Chapter 2

Synthesis and Luminescence Properties of Trinuclear Lanthanide Complexes with Linear Multidentate Ligands

Abstract

Novel trinuclear lanthanide complexes, $[\text{Ln}_3\text{L}_2(\text{NO}_3)_5(\text{MeOH})_4] \cdot n\text{solv}$ (**Ln₃L**: Ln = La, Ce, Pr, Eu) and $[\text{Eu}_3\text{L}^{\text{F}}_2(\text{NO}_3)_5(\text{H}_2\text{O})_3(\text{MeOH})] \cdot 3\text{MeOH}$ (**Eu₃L^F**) were obtained using triple-arch-type ligands, 2,6-di(acetoacetyl)pyridine (H_2L) or 2,6-di(1,1,1-trifluoro-acetoacetyl)pyridine ($\text{H}_2\text{L}^{\text{F}}$), having two β -diketone and one central 2,6-diacetylpyridine sites. They formed analogous structures, in which three Ln(III) ions were located between two ligands with coordinated nitrate anions and solvents. The central Ln(III) ion had different coordination environment from that on both sides. **Eu₃L** showed red luminescence around 618 nm with quantum yield of 0.43% in solid state. Thermal vibration of C-H bonds of methyl groups in L^{2-} was a one of the main factors for the low light emission quantum yield. In the case of **Eu₃L^F**, the methyl groups were substituted to the trifluoromethyl groups to compress the thermal vibration, which enhanced the quantum yield to 8.07%. We successfully established a rational synthesis method of trinuclear lanthanide complexes by using linear multidentate ligands, and improved their luminescent properties by suppressing vibrational relaxation.

Introduction

Photo luminescence is one of the luminous properties which occurs when a photo-irradiated matter returns from excited state to the ground state. Photo luminescence components are expected primitive mechanism, so it is expected to be applied as sensor^{1, 2} and display.³ Especially, lanthanide compounds have been applied for a lot of photo luminescent materials. Some lanthanide ions such as europium and terbium, exhibit remarkable photo luminescent properties. Trivalent lanthanide ions have some electrons in the 4f orbitals and eight electrons in 5s² and 5p⁶ orbitals. The 4f orbitals are shielded from surroundings by the 5s² and 5p⁶ orbitals, so they are hardly affected by ligand fields. This is called “shielding effect”, and the effect causes remarkable lanthanide-ion-specific luminescent properties (luminescent wavelength, Stokes shift, and color purity), e.g. Eu(III) and Sm(III) show red emission,^{4, 5} Tb(III) shows green emission,⁶ Nd(III), Er(III) and Yb(III) show infrared emission.⁷ Because of these property, lanthanide ions are expected to be applied as not only luminescence materials⁸ but also solid laser⁹ and luminescence probes.^{10, 11} However, the luminescence efficiency of lanthanide ions is low, because of very low absorption coefficient ($\varepsilon = 1 \sim 10 \text{ cm}^{-1} \text{ mol}^{-1} \text{ dm}^3$). On the other hand, lanthanide complexes shows strong luminescence, because of energy transfer from ligands to metal center with high absorption coefficient ($\varepsilon = 10^3 \sim 10^4 \text{ cm}^{-1} \text{ mol}^{-1} \text{ dm}^3$) of π - π^* transition. The energy transfer through excited organic ligands is a key process to improve the luminescence efficiency of lanthanide complexes.¹² This is called “antenna effect”, and this is a reason that lanthanide complexes are promising compounds as new luminescence materials.

Luminescence properties of lanthanide complexes have been extensively studied using mono-nuclear complexes so far,^{13, 14} whereas poly- and oligo-nuclear lanthanide complexes are still rare. In particular, hetero-nuclear lanthanide complexes are expected to exhibit multi-color emission^{15, 16} based on different lanthanide ions and highly-efficient luminescence due to metal to metal energy transfer.¹⁷⁻¹⁹ However, rational design of oligo-nuclear lanthanide complexes is still challenging, because coordination number of lanthanide ions is too flexible. In this chapter, we aimed to establish a rational synthesis method of oligo-nuclear lanthanide complexes and to investigate their luminescence properties systematically.

To prepare tri-nuclear lanthanide complexes rationally, we designed multidentate ligands providing three linearly-arranged metal binding sites (Fig. 1). These ligands provide two kinds of metal binding sites, one central 2,6-diacetylpyridine site and two β -diketone sites at each sides, which are expected to accommodate three metal ions in

each metal binding sites. This structure is available for arranging metal ions in different coordination environment, e.g. 3d-4f-3d hetero trinuclear complexes arranging lanthanide ions at the 2,6-diacetylpyridine site and M(II) ions (M = Co, Ni, Cu, Zn) at β -diketone sites were selectively prepared using different ionic radius.²⁰⁻²³ In this chapter, we report the synthesis, identification and luminescence properties of trinuclear lanthanide complexes $[\text{Ln}_3\text{L}_2(\text{NO}_3)_5(\text{MeOH})_4] \cdot n\text{MeOH}$ (**Ln₃L**: Ln = La, Ce, Pr, Eu), $[\text{Eu}_3\text{L}^{\text{F}}_2(\text{NO}_3)_5(\text{H}_2\text{O})_2(\text{MeOH})_2] \cdot 3\text{MeOH}$ (**Eu₃L^F**).

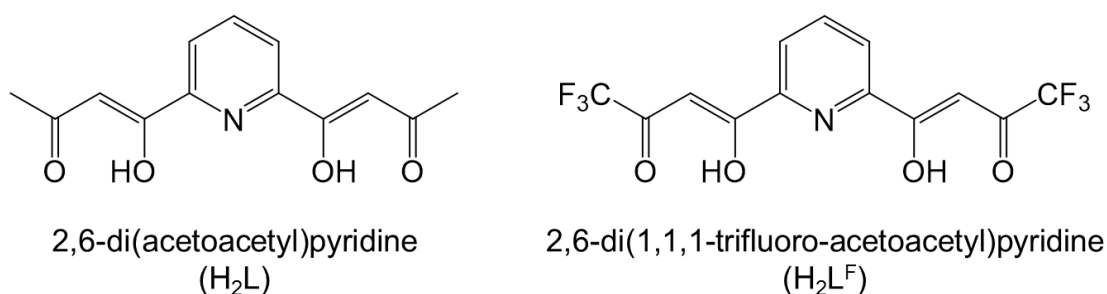


Fig. 1. Linear multidentate ligands

Experiments

Physical Measurements

Elemental analyses of carbon, hydrogen and nitrogen were carried out by the staff of technical support division graduate school of science, Kyushu University. All Single-crystal X-ray diffraction data were collected on a Bulker SMART APEX II ULTRA CCD-detector Diffractometer, a rotating-anode (Bruker Turbo X-ray source) with graphite-monochromated MoK α radiation ($\lambda = 0.71073 \text{ \AA}$) was used. A single crystal was mounted on a polymer film with liquid paraffin and the temperature kept constant under flowing N₂. All of the structures were solved by a standard direct method (XSELL V6.3.1 crystallographic software package of the Bruker AXS) and expanded using Fourier techniques. Fullmatrixleast-squares refinements were carried out with anisotropic thermal parameters for all non-hydrogen atoms. All of the hydrogen atoms were placed in the measured positions and refined using a riding model. X-ray fluorescence analysis was carried out on a Rigaku ZSX-100S. Infrared spectra were measured with a JASCO FT/IR-4200 using ATR method. UV-Vis absorption and emission spectra were measured by JASCO V-630 and FP-8200. HNMR spectra were obtained with JEOL 600MHz.

Photoluminescence quantum yield measurements were carried out on C9920-02; Absolute quantum yield measurement system made by Hamamatsu Photonics K.K. at room temperature. PL quantum yield was calculated with the following equation:

$$\Phi = \frac{\int I_{em} d\lambda}{\int (I_{ex}^{before} - I_{ex}^{after}) d\lambda}$$

I_{em} is the amount of photon from emission, I_{ex}^{before} is amount of photon from excitation light that nothing absorbed, and I_{ex}^{after} is amount of photon from excitation light that something absorbed.

Emission lifetime measurements were carried out on C11200 / Picosecond fluorescence lifetime measurement system at room temperature. Theoretical value of emission lifetime was calculated with the following equation.

$$\sum_i A_i \exp(-\frac{t}{\tau_i})$$

A_i is a coefficient, t is current time, τ_i is emission lifetime. A_i and τ_i are given by fitting of luminescent lifetime measurement.

Materials

Europium nitrate hexahydrate was purchased from Kishida Chemical, Ltd. Pyridine-2,6-dicarboxylic acid was obtained by Merck, Ltd. 2,6-diacetylpyridine, Lanthanum nitrate hexahydrate and Cerium nitrate hexahydrate were purchased from Wako Pure Chemical Industries, Ltd. Ethyl trifluoroacetate was bought from Tokyo Chemical Industry Co., Ltd. Praseodymium nitrate was got from Mitsuwa's pure chemicals, Ltd.

Preparation of compounds

2,6-Pyridine dicarboxylic acid dimethyl ester (Pmm)

Sulfuric acid (0.99 g) was added slowly into methanol suspension of pyridine-2,6-dicarboxylic acid (1.67 g, 10 mmol), and the mixture was refluxed for 2.5 hour. The colorless solution was cooled in the freezer to obtain white crystals. Crude product of Pmm was filtered, washed with methanol and recrystallized from hot methanol. Yield: 1.51 g (80.6 %)

$^1\text{H-NMR}$ (CDCl_3), δ : 8.15 ~ 8.24 ppm (3H; pyridine), δ : 3.88 ppm (6H; CH_3)

$\text{IR}(\text{v}/\text{cm}^{-1})$: 2964 b($\text{v}_{\text{C-H}}$), 1614 s($\text{v}_{\text{C=O}}$), 1559 s($\text{v}_{\text{C=C}}$)

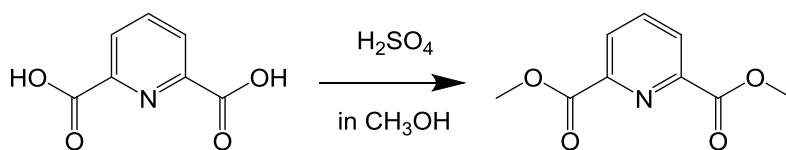


Fig. 2. Scheme of Pmm synthesis

2,6-di(acetoacetyl)pyridine (**H₂L**)

Preparation of **H₂L** was carried out by a modification of a previously published method.²⁴ Pmm (7.70 g, 46 mmol) and sodium methoxide (14.3 g, 260 mmol) were mixed in diethyl ether. Acetone was added in the suspension and the mixture was refluxed for 3 hours. Yellow powder was filtered and dissolved in distilled water. 2mol/L hydroxy chloride solution was added to the yellow solution, and stirred for 6 hours at room temperature to give yellow solid of **H²L**. Yield: 4.92 g (56.0 %).

IR(ν/cm^{-1}): 2964 b($\nu_{\text{C-H}}$), 1614 s($\nu_{\text{C=O}}$), 1559 s($\nu_{\text{C=C}}$)

¹H-NMR (CDCl_3), δ : 7.97 ~ 8.19 ppm (3H; pyridine group), δ : 6.87 ppm (2H; CH_2 in β -diketone) δ : 2.29 ppm (6H; CH_3 group)

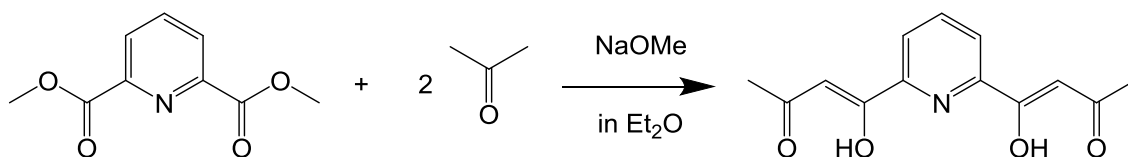


Fig. 3. Scheme of **H₂L** synthesis

[**La₃L₂(NO₃)₅(MeOH)₄**]·(**MeOH**)(**H₂O**)₂ (**La₃L**)

A methanol solution of $\text{La}(\text{NO}_3)_3 \cdot 6\text{H}_2\text{O}$ (86 mg, 0.2 mmol in 2 ml) was added to a solution of **H₂L** (36 mg, 0.14 mmol) in 2 ml methanol. The reaction mixture was diffused with diethyl ether to obtain yellow crystals of **La₃L**.

IR(ν/cm^{-1}): 2965 b($\nu_{\text{C-H}}$), 1618 s, 1509 s($\nu_{\text{C=O}}$), 1459 s($\nu_{\text{C=C}}$), 1313 s, 1285s(ν_{NO_3}).

[**Ce₃L₂(NO₃)₅(MeOH)₄**]·(**MeOH**)(**H₂O**) (**Ce₃L**)

Orange crystals of **Ce₃L** were obtained by the same method for **La₃L** except for using $\text{Ce}(\text{NO}_3)_3 \cdot 6\text{H}_2\text{O}$ (86 mg, 0.2 mmol) instead of $\text{La}(\text{NO}_3)_3 \cdot 6\text{H}_2\text{O}$.

IR(ν/cm^{-1}): 2965 b($\nu_{\text{C-H}}$), 1618 s, 1509 s($\nu_{\text{C=O}}$), 1459 s($\nu_{\text{C=C}}$), 1313 s, 1285s(ν_{NO_3}).

[**Pr₃L₂(NO₃)₅(MeOH)₄**]·(**MeOH**)(**H₂O**)₂ (**Pr₃L**)

Light yellow crystals of **Pr₃L** were obtained by the same method for **La₃L** except for using $\text{Pr}(\text{NO}_3)_3 \cdot 6\text{H}_2\text{O}$ (87 mg, 0.2 mmol) instead of $\text{La}(\text{NO}_3)_3 \cdot 6\text{H}_2\text{O}$.

IR(ν/cm^{-1}): 2965 b($\nu_{\text{C-H}}$), 1618 s, 1509 s($\nu_{\text{C=O}}$), 1459 s($\nu_{\text{C=C}}$), 1313 s, 1285s(ν_{NO_3}).

[Eu₃L₂(NO₃)₅(MeOH)₄]·MeOH (Eu₃L)

Yellow microcrystals of **Eu₃L** were obtained by the same method for **La₃L** except for using Eu(NO₃)₃·6H₂O (88 mg, 0.2 mmol) instead of La(NO₃)₃·6H₂O.

IR(ν/cm^{-1}): 2965 b($\nu_{\text{C-H}}$), 1509 s($\nu_{\text{C=O}}$), 1459 s($\nu_{\text{C=C}}$), 1313 s, 1285s(ν_{NO_3}).

2,6-di(1,1,1-trifluoro-acetoacetyl) pyridine (H₂L^F)

A mixture of sodium methoxide (1241 mg, 6 mmol) and ethyl trifluoroacetate (720 μl , 6 mmol) in tetrahydrofuran (40 ml) was stirred for 10 min, followed by the addition of 2,6-diacetylpyridine (484 g, 3 mmol). Then, the mixture was stirred at room temperature for 24 h. The resulting red solution was evaporated. 3% hydrochloric acid solution (50 ml) was added to red residue, and the resulting yellow precipitate was filtered off, washed with distilled water, and dried in a vacuum. Yield: 844 mg (79.5 %).

IR(ν/cm^{-1}): 1647 s, 1615 s, 1569 s, 1449 s, 1427 m ($\nu_{\text{O=C-C=C}}$, $\nu_{\text{C=C}}$ of arom. system), 1265 s, 1200 s, 1137s, 1094 s(ν_{CF_3}).

¹H-NMR (CDCl₃), δ : 8.12 ~ 8.34 ppm (3H; pyridine group), δ : 7.28 ppm (2H; CH₂ in β -diketone)

Elemental Analysis: Calculated (%); C 43.96, H 1.99, N 3.94; Found (%); C 44.12, H 2.01, N 4.00

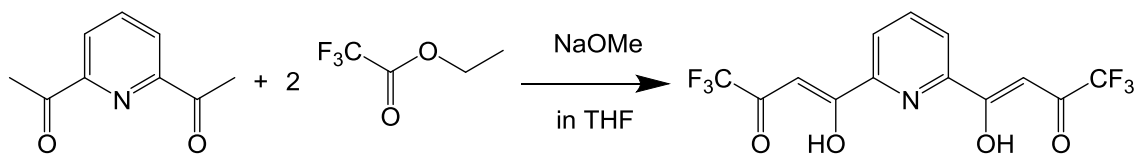


Fig. 4. Scheme of H₂L^F synthesis

[Eu₃L^F₂(NO₃)₅(H₂O)₂(MeOH)₂]·3MeOH (Eu₃L^F)

Methanolic solution of Eu(NO₃)₃·6H₂O (27mg, 0.06 mmol in 0.5 ml) was added to a solution of H₂L^F (14 mg, 0.04 mmol) in 0.5 ml methanol. Chloroform 20 ml was poured into the resulted red solution. After stand for several days, red needle crystals were obtained.

IR(ν/cm^{-1}): 1634 s, 1539 s, 1469 s, 1438 m ($\nu_{\text{O=C-C=C}}$, $\nu_{\text{C=C}}$ of arom. system), 1313 s, 1279 s(ν_{NO_3}), 1203 m, 1145 m, 1126 s(ν_{CF_3}).

Elemental Analysis: Calculated for C₅₈H₃₉N₁₄Cl₂Eu₆F₂₄O₅₉ (%); C 23.36, H 2.26, N

5.78; Found (%); C 23.37, H 2.41, N 5.25

Results and discussion

Characterization of Ln_3L

IR spectra

FT-IR spectrum of H_2L and Ln_3L ($\text{Ln} = \text{La} \sim \text{Pr}, \text{Eu}$) were shown in Fig. 5. The four Ln_3L showed same spectra each other (Fig. 5). The FT-IR spectrum of free H_2L shows enol bands of β -diketone at about 1620 cm^{-1} . In the complexes, the bands shifted to low frequency, which suggested coordination of β -diketone sites to Ln(III) ions. In addition, Ln_3L showed band for $\nu(\text{NO}_3^-)$ at around 1280 cm^{-1} .

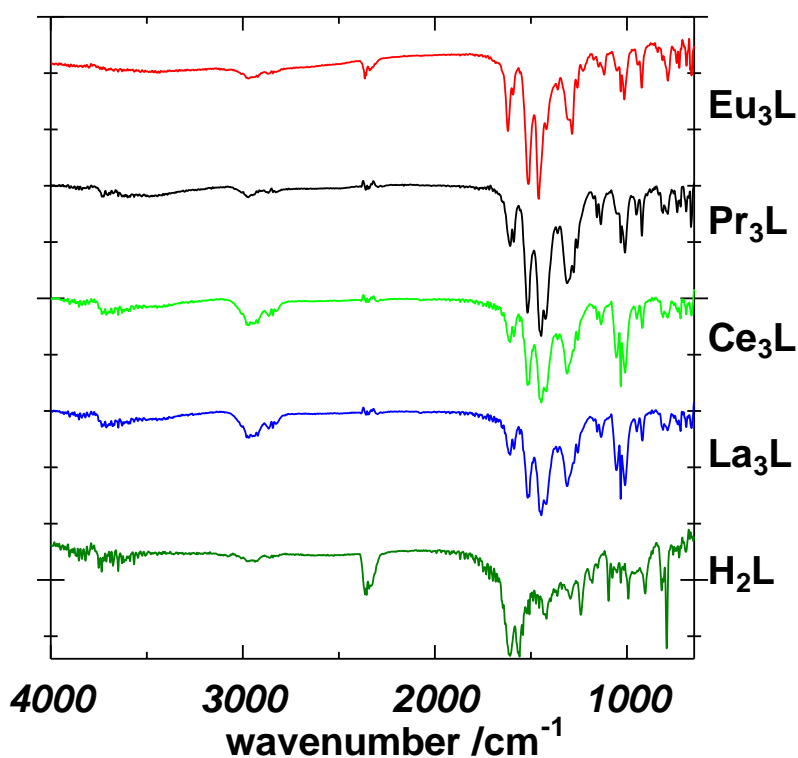


Fig. 5. FT-IR spectra of H_2L and Ln_3L ($\text{Ln} = \text{La}, \text{Ce}, \text{Pr}$ and Eu)

X-Ray Structure Analysis

Structures of Ln_3L are shown in Figs. 6-9, and crystal parameters and selected bond distances and angles are given in Tables 1-6. Single crystal structural analysis revealed that Ln_3L form a trinuclear structure with two deprotonated ligands

L^{2-} , three Ln(III) ions, five nitrate anions, and four coordinated MeOH. One central 2,6-diacylpyridine site and two side β -diketone sites coordinated to different Ln(III) ions, and central Ln(III) are linked with the side Ln(III) through enolate- and nitrate-bridges. Two nitrate anions bridged the Ln(III) ions in μ - η^1, η^2 mode. The side Ln(III) is in O_9 coordination environment with two β -diketone, one bidentate nitrate anions, two MeOH and one bridged nitrate anion. On the other hand, the central Ln(III) is in N_2O_{10} coordination environment with two 2,6-diacylpyridine sites, one bidentate nitrate anion and two bridged nitrate anions.

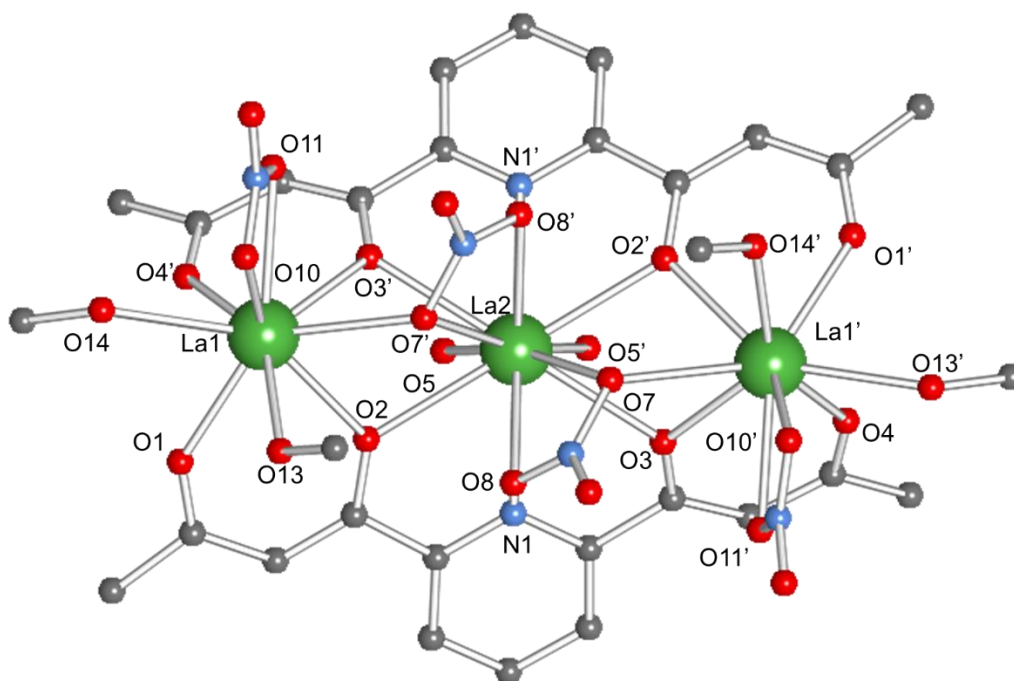


Fig. 6. Crystal structure of $[La_3L_2(NO_3)_5(MeOH)_4] \cdot (MeOH)(H_2O)_2$ (**La3L**)

Table 1. Crystallographic data for **La₃L**.

Chemical formula	C ₃₁ H ₄₄ La ₃ N ₇ O ₃₀
Formula weight	1403.40 g mol ⁻¹
Crystal size	0.084 × 0.127 × 0.199 mm ³
Crystal system	Monoclinic
Space group	C2/c
<i>a</i>	30.348(5) Å
<i>b</i>	12.586(2) Å
<i>c</i>	14.889(3) Å
<i>α</i>	90°
<i>β</i>	111.7393(17) °
<i>γ</i>	90°
<i>V</i>	5282.5(15) Å ³
<i>Z</i>	4
Density (calculated)	1.765 g/cm ³
Absorption coefficient	2.475 mm ⁻¹
<i>F</i> (000)	2728
Wavelength	0.71073 Å
Temperature	100(2) K
<i>R</i> 1	0.0325
<i>wR</i> 2	0.1316
Goodness-of-fit	1.2
Largest diff. peak and hole	4.665 and -0.759 eÅ ⁻³

Table 2. Bond length (Å) and angles (°) of **La₃L**.

La1-O1	2.502(2)	La2-O2	2.660(3)
La1-O2	2.559(2)	La2-O3	2.696(2)
La1-O3	2.607(3)	La2-O5	2.724(2)
La1-O4	3.049(3)	La2-O10	2.615(2)
La1-O7	2.652(3)	La2-O14	2.646(2)
La1-O8	4.0320(5)	La2-N1	2.612(2)
La1-O10	2.558(3)		
La1-O12	2.561(3)		
La1-O13	2.608(2)		

O1-La1-O2	70.53(8)	O2-La2-O3	109.77(7)
O1-La1-O3	119.49(9)	O2-La2-O2'	68.81(7)
O1-La1-O4	76.36(10)	O2-La2-O3'	66.04(7)
O1-La1-O7	151.43(9)	O2-La2-O5	112.80(7)
O1-La1-O8	126.09(9)	O2-La2-O5'	178.42(9)
O1-La1-O10	132.83(9)	O2-La2-O10	63.39(7)
O1-La1-O12	75.09(10)	O2-La2-O10'	116.76(7)
O1-La1-O13	73.88(9)	O2-La2-O14	111.60(7)
O2-La1-O3	65.71(7)	O2-La2-O14'	69.95(7)
O2-La1-O4	96.08(9)	O2-La2-N1	60.84(8)
O2-La1-O7	133.73(8)	O2-La2-N1'	119.86(8)
O2-La1-O8	140.89(8)	O3-La2-O3'	170.37(10)
O2-La1-O10	71.43(7)	O3-La2-O5	65.35(7)
O2-La1-O12	82.67(8)	O3-La2-O5'	105.30(7)
O2-La1-O13	144.41(8)	O3-La2-O10	126.72(7)
O3-La1-O4	69.19(8)	O3-La2-O10'	62.81(7)
O3-La1-O7	71.75(8)	O3-La2-O14	115.78(7)
O3-La1-O8	114.25(8)	O3-La2-O14'	71.20(7)
O3-La1-O10	65.97(7)	O3-La2-N1	59.71(8)
O3-La1-O12	134.33(8)	O3-La2-N1'	116.06(8)
O3-La1-O13	136.01(9)	O5-La2-O5'	48.35(10)
O4-La1-O7	84.92(9)	O5-La2-O10	167.07(8)
O4-La1-O8	121.18(9)	O5-La2-O10'	123.82(7)
O4-La1-O10	134.67(8)	O5-La2-O14	126.76(7)
O4-La1-O12	150.10(9)	O5-La2-O14'	128.77(8)
O4-La1-O13	74.99(10)	O5-La2-N1	70.32(8)
O7-La1-O8	48.70(9)	O5-La2-N1'	68.26(8)
O7-La1-O10	75.42(8)	O10-La2-O10'	65.88(10)
O7-La1-O12	117.42(9)	O10-La2-O14	46.77(7)
O7-La1-O13	80.59(9)	O10'-La2-O14	63.79(8)
O8-La1-O10	73.64(8)	O10-La2-N1	118.50(8)
O8-La1-O12	70.88(9)	O10'-La2-N1	99.98(8)
O8-La1-O13	64.91(9)	O14-La2-O14'	95.68(11)
O10-La1-O12	73.36(8)	O14-La2-N1	160.64(8)
O10-La1-O13	138.31(9)	O14'-La2-N1	64.97(8)
O12-La1-O13	88.66(10)	N1-La2-N1'	134.39(12)

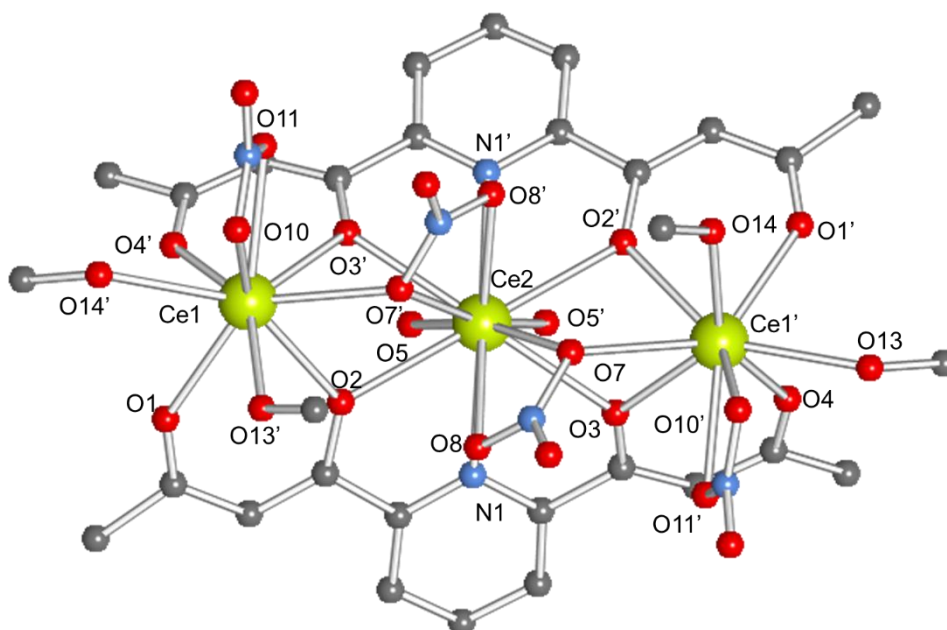


Fig. 7. Crystal structure of $[\text{Ce}_3\text{L}_2(\text{NO}_3)_5(\text{MeOH})_4] \cdot (\text{MeOH})(\text{H}_2\text{O})$ (**Ce3L**)

Table 3. Crystallographic data for **Ce3L**.

Chemical formula	$\text{C}_{32}\text{H}_{40}\text{Ce}_3\text{N}_7\text{O}_{29}$
Formula weight	1407.07 g mol ⁻¹
Crystal size	0.03 × 0.09 × 0.16 mm ³
Crystal system	Monoclinic
Space group	$C2/c$
<i>a</i>	30.133(6) Å
<i>b</i>	12.694(2) Å
<i>c</i>	14.855(3) Å
α	90°
β	111.479(2) °
γ	90°
<i>V</i>	5287.5(17) Å ³
<i>Z</i>	4
Density (calculated)	1.768 g/cm ³
Absorption coefficient	2.631 mm ⁻¹
<i>F</i> (000)	2748
Wavelength	0.71073 Å
Temperature	100(2) K

<i>R</i> 1	0.0686
<i>wR</i> 2	0.2613
Goodness-of-fit on F2	1.2
Largest diff. peak and hole	8.167 and -3.125 eÅ ⁻³

Table 4. Bond length (Å) and angles (°) of **Ce3L**.

Ce1-O1	2.398(6)	Ce2-O2	2.585(5)
Ce1-O2	2.533(5)	Ce2-O3	2.594(5)
Ce1-O3	2.485(5)	Ce2-O5	2.621(5)
Ce1-O4	2.399(6)	Ce2-O7	2.704(5)
Ce1-O7	2.575(5)	Ce2-O8	2.690(6)
Ce1-O10	2.573(6)	Ce2-N1	2.633(6)
Ce1-O11	2.628(6)		
Ce1-O13	2.546(5)		
Ce1-O14	2.532(6)		
O1-Ce1-O2	71.25(18)	O2-Ce2-O2'	177.9(2)
O1-Ce1-O3	120.79(19)	O2-Ce2-O3	116.87(16)
O1-Ce1-O4	77.6(2)	O2-Ce2-O3'	63.31(16)
O1-Ce1-O7	132.30(18)	O2-Ce2-O5	69.83(15)
O1-Ce1-O10	151.70(19)	O2-Ce2-O5'	112.21(15)
O1-Ce1-O11	124.3(2)	O2-Ce2-O7	109.71(15)
O1-Ce1-O13	73.23(19)	O2-Ce2-O7'	68.41(15)
O1-Ce1-O14	74.3(2)	O2-Ce2-O8	65.45(16)
O2-Ce1-O3	65.59(16)	O2-Ce2-O8'	113.04(16)
O2-Ce1-O4	96.86(19)	O2-Ce2-N1	61.29(18)
O2-Ce1-O7	71.23(16)	O2-Ce2-N1'	119.67(18)
O2-Ce1-O10	133.34(18)	O3-Ce2-O3'	171.1(2)
O2-Ce1-O11	140.82(17)	O3-Ce2-O5	105.65(16)
O2-Ce1-O13	144.44(18)	O3-Ce2-O5'	65.76(16)
O2-Ce1-O14	84.05(18)	O3-Ce2-O7	62.77(15)
O3-Ce1-O4	69.70(18)	O3-Ce2-O7'	125.99(16)
O3-Ce1-O7	66.10(16)	O3-Ce2-O8	70.74(16)
O3-Ce1-O10	71.53(18)	O3-Ce2-O8'	115.59(16)
O3-Ce1-O11	114.79(18)	O3-Ce2-N1	59.87(18)

Table 5. Crystallographic data for **Pr₃L**.

Chemical formula	C ₃₀ H ₂₇ N ₇ O ₂₈ Pr ₃
Formula weight	1356.3
Crystal size	0.066 × 0.044 × 0.036 mm ³
Crystal system	Monoclinic
Space group	C2/c
<i>a</i>	30.354(7) Å
<i>b</i>	12.636(2) Å
<i>c</i>	14.836(3) Å
<i>α</i>	90°
<i>β</i>	111.631(9) °
<i>γ</i>	90°
<i>V</i>	5290(2) Å ³
<i>Z</i>	4
Density (calculated)	1.703 g/cm ³
Absorption coefficient	2.7973 mm ⁻¹
<i>F</i> (000)	2628
Wavelength	0.71075 Å
Temperature	140(2) K
<i>R</i> 1	0.047
<i>wR</i> 2	0.1509
Goodness-of-fit on <i>F</i> ²	1.109
Largest diff. peak and hole	1.39, -1.16 eÅ ³

Table 6. Bond length (Å) and angles (°) of **Pr₃L**.

Pr1-O1	2.383(5)	Pr2-O2	2.589
Pr1-O2	2.513(4)	Pr2-O3	2.593
Pr1-O3	2.467(4)	Pr2-O5	2.606
Pr1-O4	2.392(5)	Pr2-O7	2.698
Pr1-O7	2.578(4)	Pr2-O8	2.667
Pr1-O10	2.622(4)	Pr2-N1	2.634
Pr1-O12	2.571(5)		
Pr1-O13	2.516(5)		
Pr1-O14	2.551(4)		
O1-Pr1-O2	71.9(1)	O2-Pr2-O2'	177.1

O1-Pr1-O3	120.6(1)	O2-Pr2-O3	62.7
O1-Pr1-O4	76.5(2)	O2-Pr2-O3'	117.5
O1-Pr1-O7	132.9(1)	O2-Pr2-O5	70.1
O1-Pr1-O10	124.7(1)	O2-Pr2-O5'	112.7
O1-Pr1-O12	150.4(2)	O2-Pr2-O7	67.6
O1-Pr1-O13	74.7(2)	O2-Pr2-O7'	109.8
O1-Pr1-O14	73.2(2)	O2-Pr2-O8	65.6
O2-Pr1-O3	65.5(1)	O2-Pr2-O8'	112.3
O2-Pr1-O4	97.2(1)	O2-Pr2-N1	61.5
O2-Pr1-O7	70.6(1)	O2-Pr2-N1	119.8
O2-Pr1-O10	140.2(1)	O3-Pr2-O3	171
O2-Pr1-O12	133.4(1)	O3-Pr2-O5	105.7
O2-Pr1-O13	83.2(1)	O3-Pr2-O7	62.6
O2-Pr1-O14	145.2(1)	O3-Pr2-O8	70.9
O3-Pr1-O4	70.1(1)	O3-Pr2-O8'	115.5
O3-Pr1-O7	66.0(1)	O3-Pr2-N1	60.1
O3-Pr1-O10	114.5(1)	O3-Pr2-N1'	115.9
O3-Pr1-O12	71.5(1)	O5-Pr2-O3	65.5
O3-Pr1-O13	134.8(1)	O5-Pr2-O5	48.9
O3-Pr1-O14	136.5(1)	O5-Pr2-O7	123.6
O4-Pr1-O7	135.6(1)	O5-Pr2-O7'	167.3
O4-Pr1-O10	120.9(1)	O5-Pr2-O8	125.8
O4-Pr1-O12	84.2(2)	O5-Pr2-O8'	128.4
O4-Pr1-O13	149.5(2)	O5-Pr2-N1	67.9
O4-Pr1-O14	74.7(2)	O5-Pr2-N1'	70.6
O7-Pr1-O10	73.8(1)	O7-Pr2-O3	126.3
O7-Pr1-O12	76.3(1)	O7-Pr2-O7	65.8
O7-Pr1-O13	73.4(1)	O7-Pr2-O8	47.8
O7-Pr1-O14	137.8(1)	O7-Pr2-O8'	63.9
O10-Pr1-O12	49.6(1)	O7-Pr2-N1	100.5
O10-Pr1-O13	69.9(1)	O7-Pr2-N1'	118
O10-Pr1-O14	64.3(1)	O8-Pr2-O8'	97
O12-Pr1-O13	117.6(1)	O8-Pr2-N1	64.4
O12-Pr1-O14	80.3(2)	O8-Pr2-N1	161.4
O13-Pr1-O14	87.6(1)	N1-Pr2-N1'	134.2

UV-Vis spectra of H₂L and complexes

UV-Vis spectra of H₂L, deprotonated ligand (L²⁻), and **Eu₃L** in methanol are shown in Fig. 12. The absorption band at around 310 nm for H₂L is attributed to the π - π^* transition of β -diketonate. After addition of base to H₂L, the π - π^* band slightly changed. On the other hand, the band shifted to around 360 nm in **Eu₃L**, which suggested the coordination of L²⁻ to Eu(III) ions.

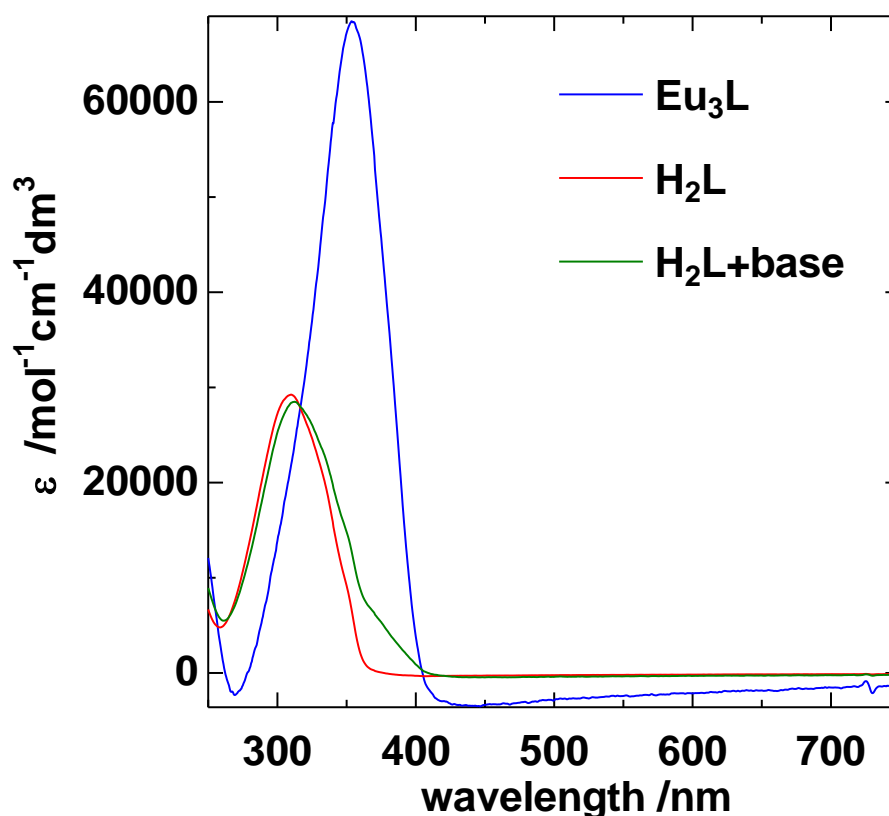


Fig. 9. Absorption spectra of **Eu₃L** (blue), H₂L (red) and deprotonated L²⁻ (green) in MeOH at room temperature

Photo luminescence properties

Photoluminescence spectrum of **Eu₃L** is shown in Fig. 13. The spectrum exhibited weak but very sharp peak, which is a characteristic signal of Eu(III) ion. The peak at 618 nm was attributed to the transition between the ⁵D₀ excited state and the ⁷F₂ ground state of Eu(III). However, the intensity of transition was very weak, which means that emission efficiency of **Eu₃L** is very low. In fact, the result of photoluminescence (PL) quantum yield was only 0.43 %. (Table 7.)

PL lifetime measurement suggested existence of two kinds of emission source, which well agrees with the molecular structure including two kinds of Eu(III) ions in O₉ and N₂O₁₀ coordination environment.

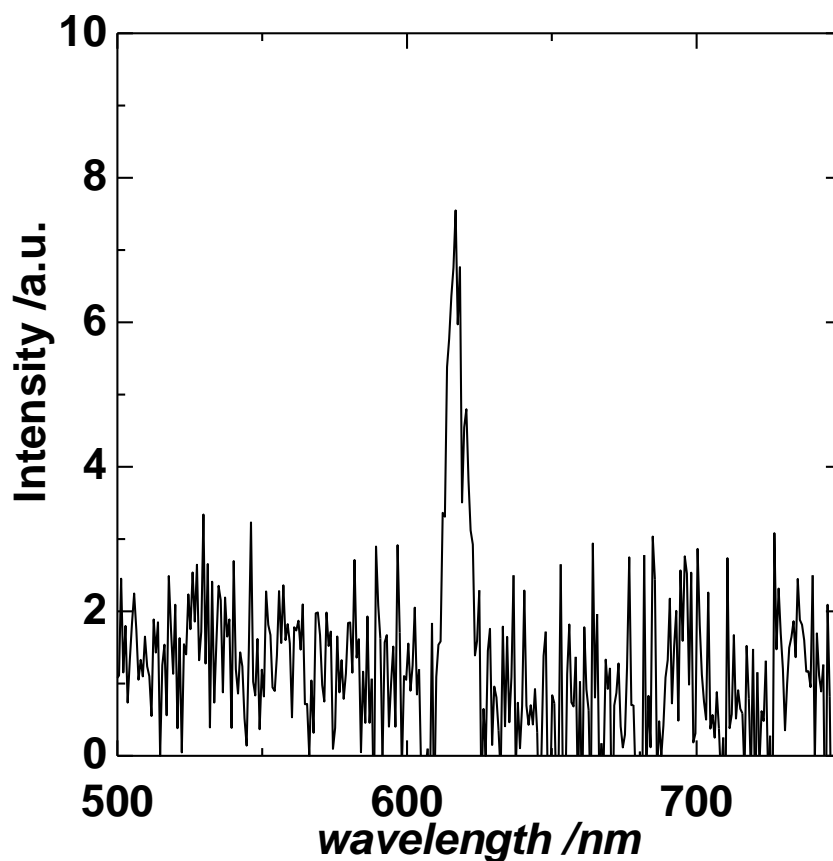


Fig. 10. Emission spectrum of **Eu₃L** in solid state at room temperature upon excitation at 360 nm.

Table 7. Excitation and emission wavelength of **Eu₃L** and identification of transition state.

λ_{ex} [nm]	λ_{em} [nm]	transition
340	618	$^5\text{D}_0 \rightarrow ^7\text{F}_2$

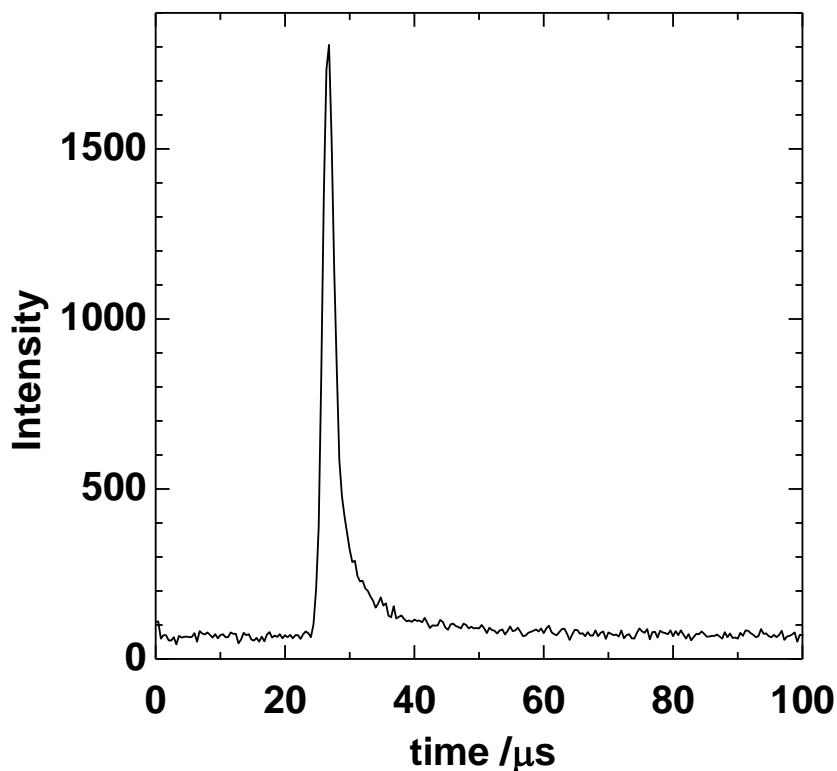


Fig. 11. PL lifetime spectrum of **Eu₃L**.

Table 8. PL quantum yields and lifetime of **Eu₃L**.

Compound	Φ [%]	τ_1 [ms]	τ_2 [ms]	A_1 [%]	A_2 [%]	χ^2
Eu₃L	0.43	7.1×10^{-4}	8.6×10^{-3}	91.39	8.61	0.94

Discussion about low PL quantum yield of **Eu₃L**

The low PL quantum yield of **Eu₃L** can be explained by two reasons: (i) metal to metal energy transfer, and (ii) vibrational relaxation of the excited state.

In the case of (i): three Eu(III) ions are closely arranged through enolate- and nitrate bridges (Table 8), in which excited energy transfer between Eu(III) ions occurs and the excited state is deactivated.

Table 9. Metal to metal distance of **Ln₃L**

	Distance / Å
La1-La2	4.032

La1-La1'	7.626
Ce1-Ce2	4.000
Ce1-Ce1'	7.547
Pr1-Pr2	4.003
Pr1-Pr1'	7.567

In the case of (ii), thermal vibration factor of ligand causes radiationless deactivation in excited state. Radiationless deactivation of lanthanide ion happens when electronic transition is occurred by superposition of wave function of ground state and that of excited state. The rate of electronic transition process is given by the following equation.²⁵

$$W_{\text{Radiationless Transition}} = \frac{2\pi\rho}{h} J^2 F$$

ρ , J and F mean density of status, overlap constant and Frank-Condon factor, respectively. Furthermore, F is given as the following equation,

$$F = \exp(-\gamma) \frac{\gamma^v}{v!}$$

γ means a variable that was used in approximate Hermite polynomials. N means vibrational quantum number. F is a function that depends on n , and the rate of vibrational deactivation is proportional to F . So, vibrational deactivation is inhibited by replacing easy vibrational group such as methyl group to hard vibrational groups such as trifluoromethyl group. According to the strategy, we designed another ligand H_2L^F for enhancing the quantum yield, and prepared analogous complex Eu_3L^F .

Characterization of Eu_3L^F

IR spectra of Eu_3L^F .

FT-IR spectrum of H_2L^F and Eu_3L^F were measured in solid state. The results show in Fig. 15.

The characteristic infrared absorption bands of the free H_2L and its lanthanide complexes which are useful for suggesting the mode of coordination of ligands. The FT-IR spectrum of the free H_2L^F shows bands at 1647, 1615, 1569, 1449, and 1427 cm^{-1}

attributed to free $\mu(\text{O}=\text{C}-\text{C}=\text{C})$ and free $\mu(\text{C}=\text{C})$ of aromatic system. In $\text{Eu}_3\text{L}^{\text{F}}$, the bands for $\mu(\text{O}=\text{C}-\text{C}=\text{C})$ and $\mu(\text{C}=\text{C})$ show a shift to low or high frequency at 1634, 1539, 1469 and 1438 cm^{-1} because of the coordination through metal-oxygen bond. In addition, the FT-IR spectrum of $\text{Eu}_3\text{L}^{\text{F}}$ shows band at 1285 for $\mu(\text{NO}_3^-)$, but that of $\text{H}_2\text{L}^{\text{F}}$ doesn't show. This result shows $\text{Eu}_3\text{L}^{\text{F}}$ contains nitric acid anion.

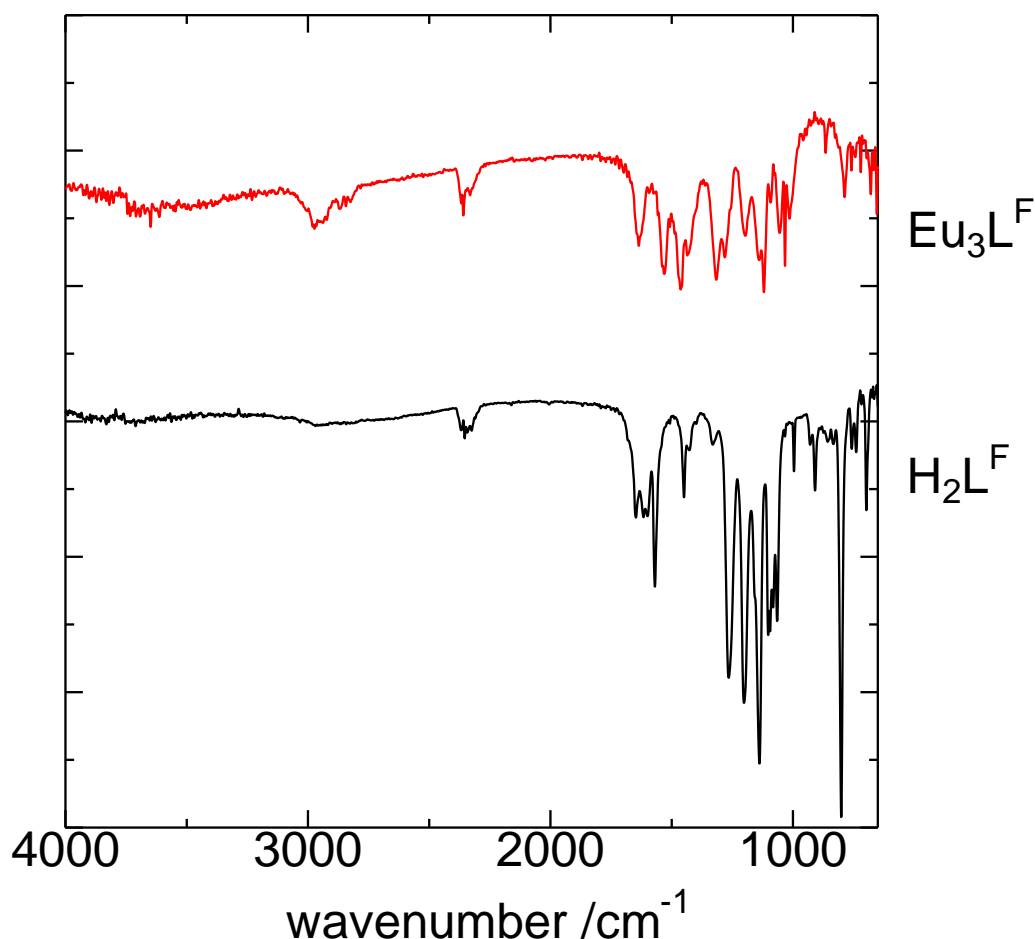


Fig. 12. FT-IR spectrum of $\text{H}_2\text{L}^{\text{F}}$ and $\text{Eu}_3\text{L}^{\text{F}}$.

X-Ray Structural Characterization

Structure of $\text{Eu}_3\text{L}^{\text{F}}$ and crystal parameter was showed in Fig. 16, and Table. 9. $\text{Eu}_3\text{L}^{\text{F}}$ is Trinuclear complex, and has two ligands, three lanthanide metals, five nitrate anions, and four solvents. Side metals are coordinated two β -diketone sites of $\text{H}_2\text{L}^{\text{F}}$, two nitrate anions, and two solvents which were methanol and water. One nitrate anion coordinated as bidentate ligands, and another coordinated as bridge-ligand with central metal. So, side metals were O_9 , 9 coordination. Central metal was coordinated two 2,

6-diacetyl pyridine sites of $\text{H}_2\text{L}^{\text{F}}$, and three nitrate anions. Two nitrate anions coordinated as bridge-ligand with side metals, and another coordinated as bidentate ligands. So, central metal was N_2O_{10} , 12 coordination

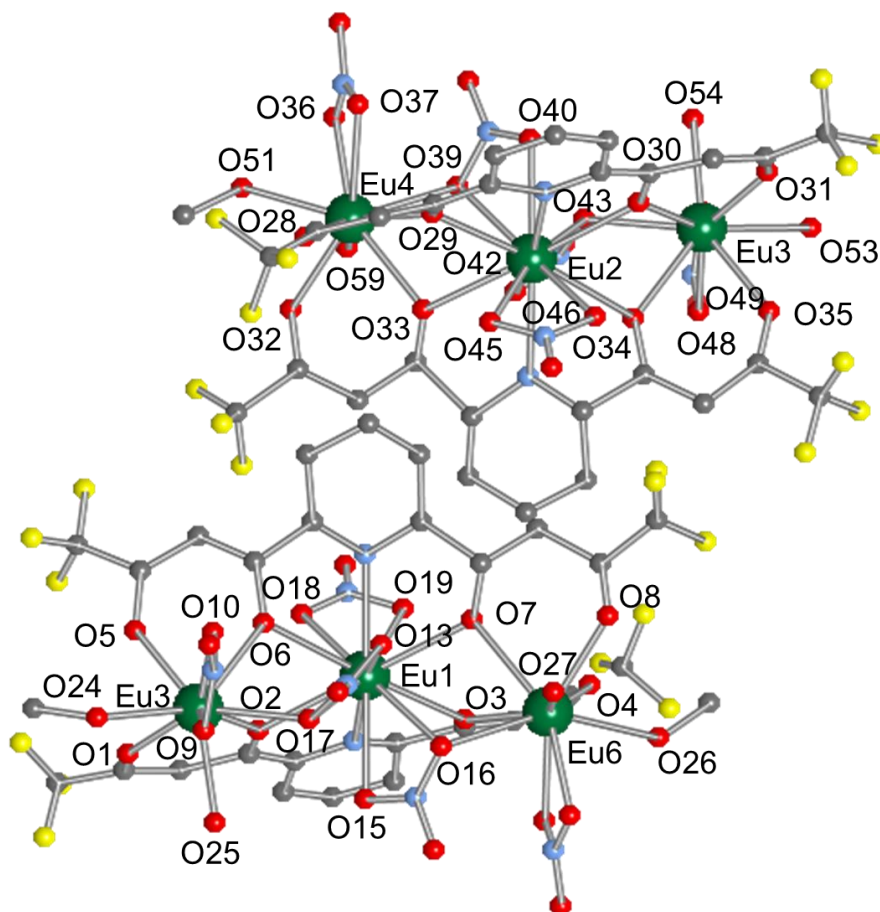


Fig. 13. Crystal structure of $[\text{Eu}_3\text{L}^{\text{F}}_2(\text{NO}_3)_5(\text{H}_2\text{O})_2(\text{MeOH})_2] \cdot 3\text{MeOH}$ (**Eu₃L^F**)

Table 10. Crystallographic data for **Eu₃L^F**

Chemical formula	$\text{C}_{58}\text{H}_{39}\text{Cl}_2\text{Eu}_6\text{F}_{24}\text{N}_{14}\text{O}_{59}$
Formula weight	$3314.69 \text{ g mol}^{-1}$
Crystal system	Monoclinic
Space group	$P2_1/c$
a	$30.133(6) \text{ \AA}$
b	$12.694(2) \text{ \AA}$
c	$14.855(3) \text{ \AA}$
α	90°

β	111.479(2) °
γ	90°
V	12456.(5) Å ³
Z	4
Density (calculated)	1.768 g cm ⁻³
Absorption coefficient	3.143 mm ⁻¹
$F(000)$	6340
Wavelength	0.71073 Å
Temperature	100K
$R1$	0.2328
$wR2$	0.5427
Goodness-of-fit on F^2	3.835
Largest diff. peak and hole	9.496 and -8.436 eÅ ⁻³

Table 11. Bond length (Å) and angles (°) of **Eu₃L^F**

Eu1-O2	2.581(16)	Eu2-O29	2.59(3)	Eu3-O1	2.41(2)
Eu1-O3	2.548(16)	Eu2-O30	2.566(16)	Eu3-O2	2.494(19)
Eu1-O6	2.58(2)	Eu2-O33	2.588(15)	Eu3-O5	2.34(3)
Eu1-O7	2.549(17)	Eu2-O34	2.548(17)	Eu3-O6	2.398(19)
Eu1-O12	2.54(2)	Eu2-O39	2.642(16)	Eu3-O9	2.47(3)
Eu1-O13	2.648(18)	Eu2-O40	2.488(18)	Eu3-O10	2.50(2)
Eu1-O15	2.53(2)	Eu2-O42	2.58(2)	Eu3-O12	2.47(2)
Eu1-O16	2.62(2)	Eu2-O43	2.513(18)	Eu3-O24	2.42(3)
Eu1-O18	2.58(2)	Eu2-O45	2.61(2)	Eu3-O25	2.31(2)
Eu1-O19	2.582(16)	Eu2-O46	2.557(16)	Eu3-N3	2.90(3)
Eu1-N1	2.576(19)	Eu2-N8	2.54(2)		
Eu1-N2	2.64(2)	Eu2-N9	2.60(2)		
Eu4-O28	2.55(3)	Eu5-O30	2.453(18)	Eu6-O3	2.396(15)
Eu4-O29	2.51(2)	Eu5-O31	2.30(2)	Eu6-O4	2.32(2)
Eu4-O32	2.345(18)	Eu5-O34	2.412(17)	Eu6-O7	2.46(2)
Eu4-O33	2.468(16)	Eu5-O35	2.30(2)	Eu6-O8	2.31(2)
Eu4-O36	2.50(3)	Eu5-O42	2.494(19)	Eu6-O16	2.418(17)
Eu4-O37	2.54(2)	Eu5-O48	2.52(2)	Eu6-O21	2.485(19)
Eu4-O40	2.52(2)	Eu5-O49	2.57(3)	Eu6-O22	2.53(3)

Eu4-O51	2.51(2)	Eu5-O53	2.40(2)	Eu6-O26	2.39(2)
Eu4-O52	2.37(2)	Eu5-O54	2.47(2)	Eu6-O27	2.46(3)
Eu4-N10	2.90(3)	Eu5-N14	2.86(5)		
O2-Eu1-O12	67.1(6)	O29-Eu2-O30	118.1(6)	O1-Eu3-O2	71.5(6)
O2-Eu1-O13	114.4(6)	O29-Eu2-O33	62.5(6)	O1-Eu3-O5	73.6(8)
O2-Eu1-O16	112.9(6)	O29-Eu2-O34	168.3(7)	O1-Eu3-O6	121.9(7)
O2-Eu1-O18	68.6(6)	O29-Eu2-O39	73.2(6)	O1-Eu3-O9	125.9(8)
O2-Eu1-O19	111.5(6)	O29-Eu2-O40	63.8(8)	O1-Eu3-O10	146.9(8)
O2-Eu1-O6	62.1(5)	O29-Eu2-O42	129.3(7)	O1-Eu3-O12	132.5(7)
O2-Eu1-O7	178.5(7)	O29-Eu2-O43	117.0(6)	O1-Eu3-O24	71.6(8)
O2-Eu1-N1	61.8(6)	O29-Eu2-O45	62.7(6)	O1-Eu3-N3	144.3(8)
O2-Eu1-N2	117.9(7)	O29-Eu2-O46	103.3(6)	O2-Eu3-O5	93.3(8)
O3-Eu1-O12	128.0(7)	O29-Eu2-N8	59.3(7)	O2-Eu3-O6	65.9(5)
O3-Eu1-O13	112.8(6)	O29-Eu2-N9	113.4(7)	O2-Eu3-O9	143.4(9)
O3-Eu1-O15	70.9(5)	O30-Eu2-O33	177.7(6)	O2-Eu3-O10	133.6(9)
O3-Eu1-O16	60.2(5)	O30-Eu2-O34	61.4(5)	O2-Eu3-O12	69.5(7)
O3-Eu1-O18	107.0(5)	O30-Eu2-O39	64.9(5)	O2-Eu3-O24	142.6(7)
O3-Eu1-O19	65.9(5)	O30-Eu2-O40	111.2(6)	O2-Eu3-O25	84.4(7)
O3-Eu1-O2	118.4(5)	O30-Eu2-O42	66.7(6)	O2-Eu3-N3	143.0(8)
O3-Eu1-O6	172.8(7)	O30-Eu2-O43	112.9(5)	O5-Eu3-O10	82.5(9)
O3-Eu1-O7	61.4(5)	O30-Eu2-O45	113.6(5)	O5-Eu3-O12	133.9(8)
O3-Eu1-N1	60.9(6)	O30-Eu2-O46	69.4(5)	O5-Eu3-O24	70.4(12)
O3-Eu1-N2	116.5(7)	O30-Eu2-N8	62.0(6)	O5-Eu3-O25	144.3(9)
O6-Eu1-O7	118.3(6)	O30-Eu2-N9	119.6(6)	O5-Eu3-O6	71.5(9)
O6-Eu1-O12	59.1(8)	O33-Eu2-O34	118.6(5)	O5-Eu3-O9	121.5(10)
O6-Eu1-O13	71.9(7)	O33-Eu2-O39	113.6(5)	O5-Eu3-N3	105.0(11)
O6-Eu1-O15	114.4(7)	O33-Eu2-O40	66.9(6)	O6-Eu3-O10	69.0(9)
O6-Eu1-O16	126.8(7)	O33-Eu2-O42	111.2(6)	O6-Eu3-O12	62.4(9)
O6-Eu1-O18	66.2(7)	O33-Eu2-O43	65.4(5)	O6-Eu3-O24	132.7(12)
O6-Eu1-O19	107.0(7)	O33-Eu2-O45	68.7(6)	O6-Eu3-O25	136.7(9)
O6-Eu1-N1	116.3(6)	O33-Eu2-O46	112.8(5)	O6-Eu3-O9	111.8(8)
O6-Eu1-N2	59.9(7)	O33-Eu2-N8	119.2(6)	O6-Eu3-N3	89.5(8)
O7-Eu1-O12	111.8(6)	O33-Eu2-N9	61.2(5)	O9-Eu3-O10	51.0(10)
O7-Eu1-O13	64.8(6)	O34-Eu2-O39	114.5(6)	O9-Eu3-O12	77.4(9)

O7-Eu1-O15	112.9(7)	O34-Eu2-O40	127.8(7)	O9-Eu3-O25	73.8(9)
O7-Eu1-O16	65.6(6)	O34-Eu2-O42	62.1(6)	O9-Eu3-N3	24.9(9)
O7-Eu1-O18	112.9(6)	O34-Eu2-O43	71.6(5)	O10-Eu3-O12	80.6(8)
O7-Eu1-O19	69.9(5)	O34-Eu2-O45	106.3(5)	O10-Eu3-O24	79.1(10)
O7-Eu1-N1	118.6(6)	O34-Eu2-O46	65.2(5)	O10-Eu3-O25	123.9(9)
O7-Eu1-N2	63.0(7)	O34-Eu2-N8	115.0(7)	O10-Eu3-N3	26.4(9)
O12-Eu1-O13	49.4(6)	O34-Eu2-N9	61.8(6)	O12-Eu3-O24	145.2(10)
O12-Eu1-O15	65.8(6)	O39-Eu2-O40	49.6(5)	O12-Eu3-O25	78.3(9)
O12-Eu1-O16	70.3(7)	O39-Eu2-O42	64.1(6)	O12-Eu3-N3	74.7(9)
O12-Eu1-O18	120.7(7)	O39-Eu2-O43	98.8(6)	O24-Eu3-O9	67.8(10)
O12-Eu1-O19	165.6(7)	O39-Eu2-O46	124.1(5)	O24-Eu3-O25	90.1(13)
O12-Eu1-N1	119.0(6)	O39-Eu2-N8	63.9(8)	O24-Eu3-N3	74.4(9)
O12-Eu1-N2	99.4(7)	O39-Eu2-N9	163.8(7)	O25-Eu3-O1	72.0(8)
O13-Eu1-O15	97.5(6)	O40-Eu2-O42	67.9(7)	O25-Eu3-N3	97.6(10)
O13-Eu1-O16	62.9(6)	O40-Eu2-O43	65.0(6)		
O13-Eu1-O18	129.4(6)	O40-Eu2-O45	121.4(6)		
O13-Eu1-O19	125.5(6)	O40-Eu2-O46	166.2(6)		
O13-Eu1-N1	161.8(7)	O40-Eu2-N8	100.4(8)		
O13-Eu1-N2	65.4(7)	O40-Eu2-N9	118.6(6)		
O15-Eu1-O2	65.8(6)	O42-Eu2-O43	49.4(5)		
O15-Eu1-O16	50.2(6)	O42-Eu2-O45	167.2(5)		
O15-Eu1-O18	124.7(6)	O42-Eu2-O46	122.6(5)		
O15-Eu1-O19	127.7(5)	O42-Eu2-N8	117.8(7)		
O15-Eu1-N1	64.5(6)	O42-Eu2-N9	102.4(7)		
O15-Eu1-N2	162.7(6)	O43-Eu2-O45	124.1(5)		
O16-Eu1-O18	166.6(5)	O43-Eu2-O46	128.2(5)		
O16-Eu1-O19	121.4(5)	O43-Eu2-N8	162.7(8)		
O16-Eu1-N1	101.2(6)	O43-Eu2-N9	65.0(6)		
O16-Eu1-N2	118.1(7)	O45-Eu2-O39	128.2(6)		
O18-Eu1-N1	67.3(6)	O45-Eu2-O46	50.1(5)		
O18-Eu1-N2	69.7(6)	O45-Eu2-N8	70.8(7)		
O18-Eu1-O19	49.3(5)	O45-Eu2-N9	66.0(7)		
O19-Eu1-N1	69.3(6)	O46-Eu2-N8	67.2(8)		
O19-Eu1-N2	68.2(7)	O46-Eu2-N9	70.0(6)		
N1-Eu1-N2	132.7(7)	N8-Eu2-N9	132.3(9)		

Optical measurements

UV-Vis absorption of $\text{H}_2\text{L}^{\text{F}}$ and complexes

UV-Vis absorption spectra of $\text{H}_2\text{L}^{\text{F}}$, deprotonated ligand ($\text{L}^{\text{F}2-}$), and $\text{Eu}_3\text{L}^{\text{F}}$ were measured with these methanol solutions. The results showed in Fig. 17.

$\text{H}_2\text{L}^{\text{F}}$ showed two absorption peaks at 275 nm and 345 nm. Deprotonated $\text{H}_2\text{L}^{\text{F}}$ adding base (Triethylamine) showed absorption shoulder at 275nm, and absorption peak at 336 nm. The absorption peak at 336 nm of $\text{L}^{\text{F}2-}$ was stronger than that of H_2L at 345 nm. The absorptions around 340 nm of $\text{H}_2\text{L}^{\text{F}}$ and $\text{L}^{\text{F}2-}$ were attributed to the singlet-singlet $\pi-\pi^*$ electronic transition of the aromatic rings in the bis- β -diketonate. From this result, the absorption peak at 345 nm was suggested to relate with proton at bis- β -diketone of $\text{H}_2\text{L}^{\text{F}}$. Compared with the ligand, the maximum absorption peaks were red-shifted for $\text{Eu}_3\text{L}^{\text{F}}$ (350 nm), which was attributed to the perturbation induced by the coordination of the Eu^{3+} ion.

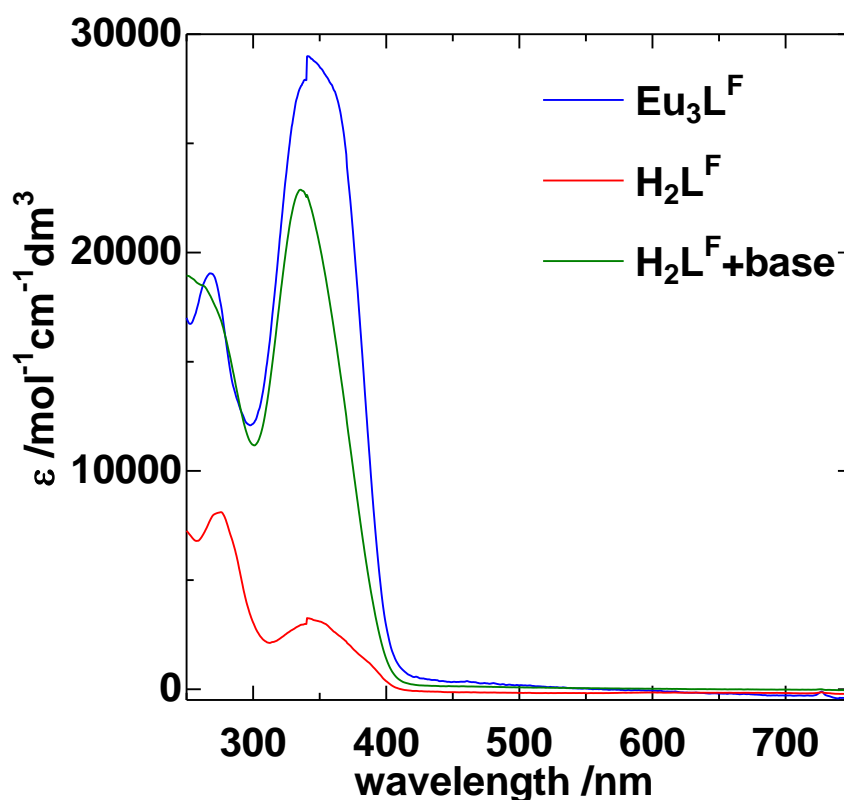


Fig. 14. Absorption spectrum of $\text{Eu}_3\text{L}^{\text{F}}$ (blue), H_2L (red) and deprotonated L^{2-} (green) in MeOH at room temperature.

Photo luminescence properties

Photoluminescence spectrum of **Eu₃L^F** show in Fig. 18 and Table. 12. The spectrum was very sharp, and this is one of characteristic of Eu(III) ion. So, this spectrum was suggested that this emission came from Eu(III) ion. The narrow bands observed in the emission spectrum at 578, 593, 614, 649, and 688 nm are transitions between the ⁵D₀ excited state and the different J levels of the ground term ⁷F_J (J = 0 ~ 4 respectively) of the europium.

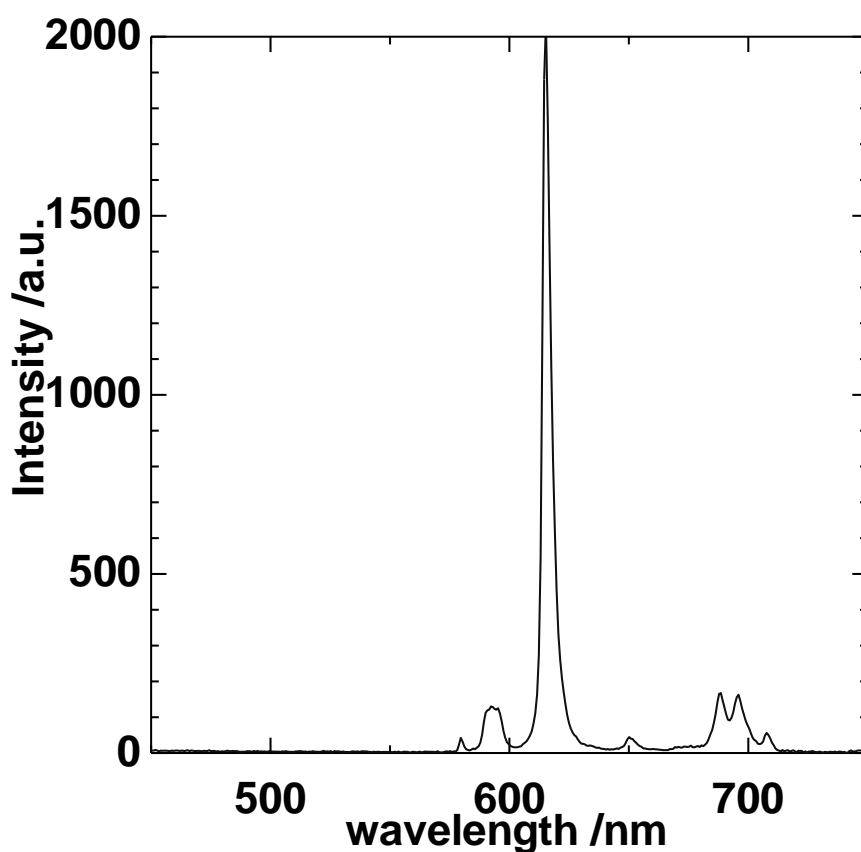


Fig. 15. Emission spectrum of **Eu₃L^F** in solid state at room temperature upon excitation at 340nm.

Table 12. Excitation and emission wavelength of **Eu₃L^F** and identification of transition state.

λ_{ex} [nm]	λ_{em} [nm]	transition
----------------------------	----------------------------	------------

340	578	$^5D_0 \rightarrow ^7F_0$
	593	$^5D_0 \rightarrow ^7F_1$
	614	$^5D_0 \rightarrow ^7F_2$
	649	$^5D_0 \rightarrow ^7F_3$
	688	$^5D_0 \rightarrow ^7F_4$

Photoluminescence luminescent quantum yield and emission lifetime of **Eu₃L^F** showed on Table. 13. PL quantum yield of **Eu₃L^F** was higher than that of Eu₃L. This is suggested that thermal vibration of ligands have an effect on luminous efficiency of europium complex. H₂L have more C-H bonds that are easy to vibrate than H₂L^F.

PL lifetime measurement is expected two kinds of emission source, and this result agree with that there are two kinds of coordination environment, O₉ and N₂O₁₀.

Table 13. PL quantum yields and lifetime of **Eu₃L^F**.

Compound	Φ [%]	τ_1 [ms]	τ_2 [ms]	A ₁ [%]	A ₂ [%]	χ^2
Eu₃L^F	8.07	0.22	0.43	83.71	16.29	1.15

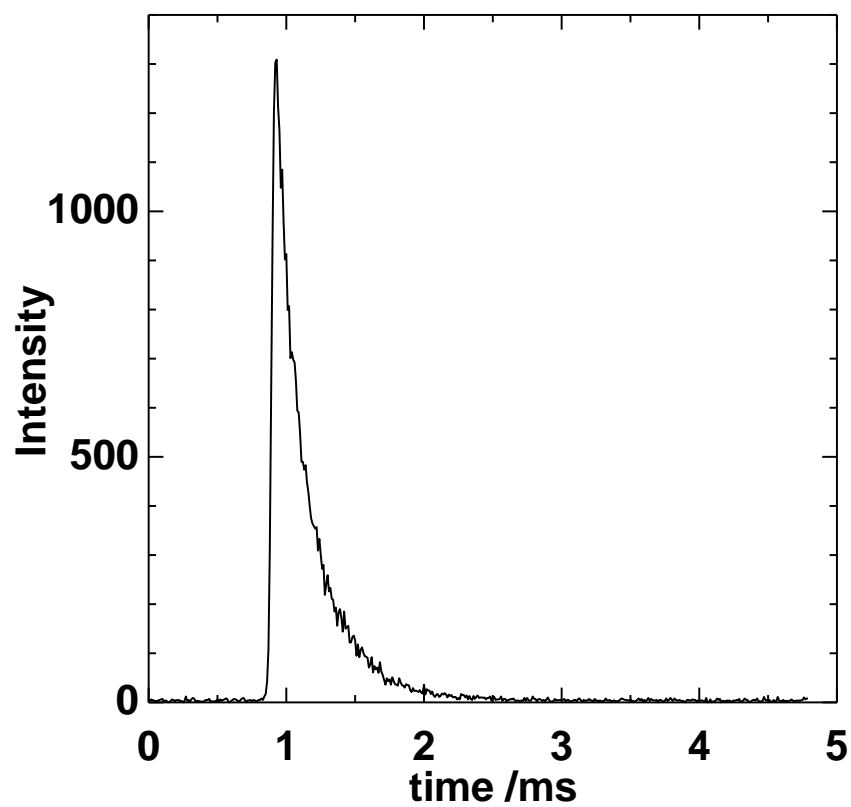


Fig. 16. PL lifetime spectrum of $\text{Eu}_3\text{L}^{\text{F}}$

Conclusion

Novel trinuclear complexes $[\text{Ln}_3\text{L}_2(\text{NO}_3)_5(\text{MeOH})_4] \cdot n\text{solv}$ (**Ln₃L**) (Ln = La, Ce, Pr, Eu) and $[\text{Eu}_3\text{L}^{\text{F}}_2(\text{NO}_3)_5(\text{H}_2\text{O})_3(\text{MeOH})] \cdot 3\text{MeOH}$ (**Eu₃L^F**) were successfully prepared by using linear multidentate ligands, 2,6-di(acetoacetyl)pyridine (**H₂L**) and 2,6-di(1,1,1-trifluoroacetoacetyl) pyridine (**H₂L^F**). In these structures, two kinds of Ln(III) ions: the central and side Ln(III) ions, were in N_2O_{10} and O_9 coordination environment, respectively. **Eu₃L** and **Eu₃L^F** showed characteristic Eu(III) red emission with PL quantum yield (QY) of 0.43 % and 8.07 %, respectively. One of the main factors for the very low QY of **Eu₃L** is supposed to be thermal vibration of L^{2-} , in particular of methyl groups. In the case of **Eu₃L^F**, the methyl groups of L^{2-} were substituted to the trifluoromethyl groups, which improved QY with suppressing the vibrational relaxation as expected. The ligand modification achieved a limited success in improving QY, but the QY was still low. Energy transfer between Eu(III) ions would be an additional suppressing factor of emission. In the tri-nuclear complexes, metal ions are located closely, which intrinsically include the energy transfer problem due to metal-to-metal interaction. To solve the problem, we are developing a rational synthetic method of hetero-lanthanide multinuclear complexes. Such compounds are expected to show high QY emission with utilizing the energy transfer between different Ln(III) ions or exhibit multicolor emission depending on combination of Ln(III) ions. In both cases, our approach would give significant insights for developing highly-effective light emission element materials.

References

1. M. Schäferling, *Angewandte Chemie International Edition*, 2012, **51**, 3532-3554.
2. M.-W. Ahn, K.-S. Park, J.-H. Heo, J.-G. Park, D.-W. Kim, K. J. Choi, J.-H. Lee and S.-H. Hong, *Applied Physics Letters*, 2008, **93**, -.
3. Q. H. Zhang, J. Wang, C. W. Yeh, W. C. Ke, R. S. Liu, J. K. Tang, M. B. Xie, H. B. Liang and Q. Su, *Acta Materialia*, 2010, **58**, 6728-6735.
4. Y. Cao, Z. Zhao, J. Yi, C. Ma, D. Zhou, R. Wang, C. Li and J. Qiu, *Journal of Alloys and Compounds*, 2013, **554**, 12-20.
5. P. S. Dutta and A. Khanna, *Ecs Journal of Solid State Science and Technology*, 2013, **2**, R3153-R3167.
6. U. Caldiño, E. Álvarez, A. Speghini and M. Bettinelli, *Journal of Luminescence*, 2013, **135**, 216-220.
7. M. D. Ward, *Coordination Chemistry Reviews*, 2007, **251**, 1663-1677.
8. M. Pal, U. Pal, J. M. G. Jimenez and F. Perez-Rodriguez, *Nanoscale Research Letters*, 2012, **7**, 1.
9. W. Stambouli, H. Elhouichet, B. Gelloz and M. Férid, *Journal of Luminescence*, 2013, **138**, 201-208.
10. Y. Liu, D. Tu, H. Zhu and X. Chen, *Chemical Society reviews*, 2013, **42**, 6924-6958.
11. S. V. Eliseeva and J.-C. G. Bunzli, *Chemical Society Reviews*, 2010, **39**, 189-227.
12. H. Kataoka, T. Kitano, T. Takizawa, Y. Hirai, T. Nakanishi and Y. Hasegawa, *Journal of Alloys and Compounds*, 2014, **601**, 293-297.
13. S. J. Butler and D. Parker, *Chemical Society reviews*, 2013, **42**, 1652-1666.
14. N. Thejo Kalyani and S. J. Dhoble, *Renewable and Sustainable Energy Reviews*, 2012, **16**, 2696-2723.
15. H.-B. Xu, J.-G. Deng and Z.-N. Chen, *Inorganic Chemistry Communications*, 2012, **15**, 314-316.
16. Y. Liu, M. Pan, Q.-Y. Yang, L. Fu, K. Li, S.-C. Wei and C.-Y. Su, *Chem. Mater.*, 2012, **24**, 1954-1960.
17. K. Miyata, Y. Konno, T. Nakanishi, A. Kobayashi, M. Kato, K. Fushimi and Y. Hasegawa, *Angewandte Chemie-International Edition*, 2013, **52**, 6413-6416.
18. F. Le Natur, G. Calvez, C. Daignebonne, O. Guillou, K. Bernot, J. Ledoux, L. Le Polles and C. Roiland, *Inorganic chemistry*, 2013, **52**, 6720-6730.

19. Y. Suffren, D. Zare, S. V. Eliseeva, L. Guénée, H. Nozary, T. Lathion, L. Aboshyan-Sorgho, S. Petoud, A. Hauser and C. Piguet, *The Journal of Physical Chemistry C*, 2013, **117**, 26957-26963.
20. T. Shiga, N. Ito, A. Hidaka, H. Ōkawa, S. Kitagawa and M. Ohba, *Inorg. Chem.*, 2007, **46**, 3492-3501.
21. M. Ohba, N. Ohtsubo, T. Shiga, M. Sakamoto and H. Okawa, *Polyhedron*, 2003, **22**, 1905-1910.
22. T. Shiga, M. Ohba and H. Okawa, *Inorganic Chemistry Communications*, 2003, **6**, 15-18.
23. T. Shiga, M. Ohba and H. Okawa, *Inorg. Chem.*, 2004, **43**, 4435-4446.
24. D. E. Fenton, J. R. Tate, U. Casellato, S. Tamburini, P. A. Vigato and M. Vidali, *Inorg. Chim. Acta.*, 1984, **83**, 23-31.
25. Y. Hasegawa, Y. Wada and S. Yanagida, *Journal of Photochemistry and Photobiology C: Photochemistry Reviews*, 2004, **5**, 183-202.

Chapter 3

Synthesis and Multi-Emission Properties of Lanthanide-Boron Hetero-Nuclear Complexes

Abstract

Novel lanthanide-boron complexes $[\text{Ln}(\text{LBF}_2)_3(\text{solv})_n]$ ($\text{Ln}(\text{III}) = \text{La}, \text{Eu}, \text{Gd}$; **Ln-LBF₂**) were prepared with boron complex ligand (**HLBF₂**) derived from a multidentate ligand 3-(3-(4-methoxyphenyl)-3-oxopropanyl) benzoic acid (H_2L). **Eu-LBF₂** showed concentration and solvent dependent multi-emission based on B and Eu(III) centers. In the coordinating solvent such as acetone and DMF, **Eu-LBF₂** showed blue emission originated from boron complexes with weak emission attributed to Eu(III). In the non-coordinating solvent such as CH_2Cl_2 and acetonitrile, **Eu-LBF₂** showed red emission based on Eu(III) ion with weak emission of boron. The results suggested the coordination of solvent to Eu(III) suppressed energy transfer from boron to Eu(III). In the low concentration solution, **Eu-LBF₂** showed blue emission with weak emission of Eu(III). On the other hand, **Eu-LBF₂** showed red emission in the high concentration solution expect for DMF, which suggested an effect of intermolecular energy transfer. Furthermore, emission color was changed by addition of ligands to non-coordination solvent solution. Especially, multidentate ligands induced more sensitive response than monodentate one. The multi-color luminescent **Eu-LBF₂** successfully exhibited guest-dependent color change with high visibility. Comparison of emission properties between **Eu-LBF₂** and **Gd-LBF₂** revealed the 3-(3-(4-methoxyphenyl)-3-oxopropanyl) benzoic acid correlation between B and Eu(III); (i) Intersystem crossing between the excited S1 and T1 terms in B is enhanced by coordination to Ln(III) due to a heavy-atom effect, (ii) energy transfer occurs between the generated T1 term of B and excited T1 term of Eu(III). The mechanism allows to change the intensity of emissions from excited S1 term of B and T1 term of Eu(III) depending on the degree of energy transfer from B to Eu(III).

Introduction

Multi-emission materials showing plural emission peaks are expected to apply for not only luminescent materials such as LED,¹⁻³ but also sensing materials.⁴⁻⁷ Because the emission color is recognized by their wavelength and intensity, multi-emission materials having modulable intensity ratio of each emission bands are expected to apply for sensing and imaging. Hasegawa et al. reported Eu-Tb solid solution coordination polymer which exhibits wide thermal color change between green and red.⁸ Hamachi et al. developed dual emissive chemosensor based on FRET.⁹ This chemosensor exhibited a dual-emission signal change upon binding with strong affinity to nucleoside polyphosphates such as ATP. However, dual emissive compounds especially organic dual emissive compounds¹⁰⁻¹² show broad emission bands. On the other hand, lanthanide complexes show sharp emission bands depending on kinds of lanthanide ions.^{13,14} Consequently most of stimuli responsible dual-emission materials have been developed using lanthanide ions, e.g. Tb-Eu heteronuclear compounds exhibit temperature responsive emission^{15, 16} or lanthanide sensing complex whose emission intensity was changed by external stimuli such as ion.¹⁷⁻¹⁹ To develop novel stimuli responsible material which show highly visible color change, we planned to create novel lanthanide-boron hetero-nuclear complexes. The complexes consisting of boron and lanthanide complex modules are expected to show coupled dual emission and visible color change responding to external stimuli. Boron complexes show excellent optical properties due to extension of the π conjugation with rigid π -based structures.²⁰⁻²² Emission color of boron complex is tunable by molecular design, and some boron complexes show mechanochromic²³ and ion sensing properties.²⁴ On the other hand, emission color of lanthanide complexes is untenable and depends on kinds of lanthanide ion, and the emission intensity strongly depends on the energy transfer from ligands. The boron and lanthanide complex modules play different roles in the multi-color emission, in which two modules show not “individual” emissions but “coupled” emissions. Intramolecular energy transfer between boron and lanthanide complex modules is expected to be a 3-(3-(4-methoxyphenyl)-3-oxopropanoyl) benzoic acid mechanism for deliver such multi-color emission and highly visible stimuli-responsivity at the same time.

Here, we prepared novel lanthanide-boron hetero-nuclear complex $[\text{Ln}(\text{LBF}_2)_3(\text{solv})_n]$ ($\text{Ln}(\text{III}) = \text{La}, \text{Eu}, \text{Gd}$; **Ln-LBF₂**) and examined their emission properties and guest responsivity. The mechanism of wide color change of **Eu-LBF₂** was discussed based on the two processes, the intersystem crossing of excited state of

boron complex module and the energy transfer between excited states of boron and Eu(III) complex modules.

Experiments

Physical Measurements

Elemental analyses of carbon, hydrogen and nitrogen were carried out by the staff of technical support division graduate school of science, Kyushu University. All Single-crystal X-ray diffraction data were collected on a Bruker SMART APEX II ULTRA CCD-detector Diffractometer, a rotating-anode (Bruker Turbo X-ray source) with graphite-monochromated MoK α radiation ($\lambda = 0.71073 \text{ \AA}$) was used. A single crystal was mounted on a polymer film with liquid paraffin and the temperature kept constant under flowing N₂. All of the structures were solved by a standard direct method (XSHELL V6.3.1 crystallographic software package of the Bruker AXS) and expanded using Fourier techniques. Fullmatrixleast-squares refinements were carried out with anisotropic thermal parameters for all non-hydrogen atoms. All of the hydrogen atoms were placed in the measured positions and refined using a riding model. X-ray fluorescence analysis was carried out on a Rigaku ZSX-100S. Infrared spectra were measured with a JASCO FT/IR-4200 using ATR method. UV-Vis absorption and emission spectra were measured by JASCO V-630 and FP-8200. HNMR spectra were obtained with JEOL 600MHz.

Photoluminescence quantum yield measurements were carried out on C9920-02; Absolute quantum yield measurement system made by Hamamatsu Photonics K.K. at room temperature. PL quantum yield was calculated with the following equation:

$$\Phi = \frac{\int I_{em} d\lambda}{\int (I_{ex}^{before} - I_{ex}^{after}) d\lambda}$$

I_{em} is the amount of photon from emission, I_{ex}^{before} is amount of photon from excitation light that nothing absorbed, and I_{ex}^{after} is amount of photon from excitation light that something absorbed.

Emission lifetime measurements were carried out on C11200 / Picosecond fluorescence lifetime measurement system at room temperature. Theoretical value of emission lifetime was calculated with the following equation.

$$\sum_i A_i \exp(-\frac{t}{\tau_i})$$

A_i is a coefficient, t is current time, τ_i is emission lifetime. A_i and τ_i are given by

fitting of luminescent lifetime measurement.

Materials

All chemical resources are purchased and used without purification.

Preparation of compounds

3-(3-(4-methoxyphenyl)-3-oxopropanpyl) benzoic acid methyl ester (HBam)

Dimethyl isophthalate (29.2 g, 150 mmol) and sodium methoxide 30% methanol solution (30 ml, 150 mmol) were mixed in 100ml THF. 4'-Methoxyacetophenone (21.0 g, 140mmol) was added in this suspension and mixture was refluxed for 3 hours. Yellow powder was filtered and dissolved in distilled water. 2mol/L hydroxy chloride solution was added to yellow solution, and stirred for 6 hours at room temperature. HBam was given as light brown solid by recrystallization in methanol. Yield: 27.8 g (59.2 %).

IR(ν/cm^{-1}): 1605 s($\nu\text{C=O}$)

$^1\text{H-NMR}$ (DMSO-d_6), δ : 8.60 ppm (s, 1H; aromatic ring), δ : 8.47 ppm (d, 1H; aromatic ring) δ : 8.21(d, 2H; aromatic ring in PhOCH_3), δ : 8.18 (d, 1H; aromatic ring), δ : 7.72 (t, 1H; aromatic ring), δ : 7.43 ppm (s, 1H; CH in β -diketone), δ : 7.19 ppm (d, 2H; aromatic ring in PhOMe), δ : 3.91 ppm (s, 3H; CH_3 group in COOCH_3), δ : 3.87 ppm (s, 3H; CH_3 group in PhOCH_3)

3-(3-(4-methoxyphenyl)-3-oxopropanpyl) benzoic acid (H_2L)

HBam (12.1 g, 40 mmol) was dissolved in 300 ml acetone. Solution of sodium hydroxide (4.0 g, 100 mmol) in 20 ml water was added to acetone solution, and mixture was stirred for overnight at room temperature. Yellow powder was filtered, and dissolved in distilled water. 2mol/L hydroxy chloride solution was added to yellow solution, and stirred for 6 hours at room temperature. H_2L was given as white solid by recrystallization in methanol. Yield: 8.3 g (71.8 %).

IR(ν/cm^{-1}): 1692 s ($\nu\text{C=O}$ in COOH), 1507 s ($\nu\text{C=O}$ in β -diketone)

$^1\text{H-NMR}$ (DMSO-d_6), δ : 17.30 ppm (s, 1H; OH in β -diketone), δ : 13.29 ppm (s, 1H; OH in COOH), δ : 8.60 ppm (s, 1H; aromatic ring), δ : 8.41ppm (d, 1H; aromatic ring) δ : 8.20 ppm (d, 2H; aromatic ring in PhOCH_3), δ : 8.16 ppm (d, 1H; aromatic ring), δ : 7.70 ppm (t, 1H; aromatic ring), δ : 7.33 ppm (s, 1H; CH in β -diketone), δ : 7.10 ppm (d, 2H; aromatic ring in PhOCH_3), δ : 3.86 ppm (s, 3H; CH_3 group in PhOCH_3)

HLBF₂

H₂L (3.08 g, 10.7 mmol) was suspended in 50 ml dichloromethane. Triethylamine (4ml, 28.5 mmol) was added to this suspension, and mixture was stirred for 2 hours. Boron trifluoride - ethyl ether complex (5 ml) was added to the mixture and stirring overnight. Dark yellow powder was filtered, and washed with chloroform. Yield: 3.41 g (95.4 %).

IR(ν/cm^{-1}): 1681 s ($\nu\text{C=O}$ in COOH), 1540 s ($\nu\text{C=O}$ in β -diketone), 1035 s($\nu\text{B-F}$)

¹H-NMR (DMSO-*d*₆), δ : 13.46 ppm (s, 1H; OH in COOH), δ : 8.76 ppm (s, 1H; aromatic ring), δ : 8.62ppm (d, 1H; aromatic ring) δ : 8.46 ppm (d, 2H; aromatic ring in PhOCH₃), δ : 8.30 ppm (d, 1H; aromatic ring), δ : 7.94 ppm (s, 1H; CH in β -diketone), δ : 7.80 ppm (t, 1H; aromatic ring), δ : 7.22 ppm (d, 2H; aromatic ring in PhOCH₃), δ : 3.95 ppm (s, 3H; CH₃ group in PhOCH₃)

Eu(LBF₂)₃(H₂O)₈(MeCN)₂ (Eu-LBF₂)

HLBF₂ (816 mg, 2.4 mmol) was suspended in 50 ml acetonitrile. Triethylamine (656 μl , 4.8 mmol) was added to this suspension to dissolve **HLBF₂**. Eu(NO₃)₃·6H₂O (356 mg, 0.8 mmol) was added to the mixture and stirred for overnight. Yellow precipitate was removed by filtration, filtrate was evaporated. The residue was washed with methanol, and filtered. Yellow precipitate was dissolved in dichloromethane. This solution was filtrated with celite, and filtrate was evaporated. **Eu-LBF₂** was obtained as yellow powder. The yield was 981 mg (86.6 %).

IR(ν/cm^{-1}): 1541 s ($\nu\text{C=O}$ in β -diketone), 1038 s($\nu\text{B-F}$)

Calcd. (%) C, 46.67; H, 4.27; N, 1.98 (Calcd. for Eu(LBF₂)₃(H₂O)₈(MeCN)₂)

Found (%) C, 46.85; H, 3.88; N, 1.79

La(LBF₂)₃(H₂O)₂(MeCN)(MeOH) (La-LBF₂)

Yellow powder of **La-LBF₂** was obtained by the same method for **Eu-LBF₂** except for using La (NO₃)₃·6 H₂O (346 mg, 0.8 mmol) instead of Eu(NO₃)₃·6H₂O. Yield: 364 mg (32.4 %).

IR(ν/cm^{-1}): 1541 s ($\nu\text{C=O}$ in β -diketone), 1038 s($\nu\text{B-F}$)

¹H-NMR (DMSO-*d*₆), δ : 8.72 ppm (s, 1H; aromatic ring), δ : 8.45ppm (broad, 1H; aromatic ring) δ : 8.39 ppm (d, 2H; aromatic ring in PhOCH₃), δ : 8.26 ppm (d, 1H; aromatic ring), δ : 7.84 ppm (s, 1H; CH in β -diketone), δ : 7.63 ppm (t, 1H; aromatic ring), δ : 7.16 ppm (d, 2H; aromatic ring in PhOCH₃), δ : 3.90 ppm (s, 3H; CH₃ group in

PhOCH₃)

Calcd. (%) C, 50.46; H, 3.84; N, 1.09

(Calcd. for La(LBF₂)₃(H₂O)₂(MeCN)(MeOH))

Found (%) C, 50.42; H, 3.49; N, 0.78

Gd(LBF₂)₃(H₂O)(MeCN)(MeOH)₃ (Gd-LBF₂)

Yellow powder of **Gd-LBF₂** was obtained by the same method for **Eu-LBF₂** except for using Gd (NO₃)₃·6 H₂O (362 mg, 0.8 mmol) instead of Eu(NO₃)₃·6H₂O. Yield: 364 mg (32.4 %).

IR(ν/cm⁻¹): 1541 s (νC=O in β-diketone), 1038 s (νB-F)

Calcd. (%) C, 49.75; H, 3.79; N, 1.07

(Calcd. for Gd(LBF₂)₃(H₂O)(MeCN)(MeOH)₃)

Found (%) C, 49.23; H, 3.41; N, 0.62

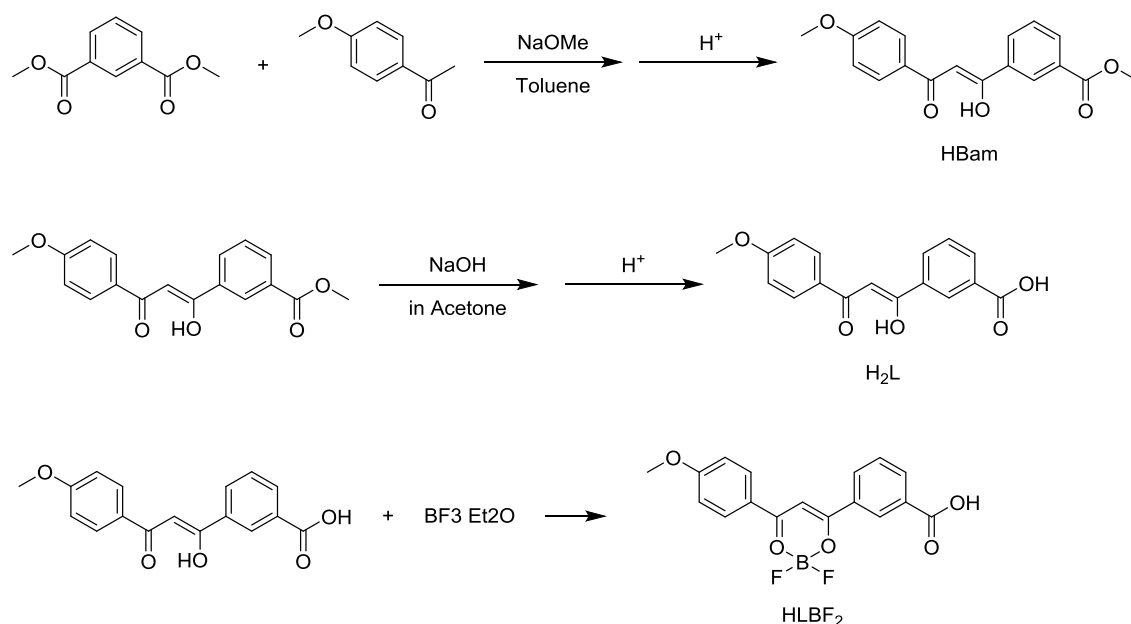


Fig. 1. Synthesis scheme of ligands and boron complex

Characterization

Crystal Structure of HLBF₂

Structure of **HLBF₂** is shown Fig. 2. BF₂ moiety coordinated with β-diketone site. This compound is planar structure. Hydrogen bonds were formed at each carboxylate moieties. From packing structure, **HLBF₂** was stacked with face to face π-π

interaction.

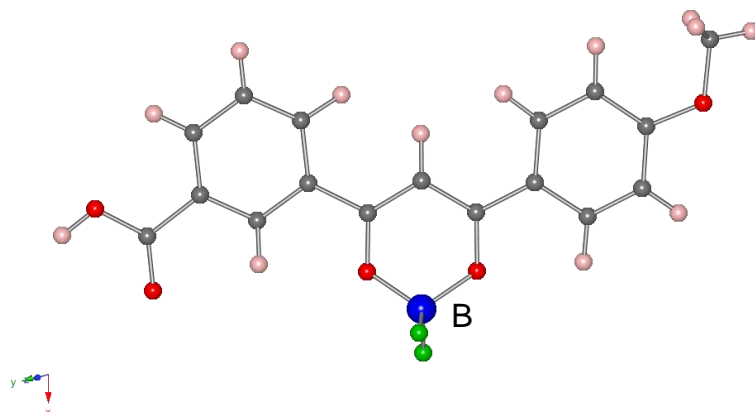


Fig. 2 Crystal structure of **HLBF₂**

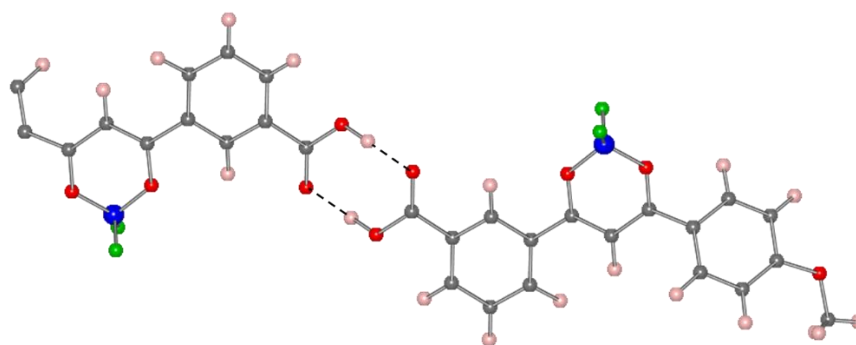


Fig. 3 Crystal structure of **HLBF₂**. Dashed lines mean hydrogen bonds.

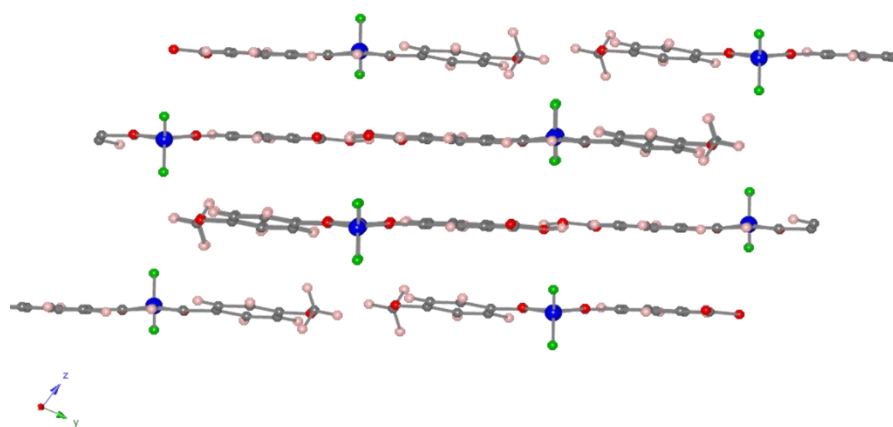


Fig. 4 Packing structure of **HLBF₂**.

Table 1 Cell parameters of **HLBF₂**

Name	HLBF ₂
Empirical formula	C ₁₇ H ₁₂ BF ₂ O ₅
Crystal system	triclinic
Space group	$P\bar{1}$
$a/\text{\AA}$	7.109(8)
$b/\text{\AA}$	8.606(11)
$c/\text{\AA}$	13.182(15)
$\alpha/^\circ$	72.715(14)
$\beta/^\circ$	78.053(14)
$\gamma/^\circ$	76.294(9)
$V/\text{\AA}^3$	739.9(15)
Z	2
GOF	1.113
$R1$	0.1066
wR	0.2602

Table 2 Bond distance and length of **HLBF₂**Bond Distances(\AA)

F001-B00P	1.364(6)	O003-C00B	1.304(5)
F002-B00P	1.380(7)	O003-B00P	1.490(6)

Bond Angles ($^\circ$)

F001-B00P-F002	110.9(4)	F002-B00P-O003	109.0(4)
F001-B00P-O003	109.3(4)	F002-B00P-O005	108.6(4)
F001-B00P-O005	108.7(4)	O003-B00P-O005	110.4(4)

IR Spectra of Eu-LBF₂

IR spectrum of **HLBF₂** showed peak of B-F bond near 1034 cm⁻¹, and peak shift of C=O bonds characterized β -diketone from 1500 cm⁻¹ to 1540 cm⁻¹. This peak shift of C=O bonds was suggested that BF₂ moiety coordinated with C=O of the β -diketone site.

IR spectrum (Fig. 5) of **Eu-LBF₂** showed peak of B-F bond near 1038 cm⁻¹ and C=O bond near 1541 cm⁻¹. This peak was suggested that BF₂ moiety exist after coordination with Eu³⁺ ion. In addition, peak of C=O bonds characterized carboxylic acid disappeared. This peak disappearance was suggested Eu³⁺ ion coordinated with -COO- moiety of **LBF₂**⁻. From these results, Eu³⁺ formed coordination bonds with boron complex.

Other lanthanide complexes, **La-LBF₂** and **Gd-LBF₂** showed same IR spectra as **Eu-LBF₂**. This result suggests that other lanthanide complex form same conformation with **Eu-LBF₂**. (Fig. 6)

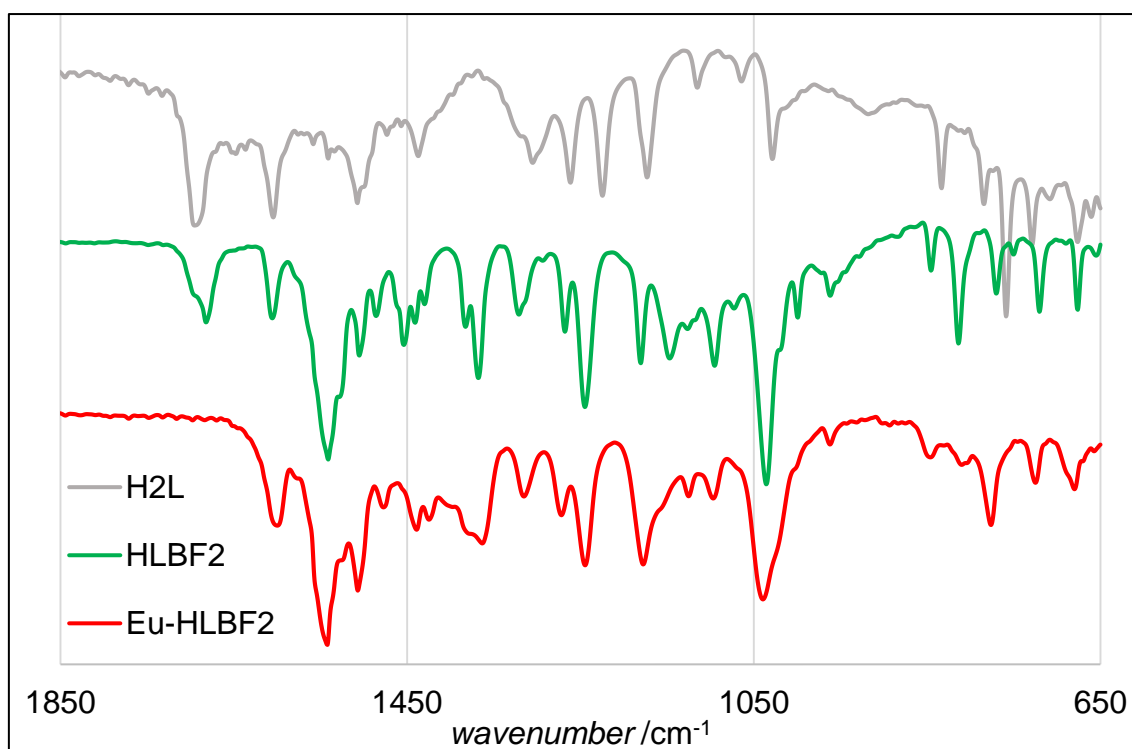


Fig. 5 IR spectra of H₂L (gray), **HLBF₂** (green), and **Eu-LBF₂** (red).

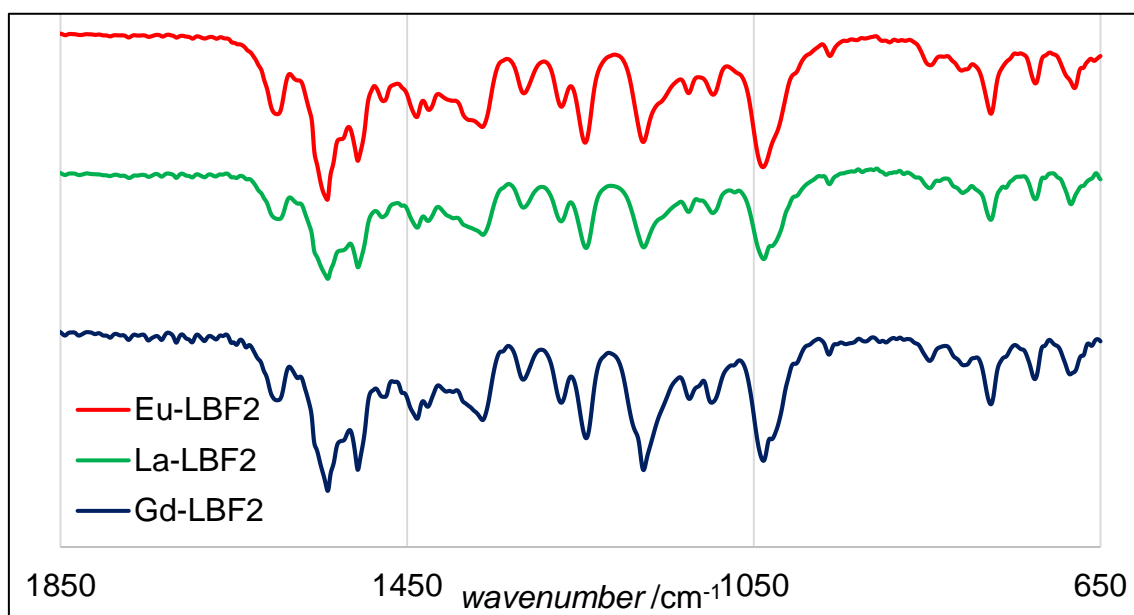


Fig. 6 IR spectra of **Eu-LBF₂** (red), **La-LBF₂** (green), and **Gd-LBF₂** (blue).

NMR spectra

NMR spectra of H_2L , **HLBF₂**, **La-LBF₂** and **Eu-LBF₂** was showed in Fig. 7 and Fig. 8. The spectrum of **Eu-LBF₂** showed mainly broad peaks. Metal complexes whose metal ion have lone pair electron usually show broad NMR spectra. So this result suggests that boron complex coordinate with Eu^{3+} ion.

On the other hand, NMR spectrum of **La-LBF₂** showed sharp peaks because La^{3+} ion have no lone pair electrons at any state. Compared with **HLBF₂**, Whole peaks shifted to high magnetic field. These peak shifts indicate that whole electron densities of boron complex were changed by forming coordination bonds with lanthanide ion. From these results, lanthanide ion coordinates with boron complex and keep the structure in the solvent.

From NMR, IR, and elemental analysis, the chemical formula of **Ln-LBF₂** was suggested $[\text{Ln}(\text{LBF}_2)_3(\text{H}_2\text{O})_2] (\text{solv.})_n$ ($\text{Ln} = \text{La}, \text{Gd}, \text{and Eu}$).

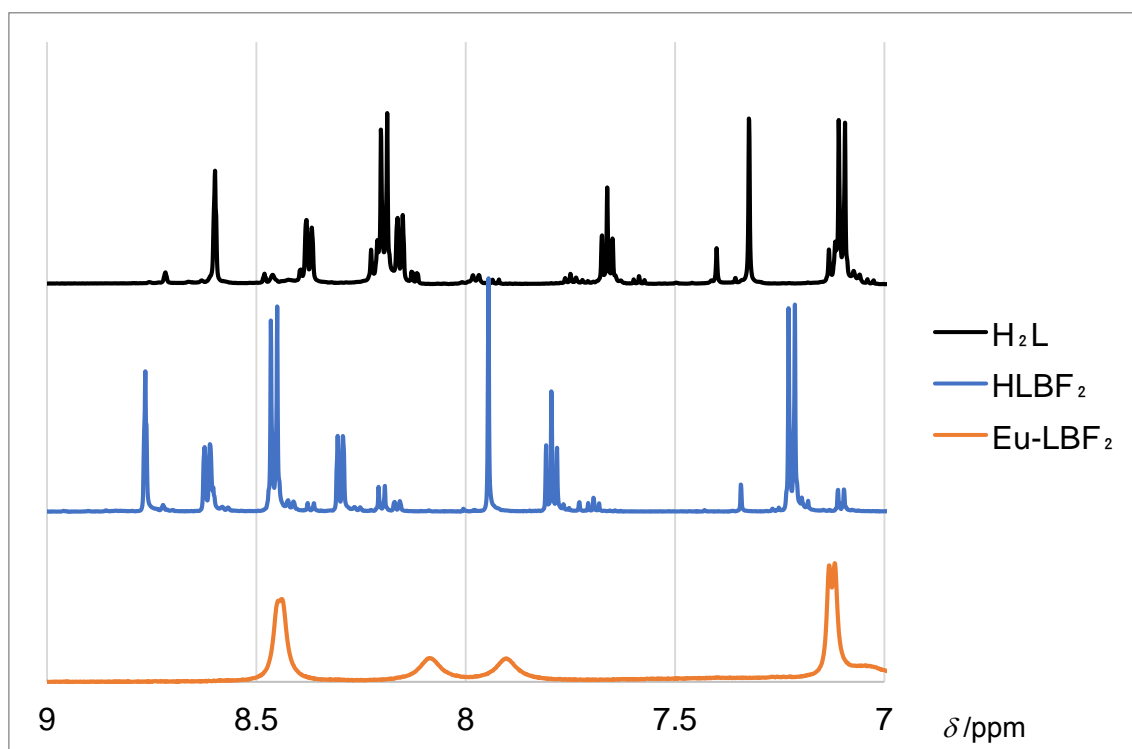


Fig. 7 NMR spectra of H_2L (black), HLBF_2 (blue), and Eu-LBF_2 (orange).

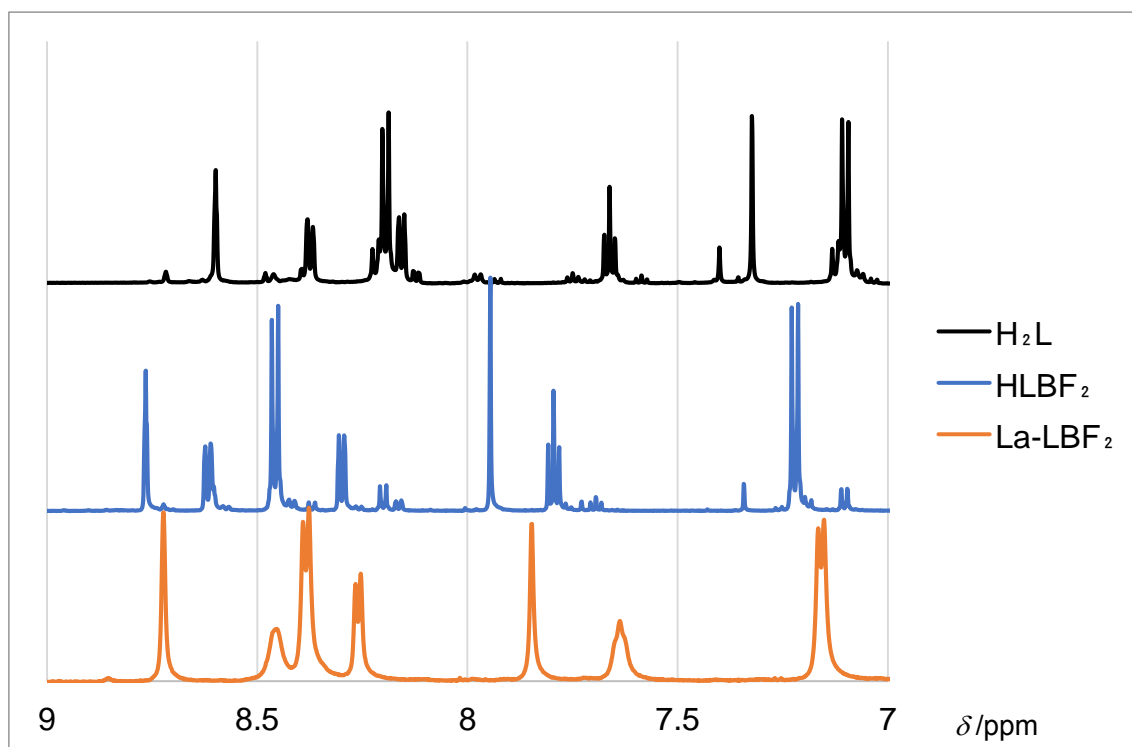


Fig. 8 NMR spectra of H_2L (black), HLBF_2 (blue), and Eu-LBF_2 (orange).

Discussion

Luminescence properties of **HLBF₂**

HLBF₂ showed blue emission in solution state (Figs. 9 and 10). In high polarity solvent, emission peak top was red shifted. Emission quantum yield in the low polarity solvent was much higher than that in high polarity solvent. This result suggests that the emission mechanism of **HLBF₂** is based on charge transfer (CT). In solid state, **HLBF₂** showed yellow emission. The emission peak top of solid **HLBF₂** is bathochromic shift to more than 100 nm. Emission lifetime of the solid state is much longer than that of the solution state. These results reflect the intermolecular interaction and packing structure of **HLBF₂** in the solid state (Fig. 4). This aggregation state is probably showed in high concentration solutions (Figs. 13-24, and Tables. 4-7).

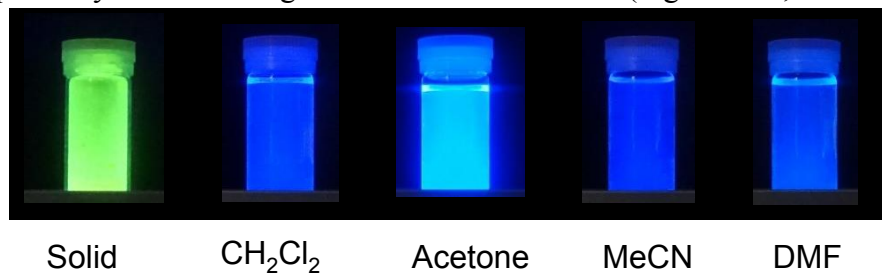


Fig. 9 Under UV irradiation of 20 $\mu\text{mol/L}$ MeCN solution of **HLBF₂**.

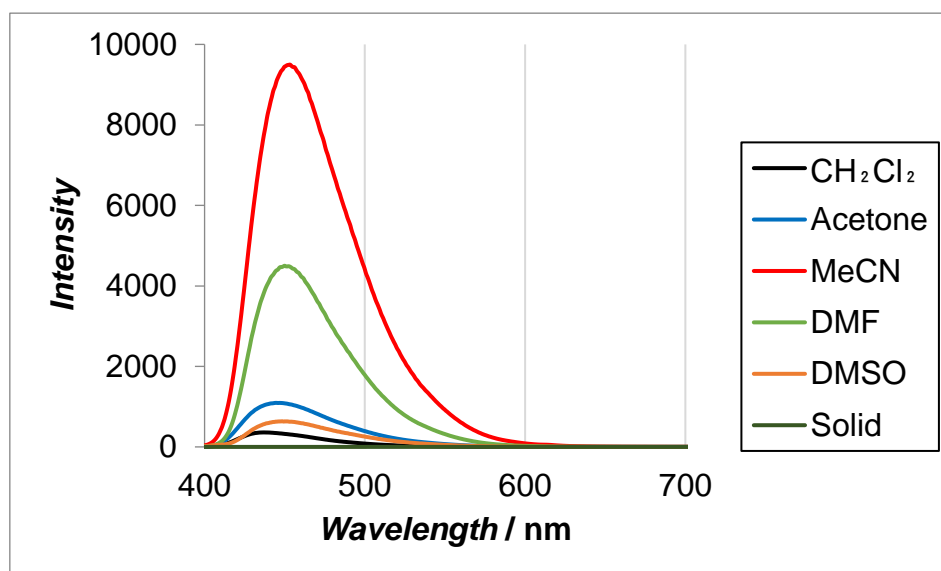


Fig. 10 PL spectra of solution and solid state of **HLBF₂**. In solution state, concentration is 20 $\mu\text{mol/L}$.

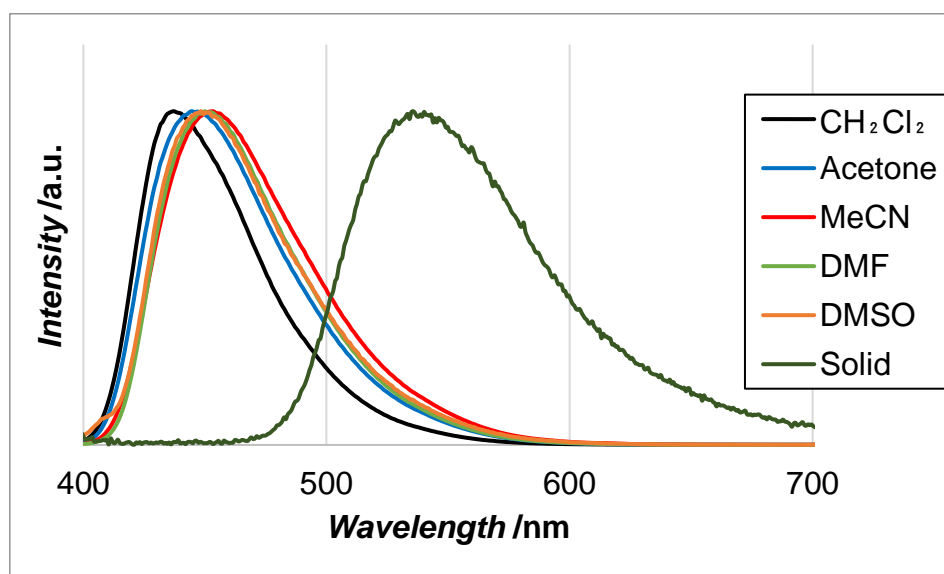


Fig. 11 Normalized PL spectra of solution and solid state of **HLBF₂**. In solution state, concentration is 20 $\mu\text{mol/L}$.

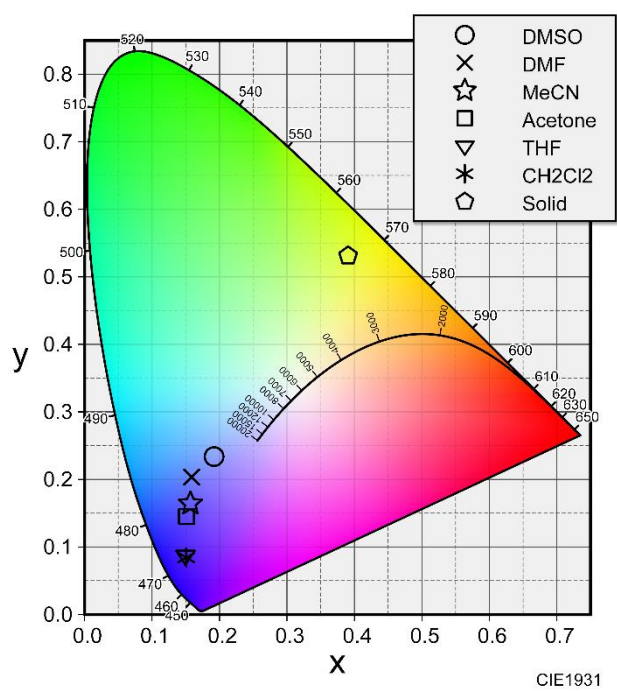


Fig. 12 Color diagram of solution and solid state of **HLBF₂**. In solution state, concentration is 20 $\mu\text{mol/L}$.

Table 3 Optical properties of 20 $\mu\text{mol/L}$ **HLBF₂** solutions.

	CH_2Cl_2	Acetone	MeCN	DMF	Solid
$\lambda_{\text{BF}_2} / \text{nm}$	437	444.5	453	450	554.3
Φ	<0.99	0.912	0.493	0.198	0.215
τ_1 / ns	2.3	2.5	1.4	1.6	1.5
τ_2 / ns	0.0	0.0	6.1	0.0	8.7
A_1	0.366	0.386	0.325	0.221	0.258
A_2	0.000	0.000	0.002	0.000	0.054
χ^2	1.501	1.487	1.299	1.438	1.055

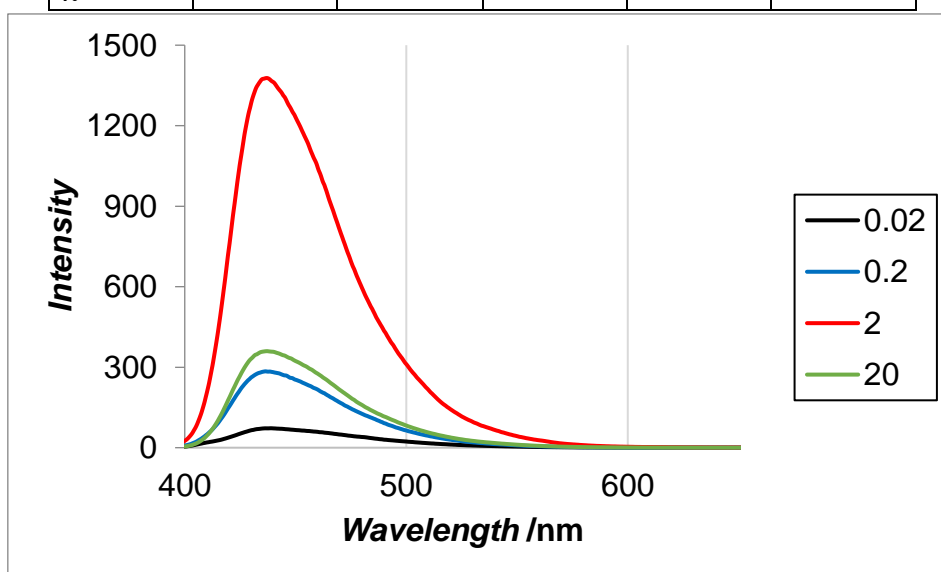


Fig. 13 PL spectra of CH_2Cl_2 solution of **HLBF₂**. Concentration is 0.02 $\mu\text{mol/L}$ to 20 $\mu\text{mol/L}$.

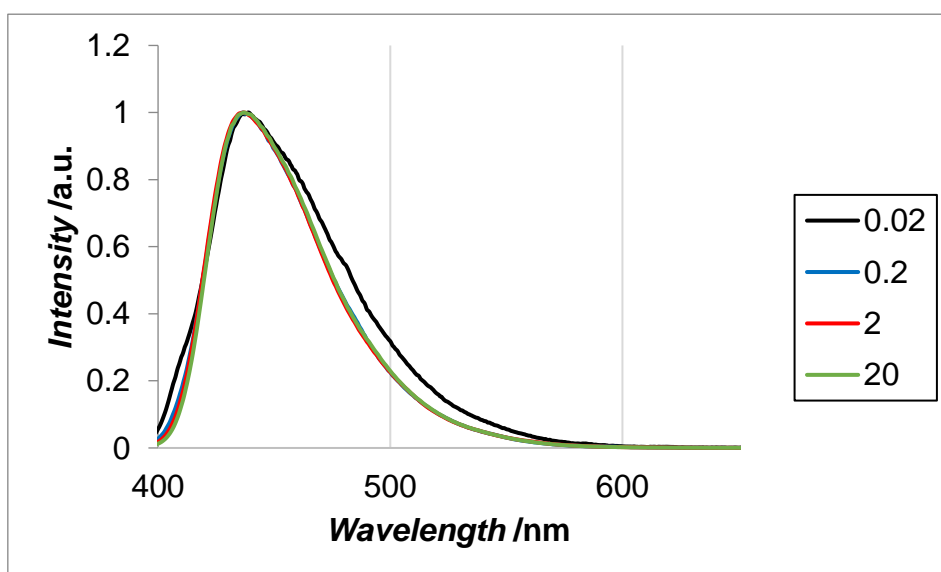


Fig. 14 Normalized PL spectra of CH₂Cl₂ solution of **HLBF₂**. Concentration is 0.02 $\mu\text{mol/L}$ to 20 $\mu\text{mol/L}$.

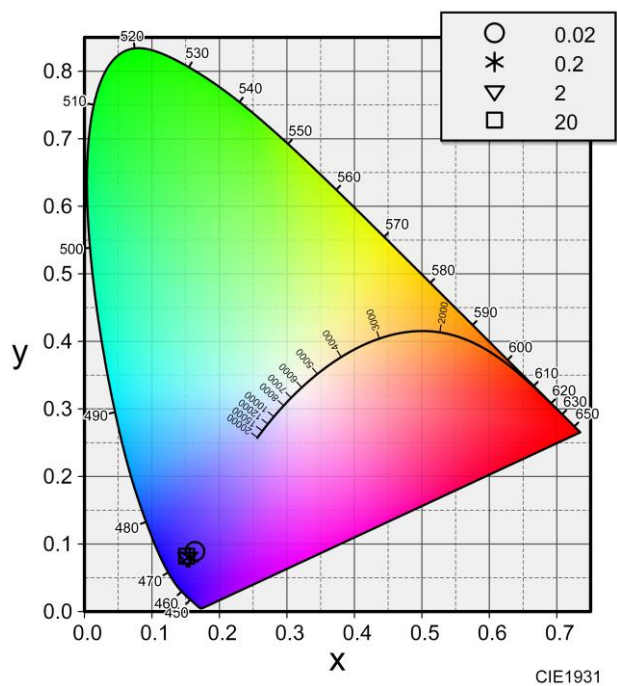


Fig. 15 Color diagram of CH₂Cl₂ solution of **HLBF₂**. Concentration is 0.02 $\mu\text{mol/L}$ to 20 $\mu\text{mol/L}$.

Table 4 Optical properties of 0.02-20 $\mu\text{mol/L}$ **HLBF₂** acetone solutions.

Conc. ($\mu\text{mol/L}$)	0.02	0.2	2	20
λ_{BF2} /nm	439	436.5	437	437
Φ	0.377	0.549	<0.99	<0.99
τ_1 /ns	2.3	2.2	2.3	2.3
A_1	0.215	0.289	0.281	0.366
χ^2	1.537	1.182	1.483	1.501

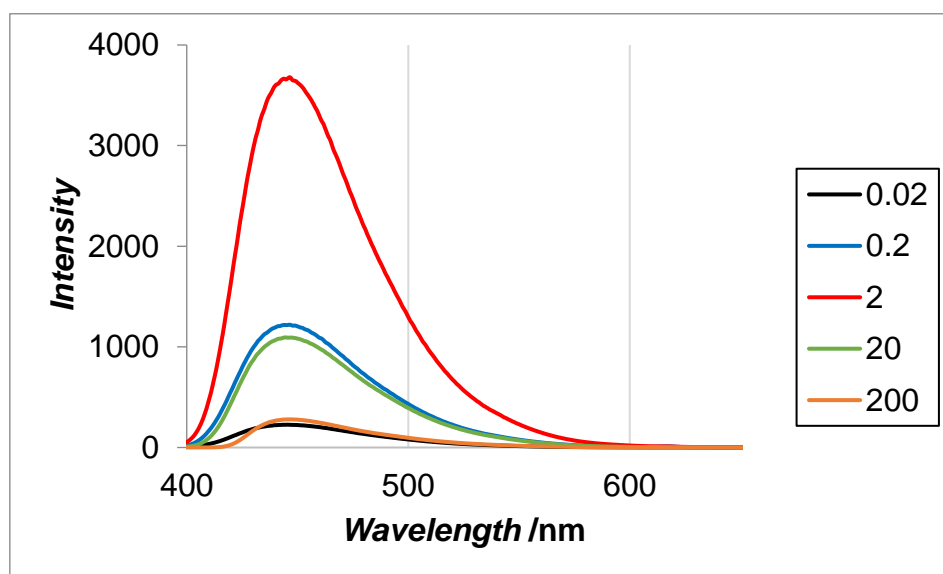


Fig. 16 PL spectra of acetone solution of **HLB F₂**. Concentration is 0.02 $\mu\text{mol/L}$ to 20 $\mu\text{mol/L}$.

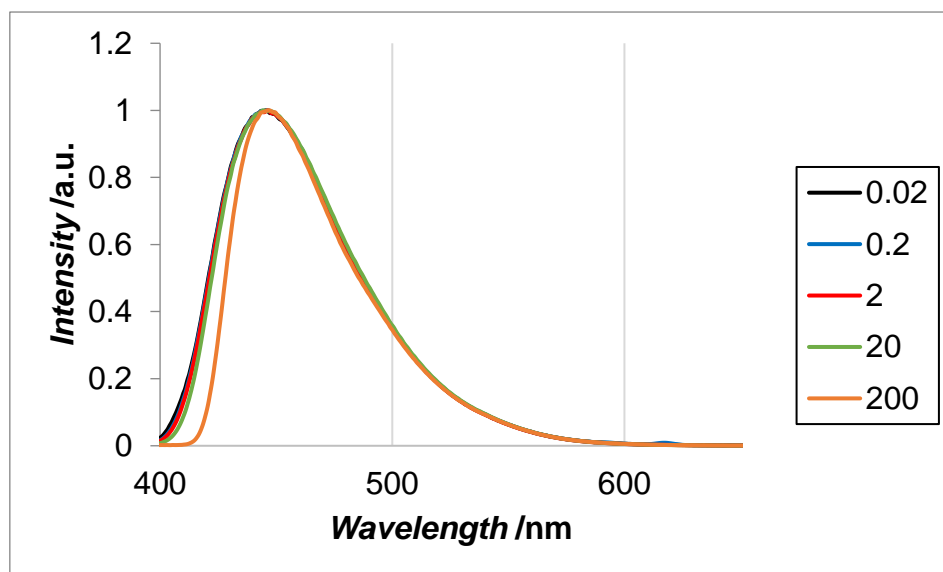


Fig. 17 Normalized PL spectra of acetone solution of **HLB F₂**. Concentration is 0.02 $\mu\text{mol/L}$ to 20 $\mu\text{mol/L}$.

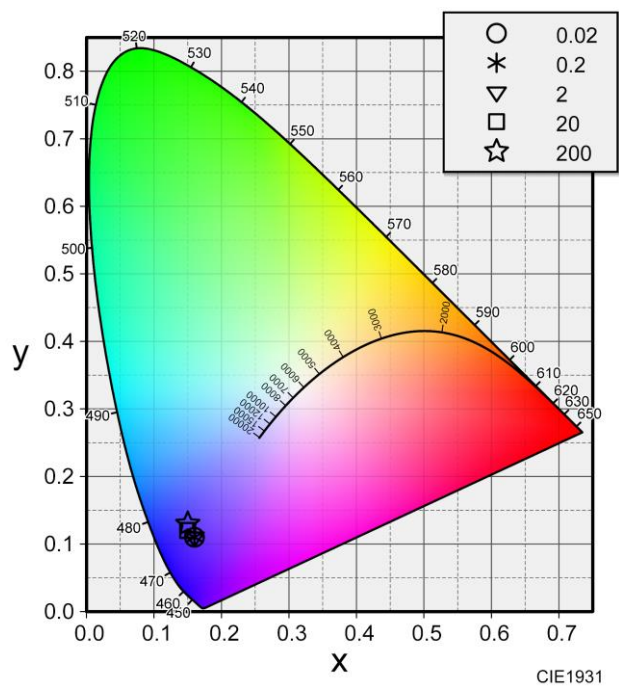


Fig. 18 Color diagram of acetone solution of **HLBF₂**. Concentration is 0.02 $\mu\text{mol/L}$ to 20 $\mu\text{mol/L}$.

Table 5 Optical properties of 0.02-200 $\mu\text{mol/L}$ **HLBF₂** acetone solutions.

Conc. ($\mu\text{mol/L}$)	0.02	0.2	2	20	200
λ_{BF_2} /nm	445.5	446	446.5	444.5	447
Φ	0.727	0.762	0.838	0.912	0.908
τ_1 /ns	2.3	2.3	2.4	2.5	2.9
A_1	0.284	0.282	0.207	0.386	0.266
χ^2	1.52	1.44	1.43	1.49	1.44

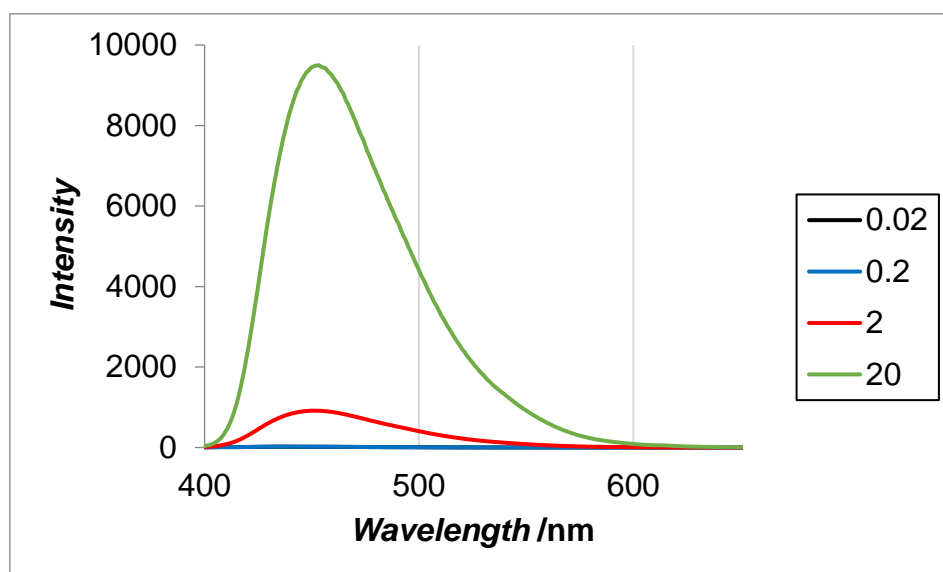


Fig. 19 PL spectra of MeCN solution of **HLBF₂**. Concentration is 0.02 $\mu\text{mol/L}$ to 20 $\mu\text{mol/L}$.

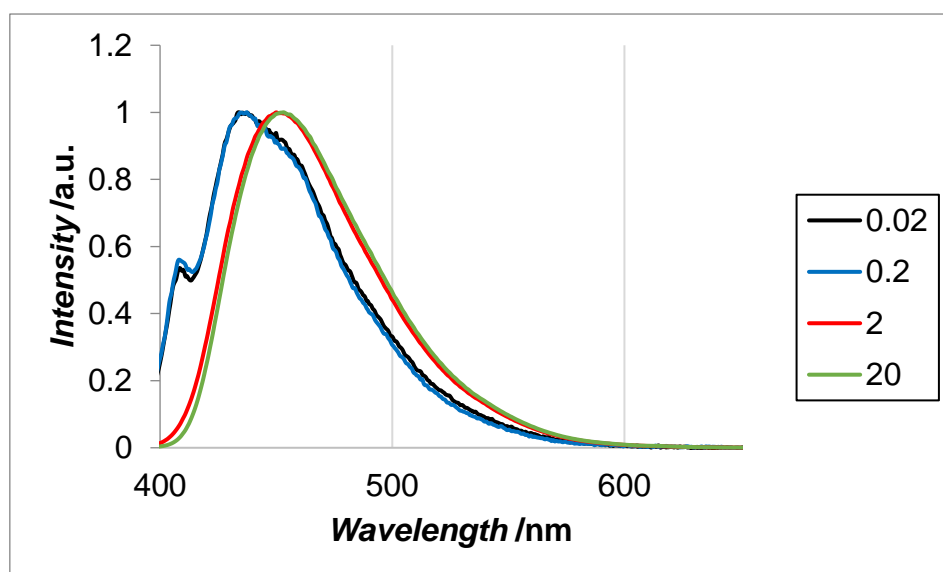


Fig. 20 Normalized PL spectra of MeCN solution of **HLBF₂**. Concentration is 0.02 $\mu\text{mol/L}$ to 20 $\mu\text{mol/L}$.

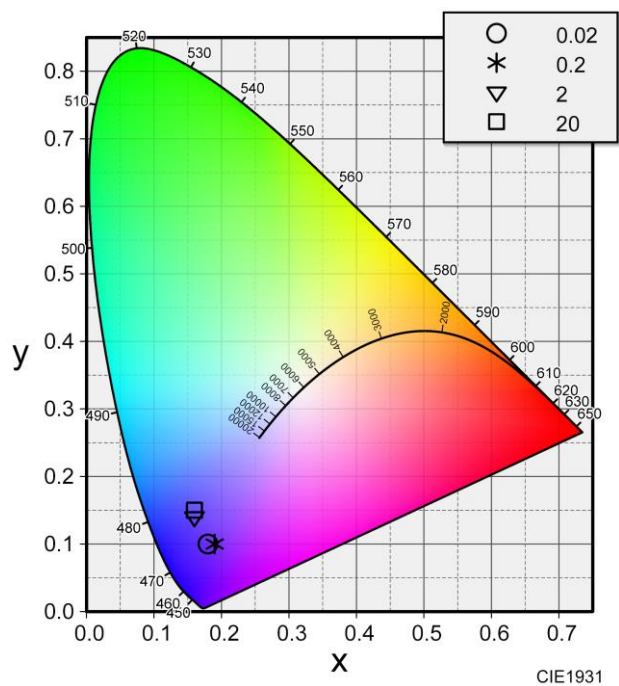


Fig. 21 Color diagram of MeCN solution of **HLBF₂**. Concentration is 0.02 $\mu\text{mol/L}$ to 20 $\mu\text{mol/L}$.

Table 6 Optical properties of 0.02-20 $\mu\text{mol/L}$ **HLBF₂** MeCN solutions.

Conc. ($\mu\text{mol/L}$)	0.02	0.2	2	20
λ_{BF_2} /nm	434	437.5	450	453
Φ	0.259	0.187	0.378	0.493
τ_1 /ns	1.5	1.5	1.4	1.4
τ_2 /ns	0.0	0.0	10.3	6.1
A_1	0.338	0.222	0.262	0.325
A_2	0.000	0.000	0.002	0.002
χ^2	1.606	1.650	1.322	1.299

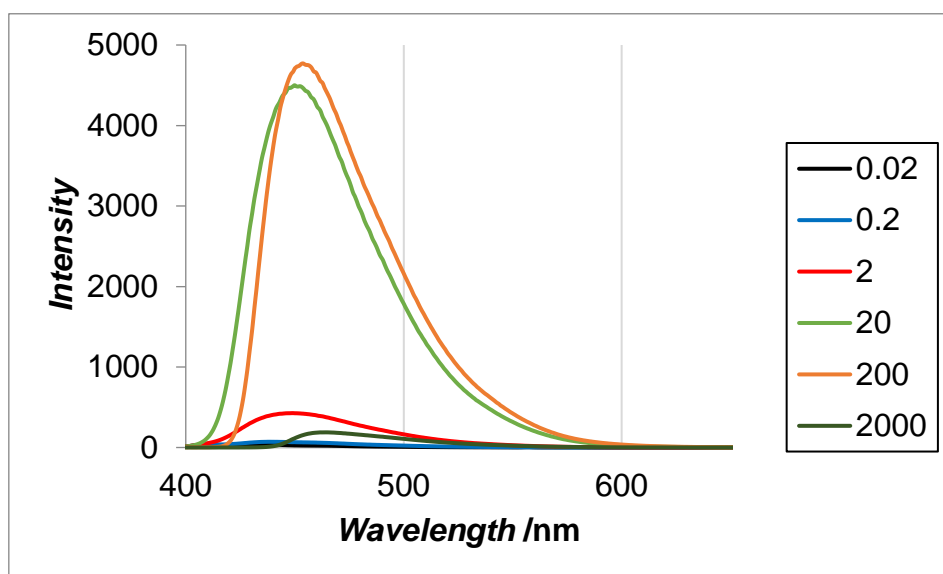


Fig. 22 PL spectra of DMF solution of **HLB F₂**. Concentration is 0.02 $\mu\text{mol/L}$ to 2000 $\mu\text{mol/L}$.

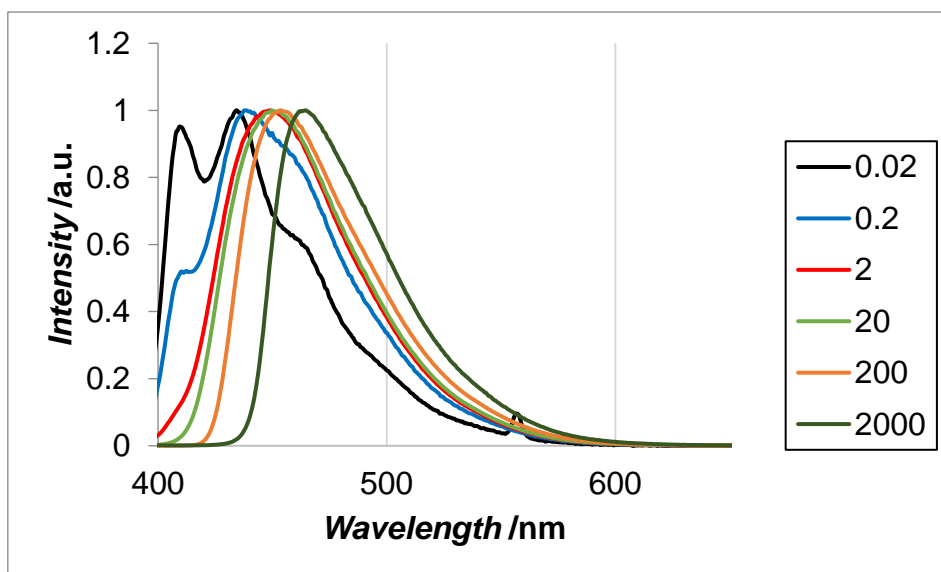


Fig. 23 Normalized PL spectra of DMF solution of **HLB F₂**. Concentration is 0.02 $\mu\text{mol/L}$ to 2000 $\mu\text{mol/L}$.

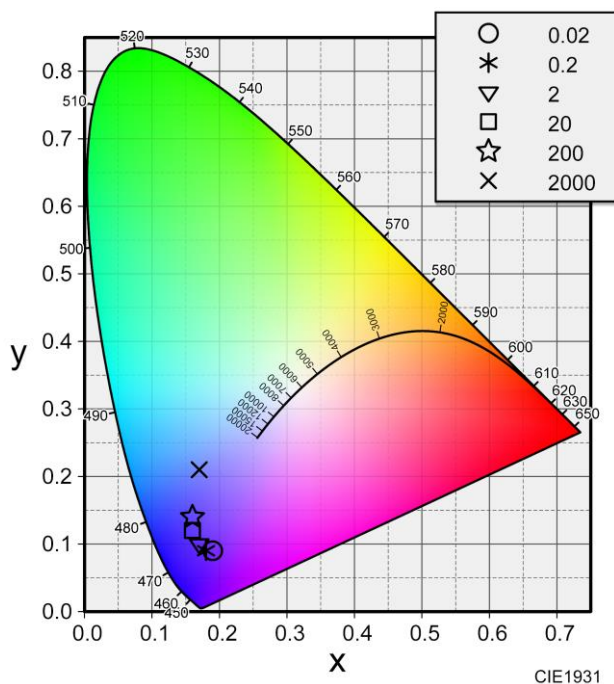


Fig. 24 Color diagram of DMF solution of **HLBF₂**. Concentration is 0.02 $\mu\text{mol/L}$ to 2000 $\mu\text{mol/L}$.

Table 7 Optical properties of 0.02-2000 $\mu\text{mol/L}$ **HLBF₂** DMF solutions.

Conc. ($\mu\text{mol/L}$)	0.02	0.2	2	20	200	2000
λ_{BF_2} /nm	434.5	438	449	450	453.5	464.5
Φ	0.046	0.086	0.108	0.198	0.225	0.077
τ_1 /ns	1.7	1.5	1.7	1.6	1.4	1.2
τ_2 /ns	0.0	0.0	0.0	0.0	18.9	13.3
A_1	0.148	0.258	0.194	0.221	0.327	0.278
A_2	0.000	0.000	0.000	0.000	0.002	0.007
χ^2	1.124	1.456	1.237	1.438	1.295	1.090

Solvent dependence about luminescence properties of Ln-LBF₂

Eu-LBF₂ also showed two emission bands below 500 nm and around 600 nm (Fig. 29). The former and the latter were attributed to the emission band of boron complex (Em^{B}) and Eu(III) ion (Em^{Eu}), respectively. In the solid state, **Eu-LBF₂** showed yellow emission with weak Em^{B} and strong Em^{Eu} . In the solution state, **Eu-LBF₂** showed solvent dependent luminescence properties with changing the intensification of

Em^{B} and Em^{Eu} . In acetone and DMF, **Eu-LBF₂** showed blue emission with stronger Em^{B} than Em^{Eu} . On the other hand, in dichloromethane and acetonitrile, **Eu-LBF₂** showed red emission with stronger Em^{Eu} than Em^{B} . All spectra were summarized in Fig. 27.

Emission properties of **Eu-LBF₂** in each solvent were summarized in Table 9. Low polarity solvent dichloromethane showed red emission, on the other hand, high polarity solvent acetone showed blue emission, which is opposite trend in the boron complex **HLBF₂**. The solvent dependent emission color is explained not by polarity but by coordination ability of solvent. Acetone and DMF have C=O site having high affinity to lanthanide ion. Because lanthanide complex has flexible coordination number (6~12), Eu(III) ion can accept more ligand in **Eu-LBF₂**. Furthermore, lanthanide ion is hard acid from HSAB theory, the hard basic solvents coordinate to Eu(III) in **Eu-LBF₂**. Finally, the coordination of solvent suppressed the intramolecular energy transfer efficiency from **LBF₂⁻** to Eu(III).

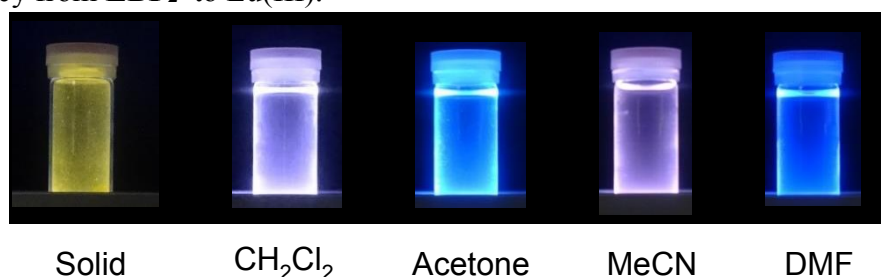


Fig. 25 Under UV irradiation of 200 $\mu\text{mol/L}$ solution of **Eu-LBF₂**.

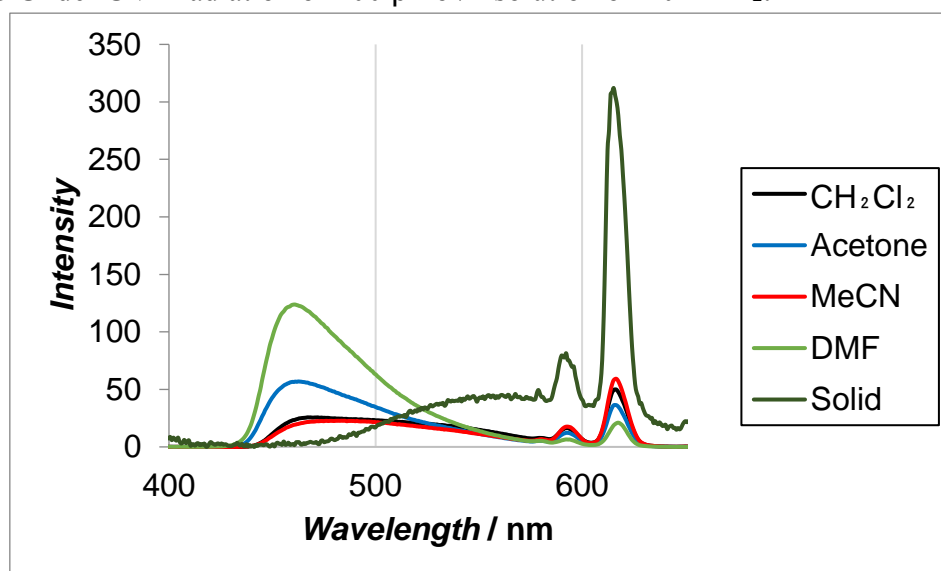


Fig. 26 PL spectra of **Eu-LBF₂** solution states (concentration is 200 $\mu\text{mol/L}$) and solid state.

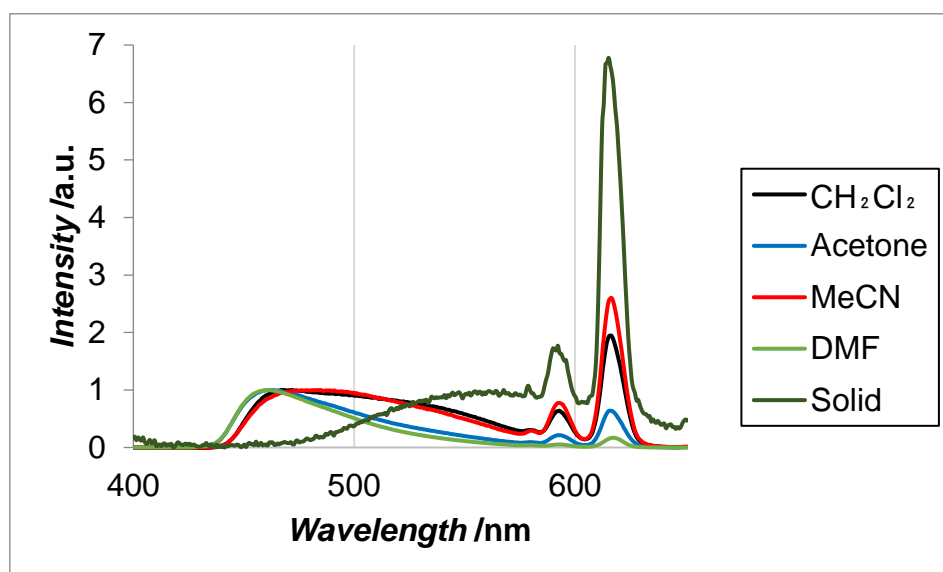


Fig. 27 Normalized PL spectra of **Eu-LBF₂** solution states (concentration is 200 $\mu\text{mol/L}$) and solid state.

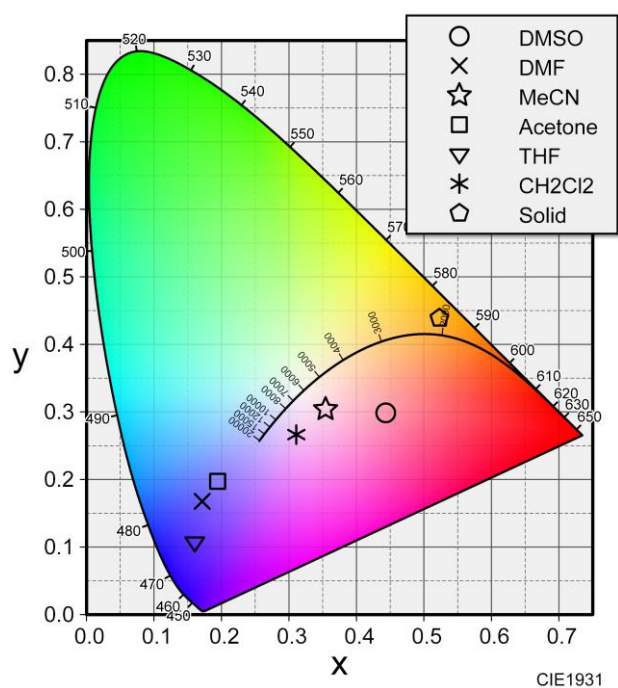


Fig. 28 Color diagram of **Eu-LBF₂** solution states (concentration is 200 $\mu\text{mol/L}$) and solid state.

Table 8 Optical properties of 200 $\mu\text{mol/L}$ **Eu-LBF₂** solutions.

	CH_2Cl_2	Acetone	MeCN	DMF	Solid
λ_{BF_2} /nm	472	462.5	483.5	461	578.9

λ_{Eu} /nm	616.5	615.5	616.5	617.5	615.5
$\text{Int}_{\text{Eu}}/\text{Int}_{\text{LBF}_2}$	1.945	0.640	2.603	0.170	6.800
Φ_{total}	0.301	0.379	0.412	0.301	0.071
Φ_{LBF_2}	0.099	0.206	0.094	0.245	0.020
Φ_{Eu}	0.193	0.164	0.30	0.052	0.051
τ_1 /ns	2.2	2.1	2.2	1.4	2.3
τ_2 /ns	9.7	6.8	9.2	12.0	10.0
A_1	0.271	0.388	0.211	0.460	0.252
A_2	0.099	0.009	0.044	0.003	0.055
χ^2	1.390	1.298	1.458	1.507	1.196

To clarify this mechanism of solvent dependent luminescence of **Eu-LBF₂**, photophysical properties of **Gd-LBF₂** was examined. Gd(III) ion has high energy gap between the ground state and the excited state (about 310 nm). Because of the energy gap, Gd(III) ion shows no emission in the region of visible light. However, Gd(III) complexes exhibit an internal heavy atom. Therefore, Gd(III) complex is available for understanding photophysical properties of lanthanide complex. PL spectra of **Gd-LBF₂** were shown in Figs. 32-34. **Gd-LBF₂** also showed solvent dependent luminescent properties. In the non-coordinating solvent; dichloromethane or acetonitrile, **Gd-LBF₂** showed green color. PL spectra showed new broad emission band around 525 nm in addition to Em^{B} . On the other hand, in the coordinating solvent; acetone or DMF, **Gd-LBF₂** showed blue color with Em^{B} similar to **HLBF₂**. Luminescent lifetime values in each solvent were summarized in Table. 10. The long lifetime emission species (~30 ns) was detected around 525 nm in dichloromethane or acetonitrile solution, which suggested that the emission peak around 525 nm originated from the phosphorescent of boron complex.

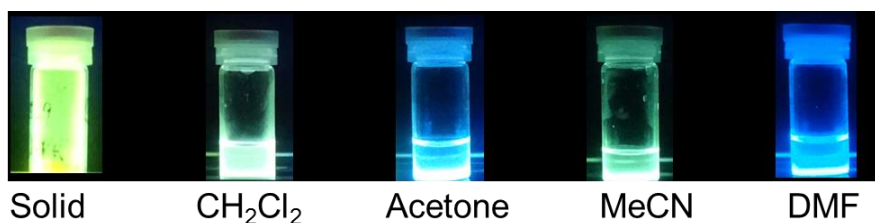


Fig. 29 Under UV irradiation of 200 $\mu\text{mol/L}$ solution of **Gd-LBF₂**.

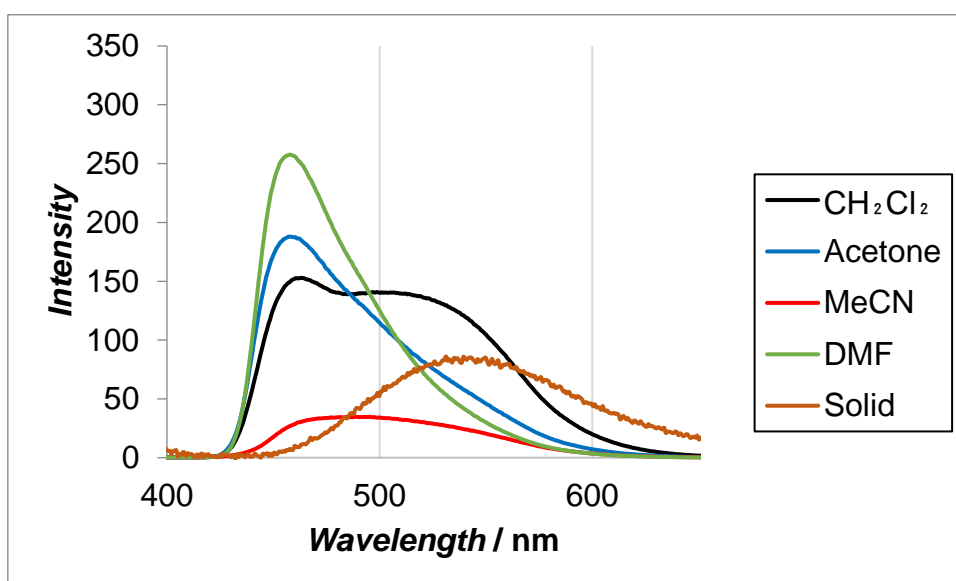


Fig. 30 PL spectra of **Gd-LBF₂** solution states (concentration is 200 $\mu\text{mol/L}$) and solid state.

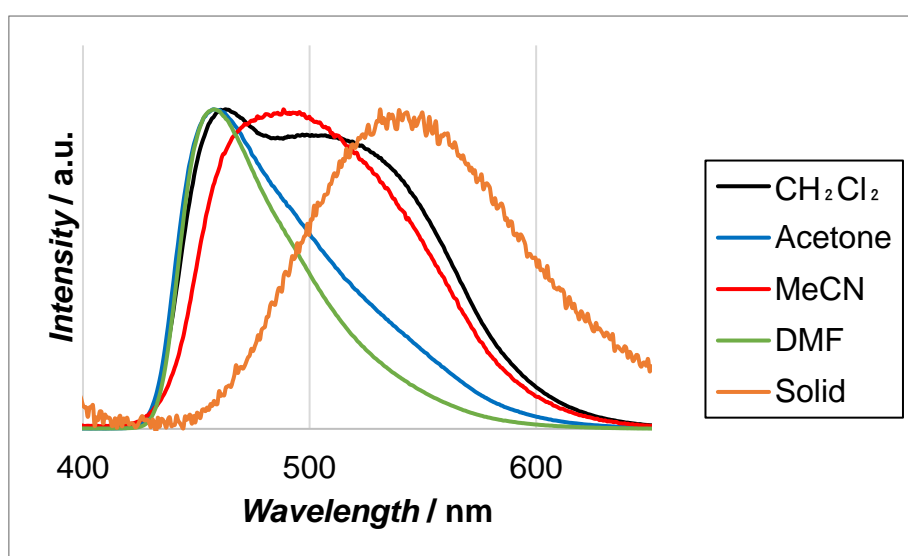


Fig. 31 Normalized PL spectra of **Gd-LBF₂** solution states (concentration is 200 $\mu\text{mol/L}$) and solid state.

Table 9 Optical properties of 200 $\mu\text{mol/L}$ **Gd-LBF₂** solutions.

Conc. ($\mu\text{mol/L}$)	CH_2Cl_2	Acetone	MeCN	DMF	Solid
λ_{BF_2} / nm	463	457.5	488.5	458	578.9
Φ	0.333	0.465	0.278	0.306	0.054
τ_1^{*1}	2.4	2.4	1.6	1.6	-
τ_2^{*1}	17.0	11.9	10.1	7.4	-

A_1^{*1}	0.285	0.205	0.192	0.184	-
A_2^{*1}	0.062	0.013	0.042	0.002	-
χ^{2*1}	1.10	1.064	1.15	1.48	-
τ_3^{*2}	4.3	3.34	8.1	1.6	-
τ_4^{*2}	24.9	20.88	26.1	11.1	-
A_3^{*2}	2.381	0.43449	0.294	0.398	-
A_4^{*2}	0.137	0.033765	0.073	0.004	-
χ^{2*2}	1.52	1.502527	1.62	1.32	-

*¹ Emission wavelength is 450 nm

*² Emission wavelength is 525 nm

From results of emission properties of **Eu-LBF₂** and **Gd-LBF₂**, mechanism of the color change in **Ln-LBF₂** was considered (Fig. 32). In non-coordinating solvent, **Ln-LBF₂** is excited and electrons go up to S_1 state by UV irradiation. Some electrons go back to ground state S_0 and show blue emission around 450 nm as fluorescent (Em^{BS1}). A part of electrons transfer to T_1 state via intersystem crossing (ISC) and show green emission around 525 nm as phosphorescent (Em^{BT1}). Although the $S_1 \rightarrow T_1$ transition is spin forbidden process, lanthanide ion relaxed the forbidden transition by internal heavy-atom effect. In **Eu-LBF₂**, a part of T_1 state electrons in boron complex transfer to T_1 state of Eu(III) ion as intra-molecular energy transfer. Then, red emission of Eu(III), Em^{Eu} , around 600 nm is observed. This is a proposed emission mechanism of **Ln-LBF₂** in non-coordinating solvent. In the case of coordinating solvent, the additional coordination to lanthanide ion weakens the interaction among lanthanide ion and other ligands which means weakens the internal heavy atom effect and the $S_1 \rightarrow T_1$ process in the boron complex is suppressed. As a result, **Eu-LBF₂** shows strong fluorescent from S_1 state of boron (Em^{BS1}), and weak Em^{Eu} with the suppressed energy transfer from boron complex to Eu(III) ion.

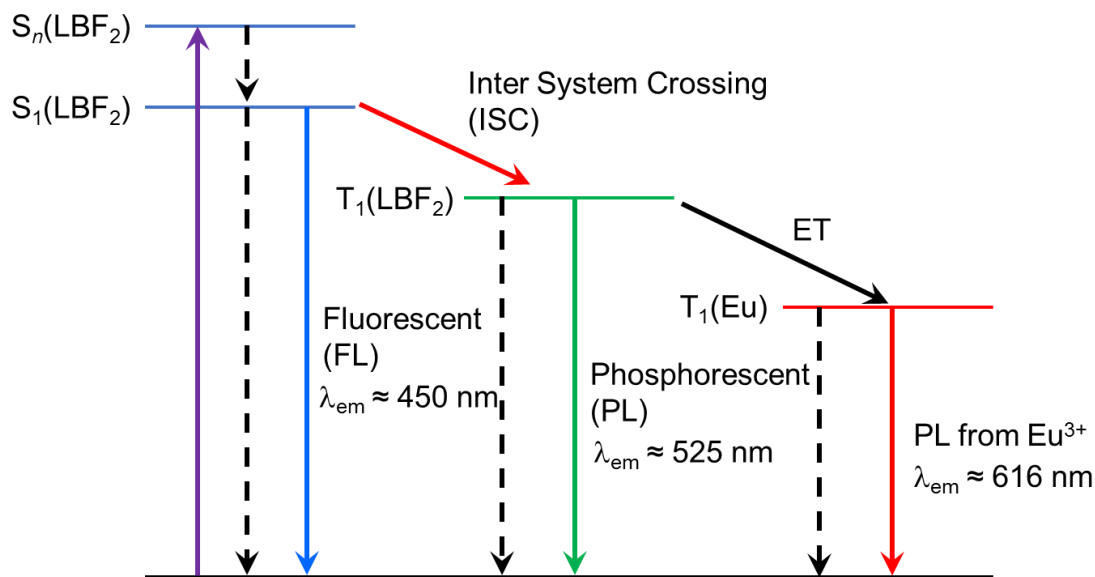


Fig. 32 Energy Diagram of **Eu-LBF₂**

Concentration dependence of **Eu-LBF₂**

In 200 $\mu\text{mol/L}$ dichloromethane and acetonitrile solution, **Eu-LBF₂** showed red emission. On the other hand, in their diluted solution, **Eu-LBF₂** showed blue emission. Fig. 34 shows normalized PL spectra of dichloromethane solution in difference concentration. In the dilute solution lower than 2 $\mu\text{mol/L}$, major emission band was Em^{BSI} . On the other hand, in the concentrated solution higher than 20 $\mu\text{mol/L}$, major emission band changed to Em^{Eu} . Furthermore, the concentration gets higher, the emission peak top of boron complex shifted to longer wavelength.

Change of emission intensity ratio of $\text{Em}^{\text{Eu}}/\text{Em}^{\text{B}}$ was also measured using other solvents (Tables. 11-14). Except for DMF solution, all solution exhibited similar trend. Only DMF solution showed blue emission in all concentration range from 2 $\mu\text{mol/L}$ to 2000 mmol/L. These color changes suggest that intermolecular energy transfer from **LBF₂** to Eu(III) ion.

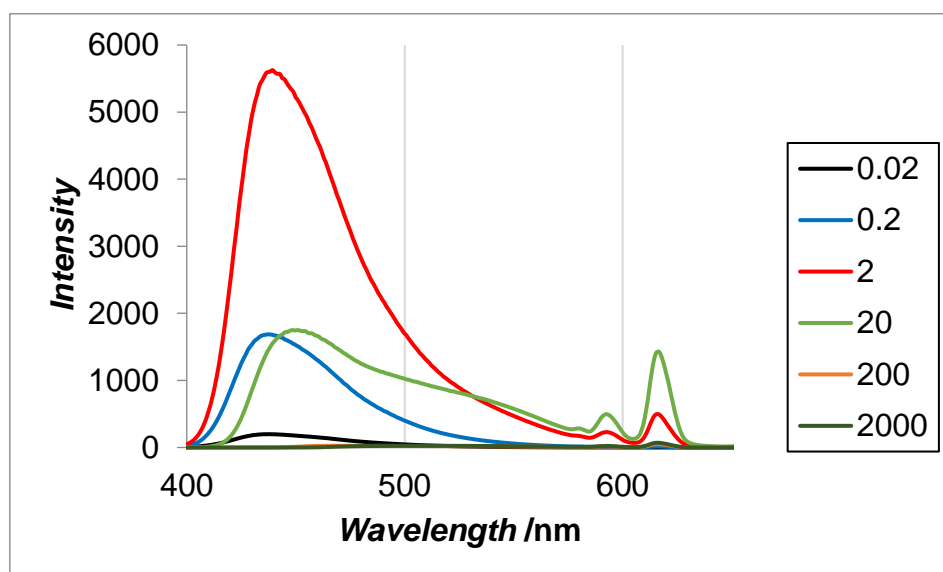


Fig. 33 PL spectra of CH_2Cl_2 solution of **Eu-LBF₂**. Concentration is 0.02 $\mu\text{mol/L}$ to 2000 $\mu\text{mol/L}$.

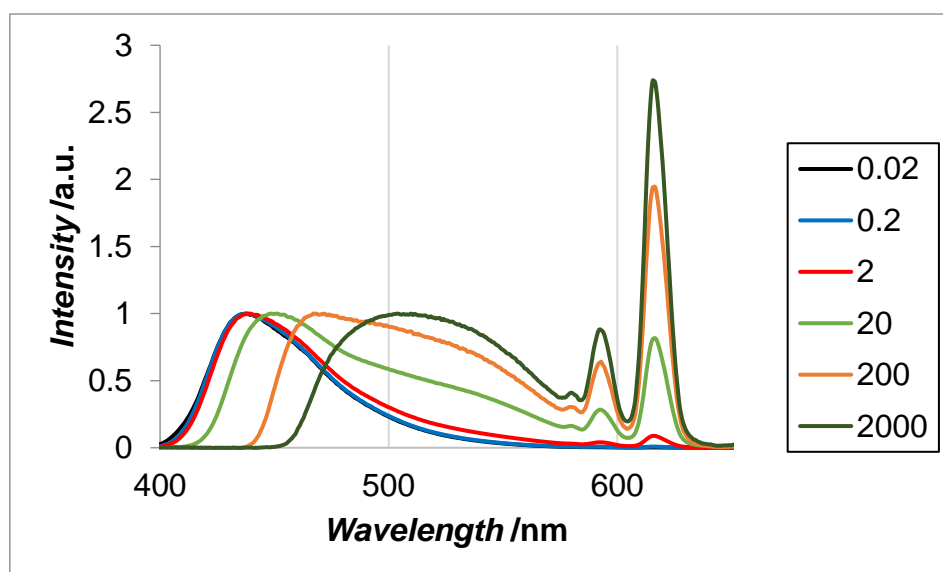


Fig. 34 Normalized PL spectra of CH_2Cl_2 solution of **Eu-LBF₂**. Concentration is 0.02 $\mu\text{mol/L}$ to 2000 $\mu\text{mol/L}$.

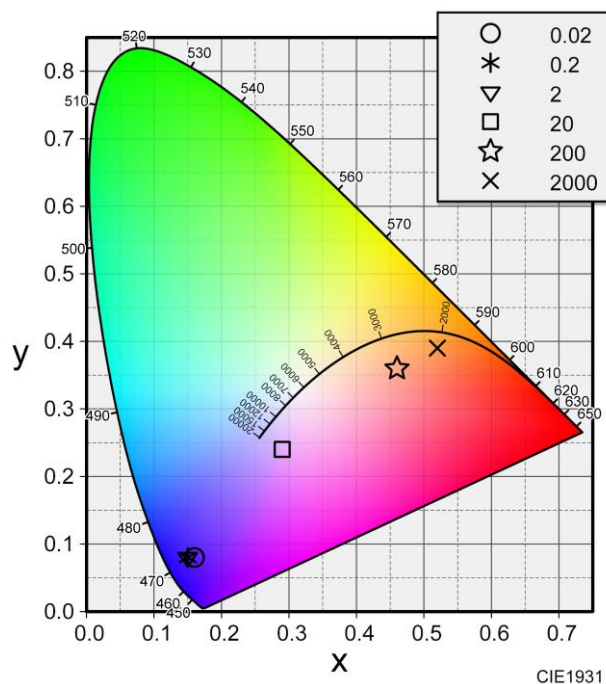


Fig. 35 Color diagram of CH_2Cl_2 solution of **Eu-LBF₂**. Concentration is 0.02 $\mu\text{mol/L}$ to 2000 $\mu\text{mol/L}$.

Table 10 Optical properties of 0.02-2000 $\mu\text{mol/L}$ **Eu-LBF₂** CH_2Cl_2 solutions.

Conc. ($\mu\text{mol/L}$)	0.02	0.2	2	20	200	2000
λ_{BF_2} /nm	437.5	437.5	439.5	448.5	472	504
λ_{Eu} /nm	614.5	616	616	616.5	616.5	615.5
$\text{Int}_{\text{Eu}}/\text{Int}_{\text{LBF}_2}$	0.003	0.009	0.088	0.818	1.945	2.738
Φ_{total}	0.879	1.011	0.820	0.409	0.301	0.317
Φ_{LBF_2}	0.860	0.993	0.804	0.243	0.099	0.075
Φ_{Eu}	0.017	0.015	0.014	0.159	0.193	0.231
τ_1 /ns	2.4	2.5	2.4	2.6	2.2	2.4
τ_2 /ns	0.0	11.1	4.1	9.9	9.7	0.0
A_1	0.395	0.402	1.620	0.193	0.271	0.308
A_2	0.000	0.011	0.037	0.068	0.099	0.000
χ^2	1.440	1.180	1.586	1.337	1.390	1.273

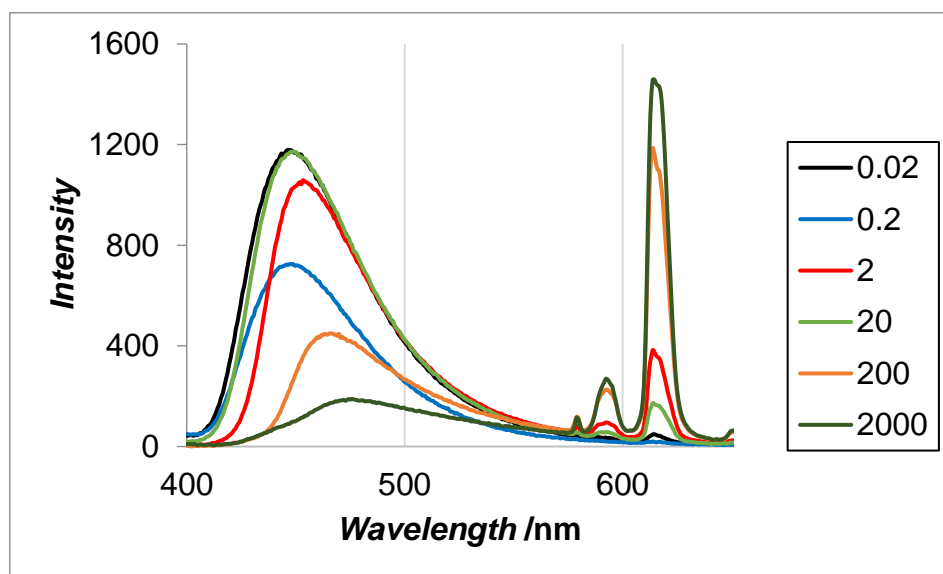


Fig. 36 PL spectra of acetone solution of **Eu-LBF₂**. Concentration is 0.02 $\mu\text{mol/L}$ to 2000 $\mu\text{mol/L}$.

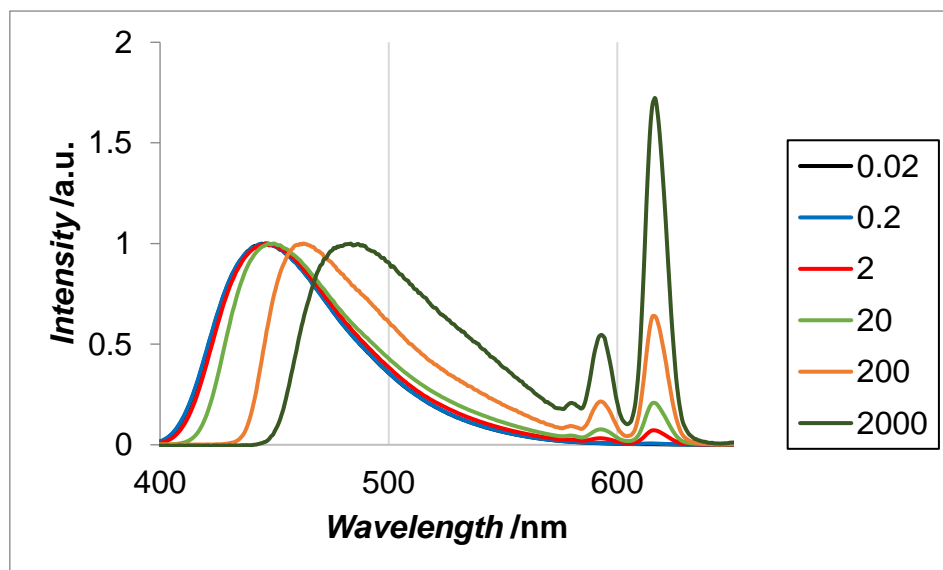


Fig. 37 Normalized PL spectra of acetone solution of **Eu-LBF₂**. Concentration is 0.02 $\mu\text{mol/L}$ to 2000 $\mu\text{mol/L}$.

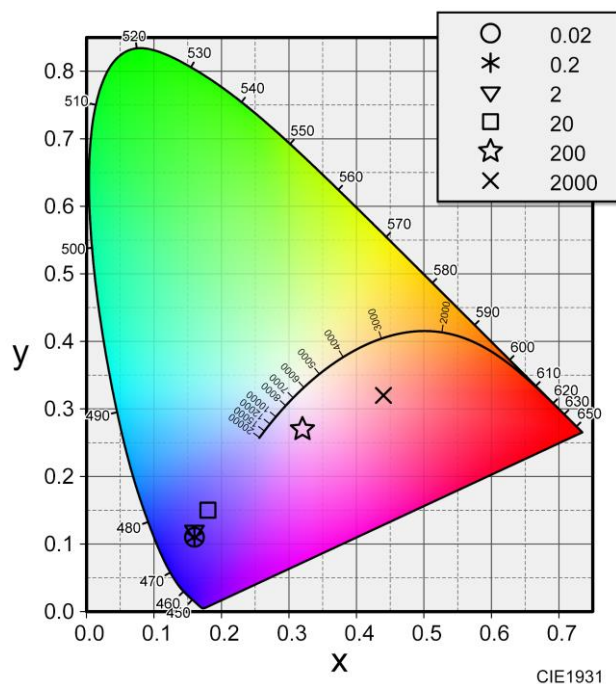


Fig. 38 Color diagram of acetone solution of **Eu-LBF₂**. Concentration is 0.02 $\mu\text{mol/L}$ to 2000 $\mu\text{mol/L}$.

Table 11 Optical properties of 0.02-2000 $\mu\text{mol/L}$ **Eu-LBF₂** acetone solutions.

Conc. ($\mu\text{mol/L}$)	0.02	0.2	2	20	200	2000
λ_{BF_2} /nm	447	446	446	449.5	462.5	483.5
λ_{Eu} /nm	605	614.5	615.5	616	615.5	616.5
$\text{Int}_{\text{Eu}}/\text{Int}_{\text{LBF}_2}$	0.004	0.007	0.072	0.208	0.640	1.723
Φ_{total}	0.934	0.912	0.671	0.512	0.379	0.348
Φ_{LBF_2}	0.901	0.888	0.627	0.443	0.206	0.113
Φ_{Eu}	0.030	0.021	0.040	0.063	0.164	0.224
τ_1 /ns	2.4	2.4	2.6	2.5	2.1	1.4
τ_2 /ns	0.0	0.0	0.0	5.2	6.8	4.0
A_1	0.286	0.307	0.334	1.344	0.388	0.539
A_2	0.000	0.000	0.000	0.018	0.009	0.010
χ^2	1.564	1.548	1.540	1.131	1.298	1.183

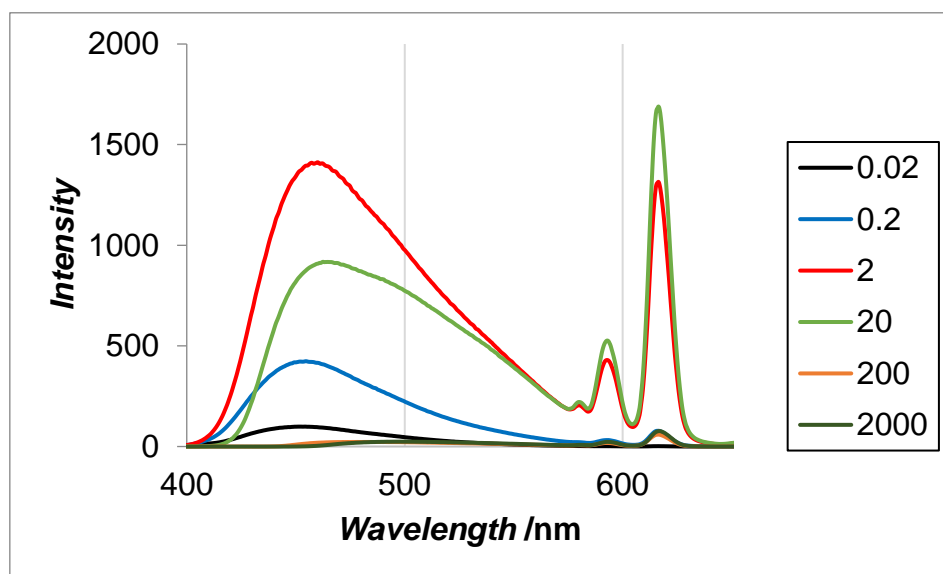


Fig. 39 PL spectra of MeCN solution of **Eu-LBF₂**. Concentration is 0.02 $\mu\text{mol/L}$ to 2000 $\mu\text{mol/L}$.

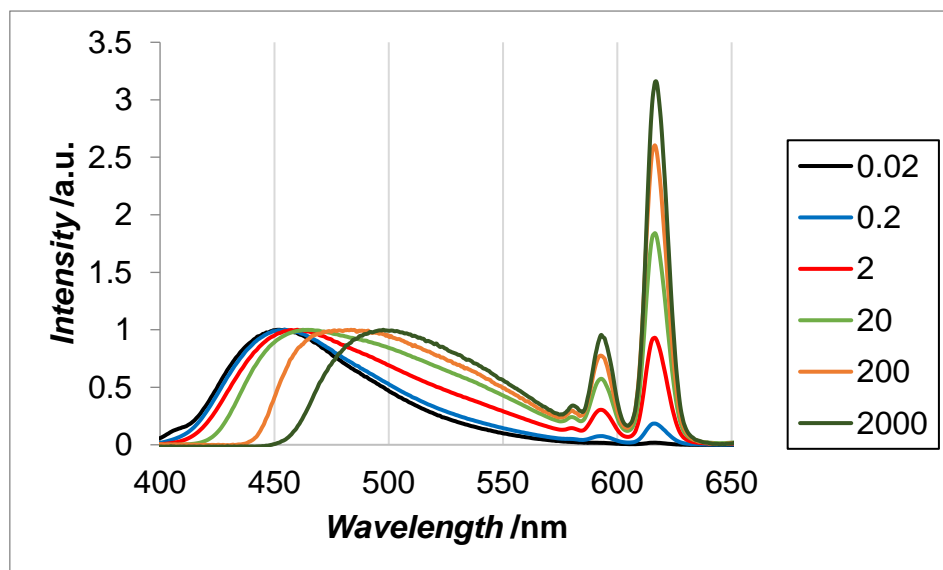


Fig. 40 Normalized PL spectra of MeCN solution of **Eu-LBF₂**. Concentration is 0.02 $\mu\text{mol/L}$ to 2000 $\mu\text{mol/L}$.

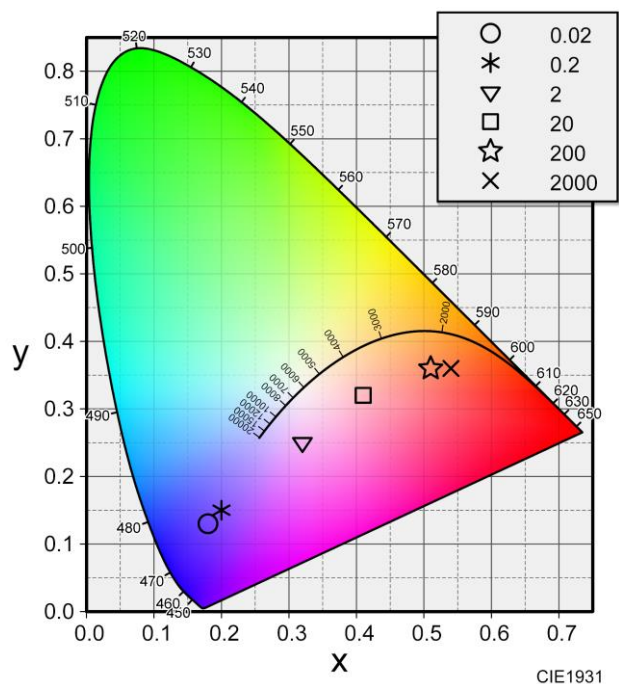


Fig. 41 Color diagram of MeCN solution of **Eu-LBF₂**. Concentration is 0.02 $\mu\text{mol/L}$ to 2000 $\mu\text{mol/L}$.

Table 12 Optical properties of 0.02-2000 $\mu\text{mol/L}$ **Eu-LBF₂** MeCN solutions.

Conc. ($\mu\text{mol/L}$)	0.02	0.2	2	20	200	2000
λ_{BF_2} /nm	454.5	454.5	460	462.5	483.5	497.5
λ_{Eu} /nm	616.5	616.5	616.5	616.5	616.5	617
$\text{Int}_{\text{Eu}}/\text{Int}_{\text{LBF}_2}$	0.018	0.185	0.931	1.840	2.603	3.160
Φ_{total}	0.415	0.359	0.360	0.325	0.412	0.440
Φ_{LBF_2}	0.395	0.299	0.191	0.122	0.094	0.081
Φ_{Eu}	0.02	0.06	0.16	0.19	0.30	0.34
τ_1 /ns	1.5	1.7	2.0	2.1	2.2	0.9
τ_2 /ns	7.8	9.4	9.0	8.3	9.2	2.6
A_1	0.347	0.361	0.224	0.339	0.211	17.516
A_2	0.006	0.010	0.022	0.041	0.044	1.115
χ^2	1.147	1.560	1.513	1.390	1.458	1.688

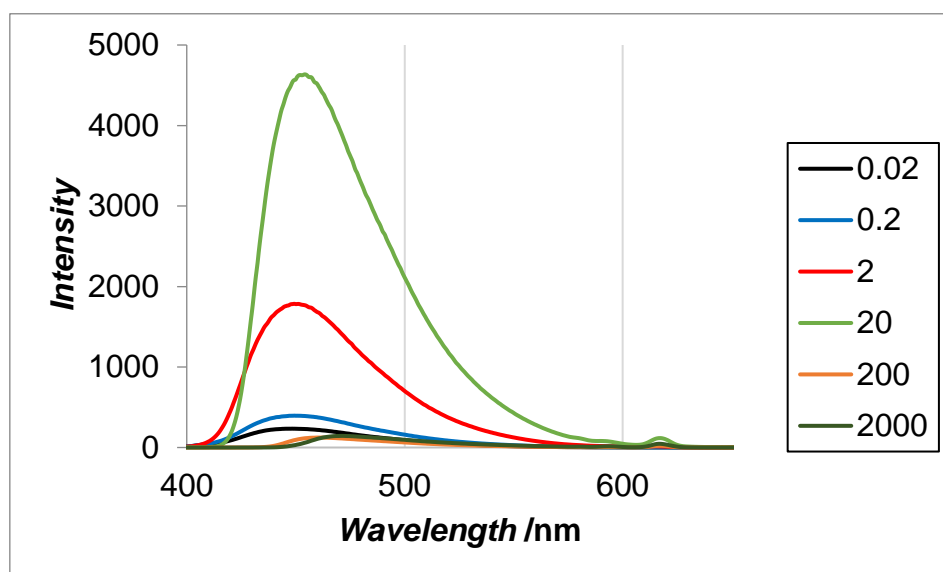


Fig. 42 PL spectra of DMF solution of **Eu-LBF₂**. Concentration is 0.02 $\mu\text{mol/L}$ to 2000 $\mu\text{mol/L}$.

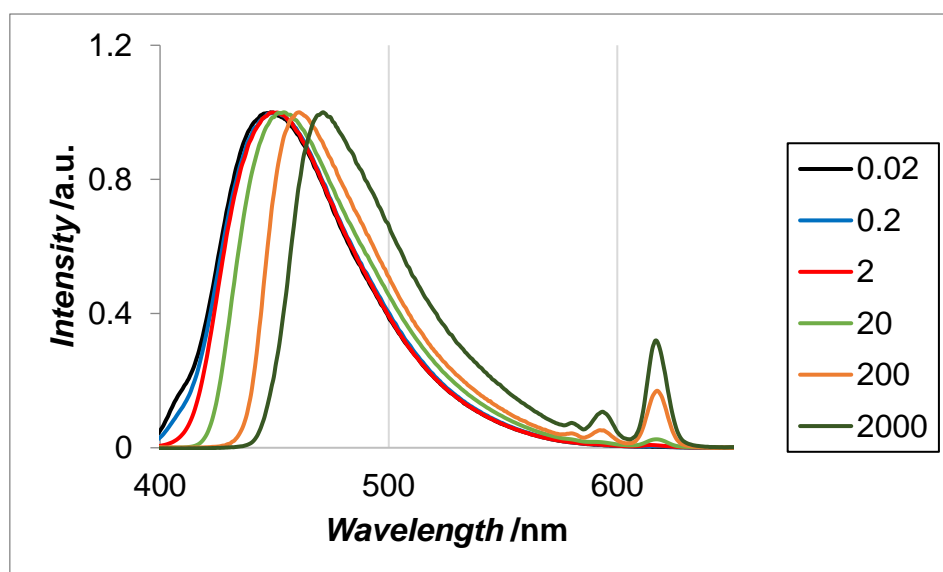


Fig. 43 Normalized PL spectra of DMF solution of **Eu-LBF₂**. Concentration is 0.02 $\mu\text{mol/L}$ to 2000 $\mu\text{mol/L}$.

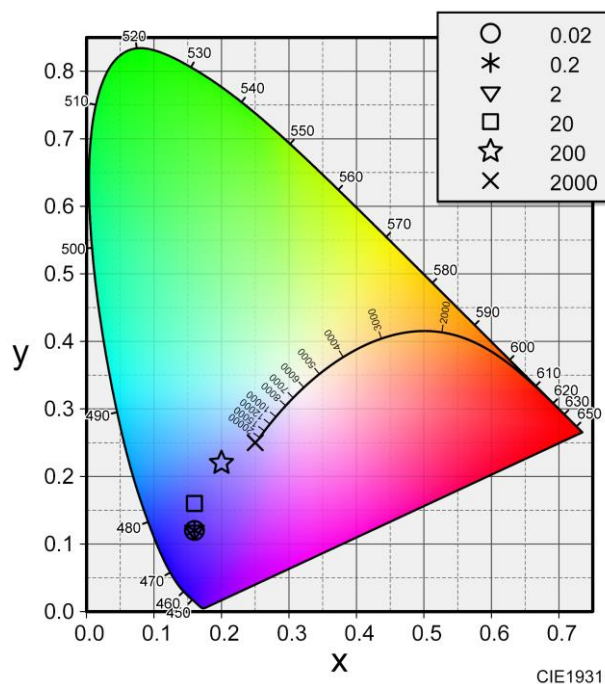


Fig. 44 Color diagram of DMF solution of **Eu-LBF₂**. Concentration is 0.02 $\mu\text{mol/L}$ to 2000 $\mu\text{mol/L}$.

Table 13 Optical properties of 0.02-2000 $\mu\text{mol/L}$ **Eu-LBF₂** DMF solutions.

Conc. ($\mu\text{mol/L}$)	0.02	0.2	2	20	200	2000
λ_{BF_2} /nm	448.5	449.5	449.5	454	461	471.5
λ_{Eu} /nm	605	615	614.5	617	617.5	617
$\text{Int}_{\text{Eu}}/\text{Int}_{\text{LBF}_2}$	0.004	0.005	0.008	0.025	0.170	0.320
Φ_{total}	0.216	0.207	0.138	0.294	0.301	0.280
Φ_{LBF_2}	0.209	0.200	0.132	0.277	0.245	0.193
Φ_{Eu}	0.007	0.007	0.005	0.016	0.052	0.082
τ_1 /ns	1.4	1.0	1.4	1.3	1.4	0.2
τ_2 /ns	6.4	5.0	7.5	4.0	12.0	4.6
A_1	0.344	0.652	0.316	6.931	0.460	0.905
A_2	0.006	0.012	0.003	0.039	0.003	0.004
χ^2	0.908	1.596	1.292	0.996	1.507	1.642

Concentration dependence of photophysical properties of **Gd-LBF₂** was also measured. Fig. 46 showed normalized PL spectra of dichloromethane solution in difference concentration. In the the diluted solution lower than 2 $\mu\text{mol/L}$, the fluorescent band Em^{BS1} was obserbed around 450 nm. On the other hand, in the concentrated solution higher than 20 $\mu\text{mol/L}$, the emission band shifted to longer wavelength. Finally, the shift reached over 80 nm. The shifted band is attributed to phosphorescent of boron complex, Em^{BT1} . Especially, in the high concentration, the emission intensity ratio of phosphorescent shows stronger than that of florescent (Fig. 51).

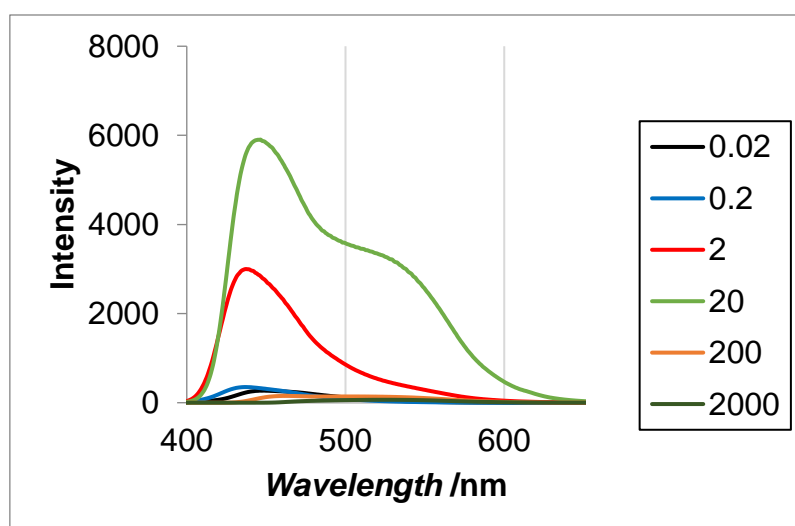


Fig. 45 PL spectra of CH_2Cl_2 solution of **Gd-LBF₂**. Concentration is 0.02 $\mu\text{mol/L}$ to 2000 $\mu\text{mol/L}$.

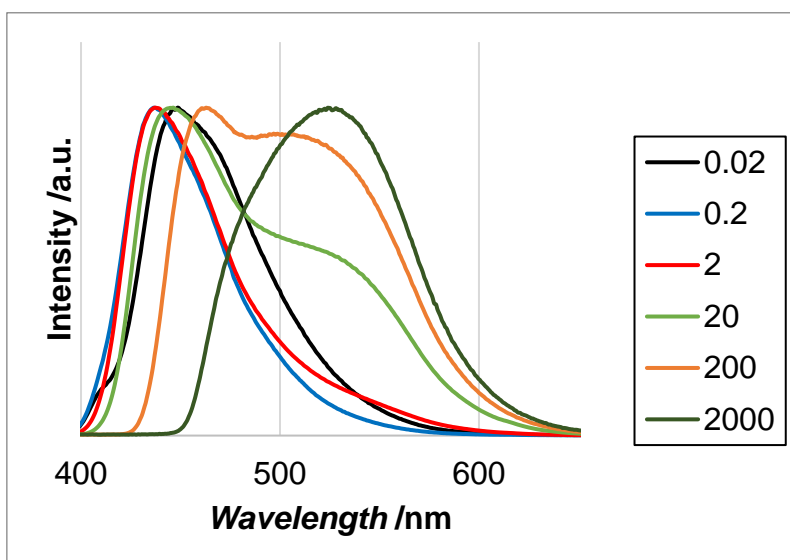


Fig. 46 Normalized PL spectra of CH₂Cl₂ solution of **Gd-LBF₂**. Concentration is 0.02 μmol/L to 2000 μmol/L.

Table 14 Optical properties of 0.02-2000 μmol/L **Gd-LBF₂** CH₂Cl₂ solutions.

Conc. (μmol/L)	0.02	0.2	2	20	200	2000
λ_{BF_2} /nm	448.5	436.5	437.5	446.5	463	524
Φ	0.352	0.279	0.759	0.519	0.333	0.254
τ_1^{*1}	2.9	2.2	2.3	2.2	2.4	2.0
τ_2^{*1}	0	0	0	16.1	17.0	10.1
A_1^{*1}	0.206	0.318	0.199	0.243	0.285	0.234
A_2^{*1}	0	0	0	0.034	0.062	0.044
χ^{2*1}	1.03	1.46	1.54	1.18	1.10	1.52
τ_3^{*2}	3.7	2.4	2.4	3.4	4.3	7.6
τ_4^{*2}	0	23.2	23.7	29.4	24.9	31.5
A_3^{*2}	0.253	2.134	0.342	3.722	2.381	0.523
A_4^{*2}	0	0.002	0.006	0.072	0.137	0.106
χ^{2*2}	1.28	1.23	1.02	1.46	1.52	1.49
x	0.18	0.18	0.16	0.21	0.31	0.32
y	0.09	0.08	0.09	0.22	0.44	0.48

^{*1} Emission wavelength is 450 nm

^{*2} Emission wavelength is 525 nm

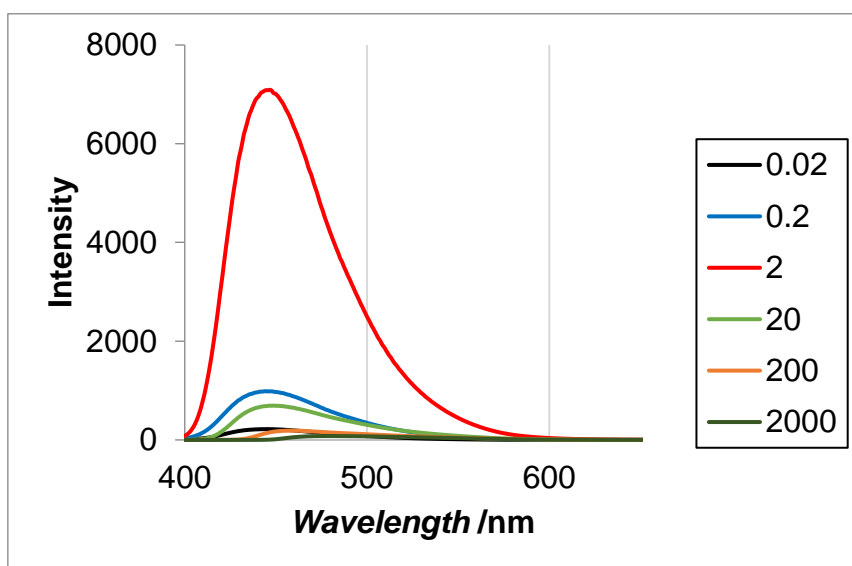


Fig. 47 PL spectra of Acetone solution of Gd-LBF_2 . Concentration is 0.02 $\mu\text{mol/L}$ to 2000 $\mu\text{mol/L}$.

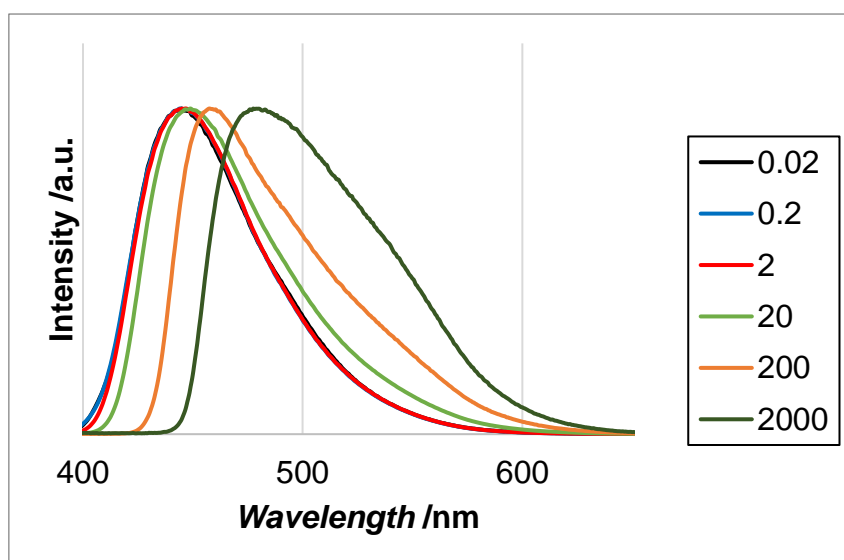


Fig. 48 Normalized PL spectra of Acetone solution of Gd-LBF_2 . Concentration is 0.02 $\mu\text{mol/L}$ to 2000 $\mu\text{mol/L}$.

Table 15 Optical properties of 0.02-2000 $\mu\text{mol/L}$ **Gd-LBF₂** Acetone solutions.

Conc. ($\mu\text{mol/L}$)	0.02	0.2	2	20	200	2000
λ_{BF_2} /nm	445	444.5	446.5	449	457.5	477.5
Φ	<0.99	<0.99	<0.99	0.711	0.465	0.289
τ_1^{*1}	2.3	2.4	2.3	2.0	2.4	2.1
τ_2^{*1}	0	0	0	4.2	11.9	10.3
A_1^{*1}	0.255	0.168	0.223	0.159	0.205	0.234
A_2^{*1}	0	0	0	0.041	0.013	0.033
χ^{2*1}	1.09	1.19	1.59	1.34	1.06	1.36
τ_3^{*2}	2.4	2.5	2.4	2.6	3.3	8.0
τ_4^{*2}	0.0	16.8	0	13.5	20.9	29.4
A_3^{*2}	0.267	1.541	0.295	0.249	0.434	0.706
A_4^{*2}	0	0.009	0	0.016	0.034	0.058
χ^{2*2}	1.25	1.29	1.11	1.01	1.50	2.00
x	0.16	0.16	0.16	0.16	0.18	0.24
y	0.11	0.11	0.11	0.14	0.22	0.36

^{*1} Emission wavelength is 450 nm

^{*2} Emission wavelength is 525 nm

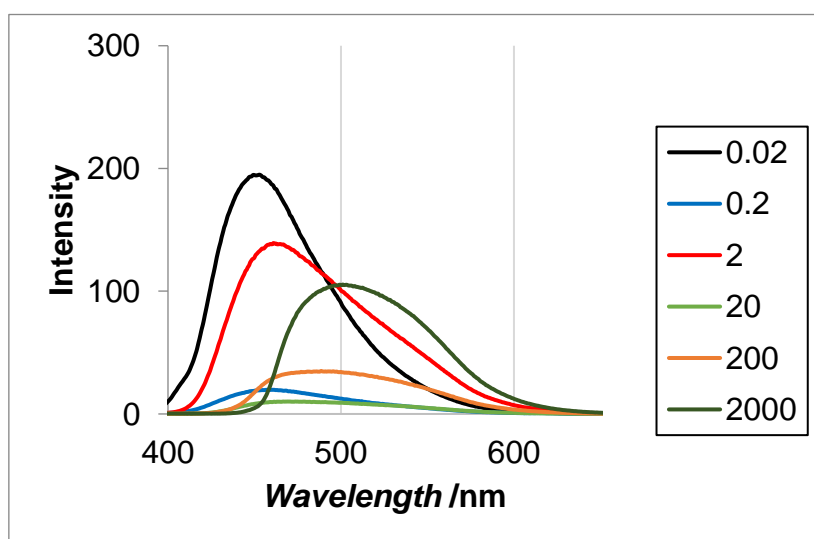


Fig. 49 PL spectra of MeCN solution of **Gd-LBF₂**. Concentration is 0.02 $\mu\text{mol/L}$ to 2000 $\mu\text{mol/L}$.

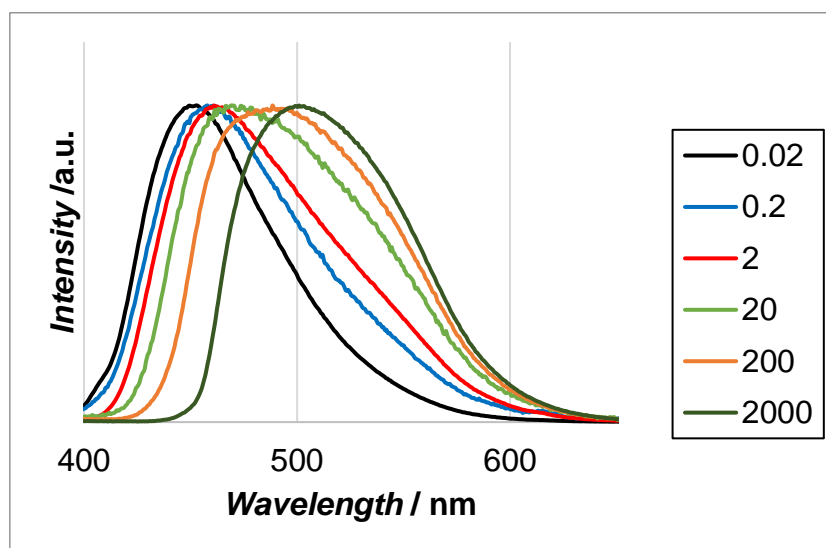


Fig. 50 Normalized PL spectra of MeCN solution of **Gd-LBF₂**. Concentration is 0.02 $\mu\text{mol/L}$ to 2000 $\mu\text{mol/L}$.

Table 16 Optical properties of 0.02-2000 $\mu\text{mol/L}$ **Gd-LBF₂** MeCN solutions.

Conc. ($\mu\text{mol/L}$)	0.02	0.2	2	20	200	2000
λ_{BF_2} /nm	453	458	461	469	488.5	501
Φ	0.307	0.330	0.396	0.263	0.278	0.270
τ_1^{*1}	1.5	1.7	1.4	1.5	1.6	1.6
τ_2^{*1}	0	0	7.9	9.8	10.1	10.6
A_1^{*1}	0.204	0.204	0.232	0.168	0.192	0.219
A_2^{*1}	0	0	0.009	0.024	0.042	0.064
χ^{2*1}	1.47	1.78	1.05	1.13	1.15	1.25
τ_3^{*2}	1.8	1.6	1.8	2.1	8.1	8.4
τ_4^{*2}	12.5	13.6	13.8	12.0	26.1	28.2
A_3^{*2}	0.212	0.289	0.234	18.864	0.294	0.320
A_4^{*2}	0.012	0.003	0.013	0.179	0.073	0.083
χ^{2*2}	1.56	1.32	1.28	1.48	1.62	1.38
x	0.18	0.18	0.18	0.22	0.26	0.29
y	0.15	0.15	0.18	0.28	0.37	0.45

^{*1} Emission wavelength is 450 nm

^{*2} Emission wavelength is 525 nm

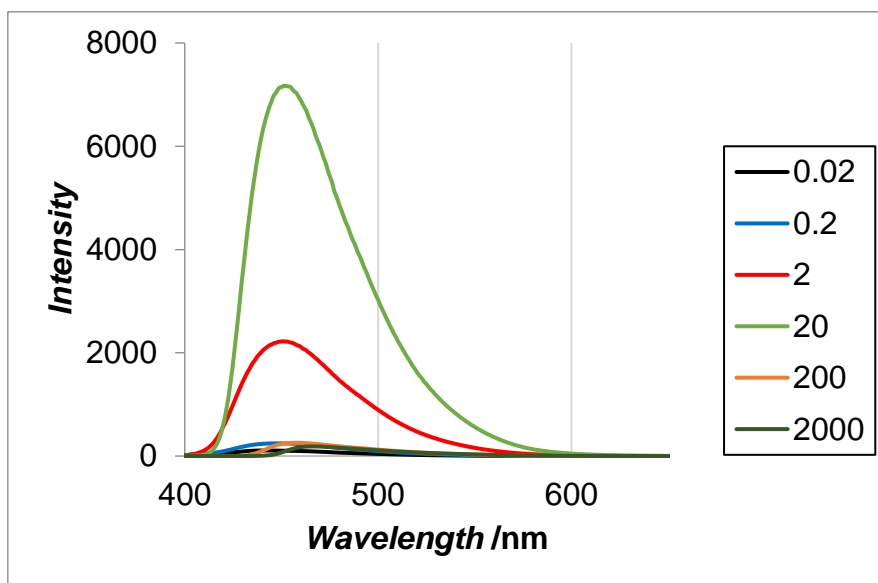


Fig. 51 PL spectra of DMF solution of **Gd-LBF₂**. Concentration is 0.02 $\mu\text{mol/L}$ to 2000 $\mu\text{mol/L}$.

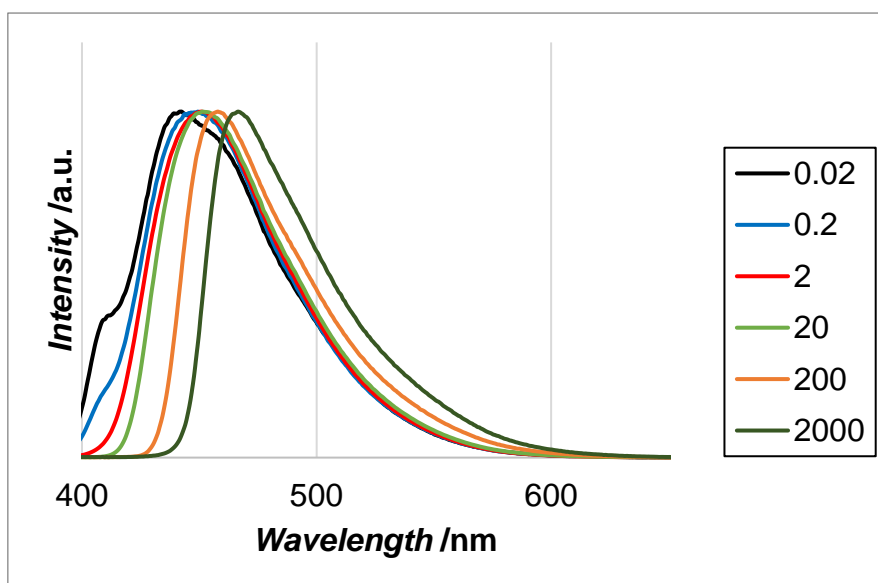


Fig. 52 Normalized PL spectra of DMF solution of **Gd-LBF₂**. Concentration is 0.02 $\mu\text{mol/L}$ to 2000 $\mu\text{mol/L}$.

Table 17 Optical properties of 0.02-2000 $\mu\text{mol/L}$ **Gd-LBF₂** DMF solutions.

Conc. ($\mu\text{mol/L}$)	0.02	0.2	2	20	200	2000
λ_{BF2} /nm	442.5	449.5	451	451.5	458	466.5
Φ	0.216	0.184	0.264	0.292	0.306	0.245

τ_1^{*1}	1.4	1.5	1.5	1.6	1.6	1.4
τ_2^{*1}	0	0	0	0	7.4	6.4
A_1^{*1}	0.199	0.240	0.179	0.149	0.184	0.266
A_2^{*1}	0	0	0	0	0.002	0.008
χ^{2*1}	1.46	1.43	1.33	1.50	1.48	1.37
τ_3^{*2}	1.5	1.7	1.5	1.6	1.6	1.8
τ_4^{*2}	0.0	0.0	5.1	0.0	11.1	12.3
A_3^{*2}	0.326	0.440	0.277	0.325	0.398	0.306
A_4^{*2}	0.000	0.000	0.002	0.000	0.004	0.013
χ^{2*2}	1.25	1.72	1.17	2.06	1.32	1.56
x	0.16	0.17	0.16	0.15	0.16	0.16
y	0.11	0.11	0.12	0.13	0.16	0.23

*¹ Emission wavelength is 450 nm

*² Emission wavelength is 525 nm

The results of concentration dependent luminescent properties of **Ln-LBF₂** suggested inter-molecular energy transfer. The inter-molecular energy transfer is occurred by two independent processes, Förster and Dexter processes. Förster process is a fluorescence resonance energy transfer between molecules,. Therefore, energy gap and distance between donor and acceptor and overlap integral between emission spectrum of donor and absorption spectrum of donor are important for this process. In high concentration solution, **Ln-LBF₂** forms aggregation state. As the energy level of S1 state in the aggregation state becomes lower compared to that of isolated state, the energy gap between S1 and T1 becomes smaller (Fig. 53). Therefore, the Förster process is enhanced in the high concentration condition. In the Dexter process, energy transfer is occurred by electron exchange through non-radioactive path. Because the electron exchange is caused by molecular collision, intermolecular distance between donor and acceptor is important. Therefore, the Dexter process is also enhanced with increasing collision probability in the high concentration solution,

From both energy transfer processes; Forster and Dexter processes, the probability of energy transfer is increased in high concentration solution. Hence, **Eu-LBF₂** showed red emission with Em^{BT1} and Em^{Eu} , and **Gd-LBF₂** showed green emission based on Em^{BT1} in high concentration solvent.

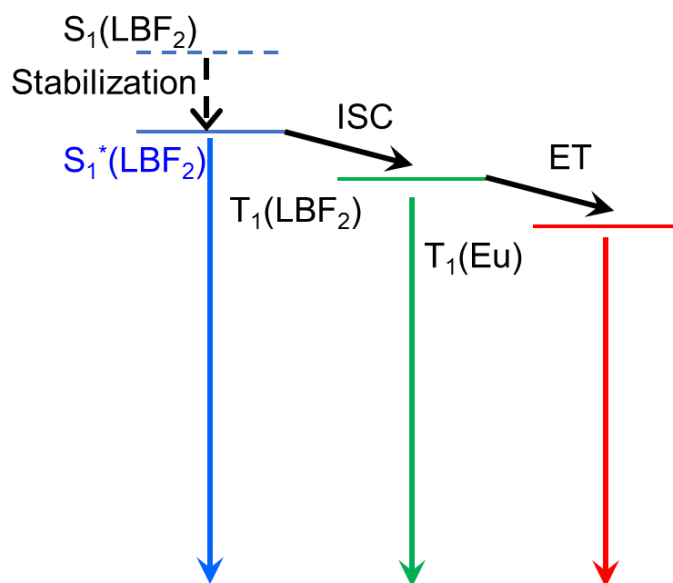


Fig. 53 Energy Diagram of **Eu-LBF₂** in high concentration state.

Guest molecular dependence luminescence of **Eu-LBF₂**

Eu-LBF₂ showed solvent-dependence luminescence properties due to coordination with solvents. From this result, **Eu-LBF₂** should show visible response to guest molecule having metal binding site.

Dichloromethane solution of 200 $\mu\text{mol/L}$ **Eu-LBF₂** was prepared, then 0.1 ml guest molecule was added to 1 ml **Eu-LBF₂** solution. Results of color change were summarized in Table 18. In the cases of alcohol molecules, longer chains enhanced Em^{Eu} . This result investigates that short alcohol form stronger coordination bonds with Eu^{3+} than long alcohol because of steric hindrance.

When phenol substitute was added, **Eu-LBF₂** showed specific emission. **Eu-LBF₂** showed yellow emission. This result suggests that after forming coordination bond, phenol interacts with boron complex, and formed excimer. In fact, solid state of **HLBF₂** also showed yellow emission.

When large steric hindrance molecules such as 2-propanol, or multidentate molecular such as acetylacetone and catechol was added, emission wavelength near 616 nm derived from Eu^{3+} ion was completely disappeared. Furthermore, emission peak derived from **LBF₂** was blue shift. These results indicate that **LBF₂** was removed from Eu^{3+} ion by forming coordination bonds with multidentate or bulky compounds. NMR spectrum of **Eu-LBF₂** in CDCl_3 with 100 μl 2-propanol showed peaks characterized free **HLBF₂**.

Table 18 Guest molecule dependence luminescence of **Eu-LBF₂**

Guest molecules	λ_{LBF_2} /nm	λ_{Eu} /nm	Int _{Eu} /Int _{LBF₂}
1-heptanol	456	615	0.13
1-hexadecanol	466	616	1.06
1-hexanol	459	616	0.22
1-octanol	456	615	0.20
2-chlorophenol	529	616	0.70
2-fluorophenol	528	616	0.59
2-octyl-1-dodecanol	461	616	0.44
2-propanol	445	600	0.00
2-propin-1-ol	449	600	0.01
acetic acid	445	600	0.00
acetophenone	461	616	0.51
acetylacetone	450	601	0.00
arylalchol	456	616	0.08
benzaldehyde	443	616	0.03
benzilalchol	461	616	0.42
valeraldehyde	440	615	0.05
dichloromethane	446	616	1.96
Dioxane	461	616	0.55
DMF	457	616	0.20
DMF-diethylacetal	445	615	0.28
ethanol	458	616	0.21
Furan	473	616	1.48
methanol	455	616	0.05
pentanol	458	615	0.19
phenol	527	616	0.63
p-methoxy acetophenone	467	616	1.11
pyrazol	458	616	0.43
catechol	449	601	0.01

pyrogarol	440	600	0.00
Styrene Oxide	463	616	0.65
THF	461	616	0.38
γ -Resorcylic Acid	441	600	0.01

Next, to investigate the detection limit, 1-10000 equivalents of guest molecules were added to 20 μ mol/L acetonitrile solution of **Eu-LBF₂**. The results showed in Fig. 54-69. When 10000 equivalents of EtOH, DMF, and phenol was added, clear color change was observed. On the other hand, **Eu-LBF₂** showed emission color change when only 1 equivalents of catechol were added. After adding 10000 equivalents of catechol, emission derived from Eu³⁺ was quenched completely. The reason why catechol showed high responsibility color change is coordination ability. Ethanol DMF, and phenol is changed emission color of **Eu-LBF₂** by coordination. Catechol also forms stronger coordination bond with Eu³⁺ than EtOH and DMF because catechol has a bidentate coordination site. Therefore, color change was occurred with small amount of catechol. In addition, when excess amount of catechol was added to **Eu-LBF₂** solution, **LBF₂** was removed from europium ion. By decomposition, Eu³⁺ is quenched due to no antenna effect, but **LBF₂** showed emission in isolation state. Therefore, catechol showed high sensitively emission color change. MeCN solution of **Gd-LBF₂** also showed emission color change from green to blue by adding coordinating guest molecules (Fig. 70-81). From this result, color change with coordinating guest molecules is caused by weakening interaction between lanthanide ion and boron complex, going back ISC forbidden transition.

This color change was achieved by affected each other, Eu³⁺ and boron complexes due to forming coordination bonds. Therefore, this optical property is distinctive features of lanthanide-boron hetero-nuclear complex.

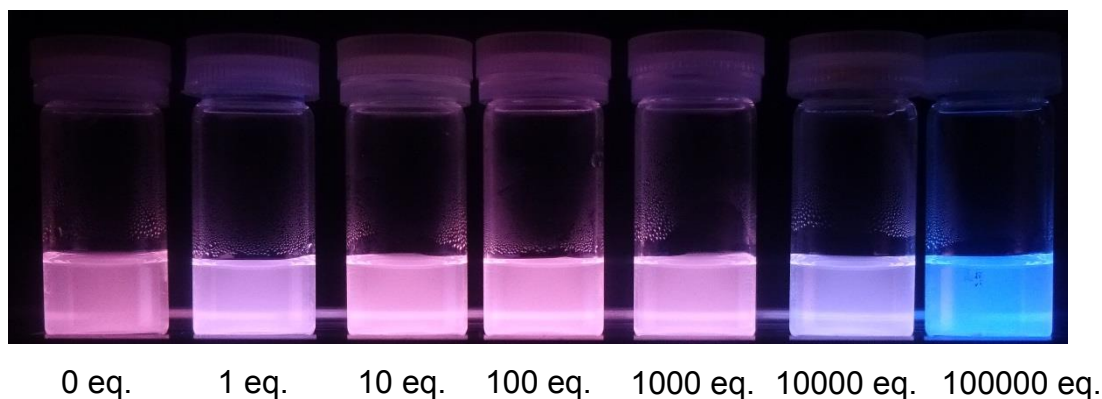


Fig. 54 Under UV irradiation of 20 μ mol/L MeCN solution of **Eu-LBF₂** added

0-100000 equivalent of EtOH

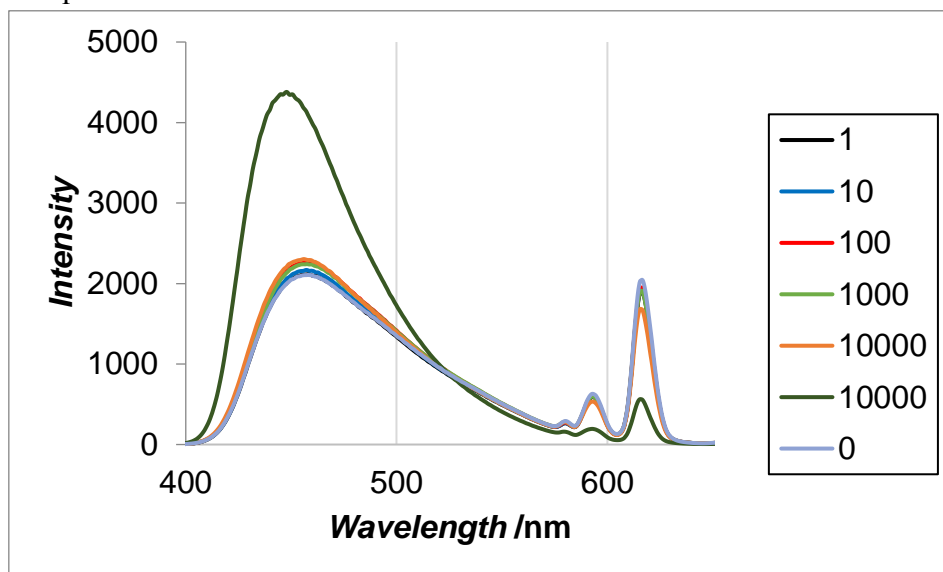


Fig. 55 PL spectra of **Eu-LBF₂** added 0-100000 equivalent of EtOH.

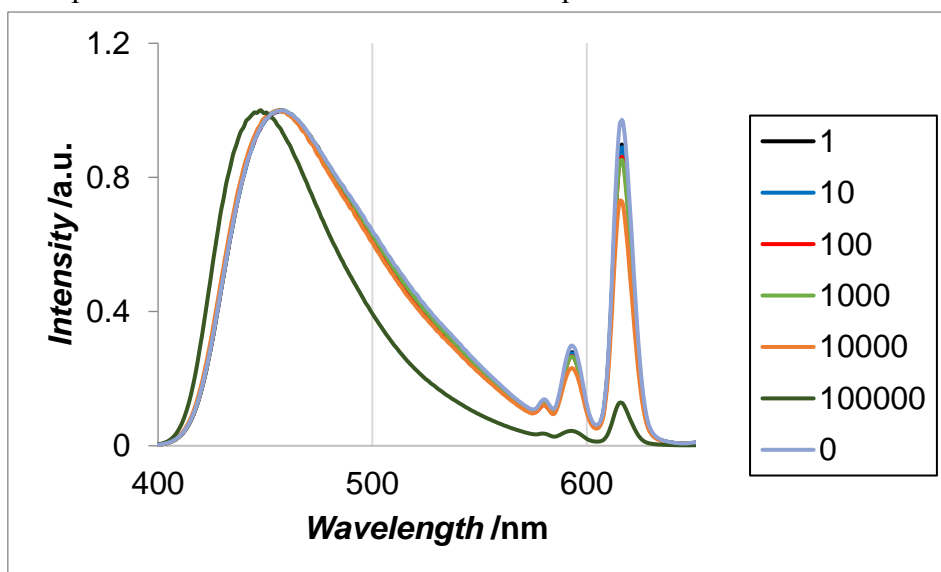


Fig. 56 Normalized PL spectra of **Eu-LBF₂** added 0-100000 equivalent of EtOH.

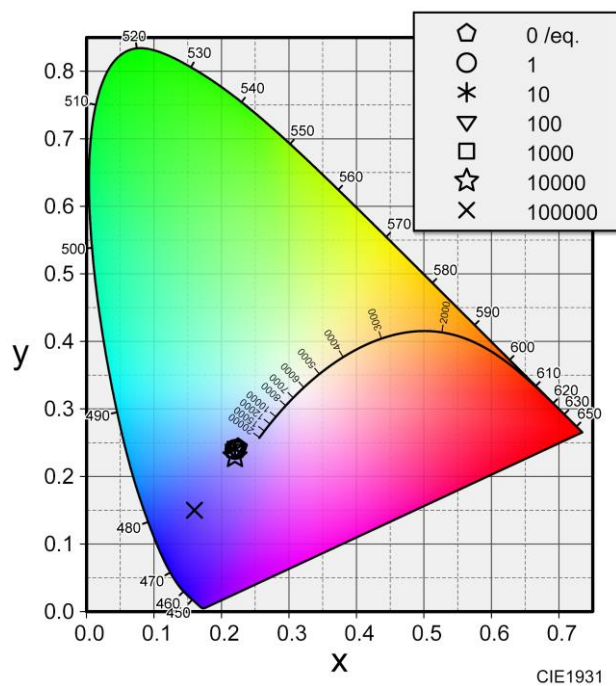


Fig. 57 Color diagram of **Eu-LBF₂** added 0-100000 equivalent of EtOH.

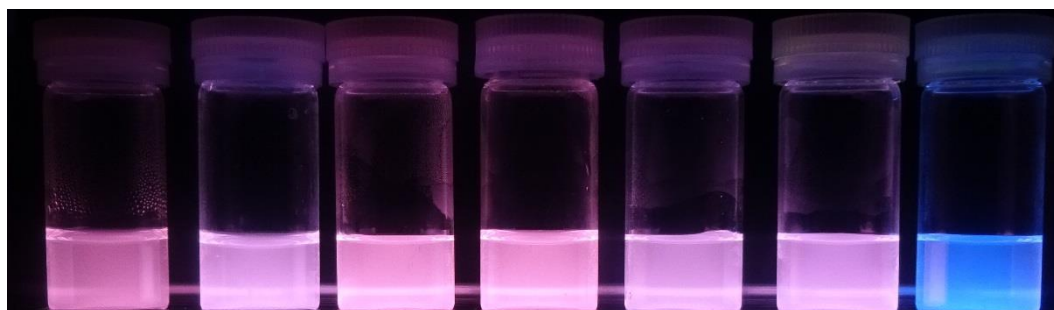


Fig. 58 Under UV irradiation of 20 $\mu\text{mol/L}$ MeCN solution of **Eu-LBF₂** added 0-100000 equivalent of DMF

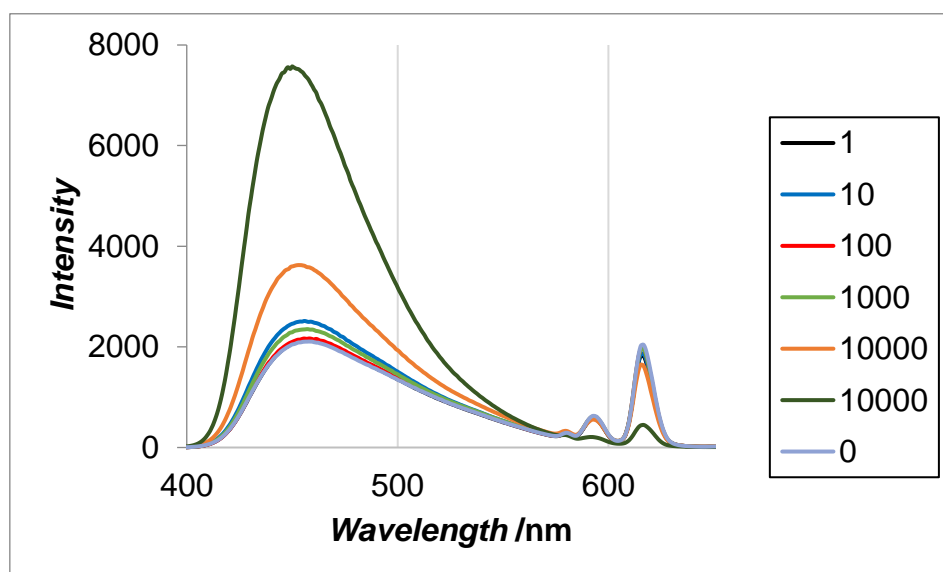


Fig. 59 PL spectra of **Eu-LBF₂** added 0-100000 equivalent of DMF

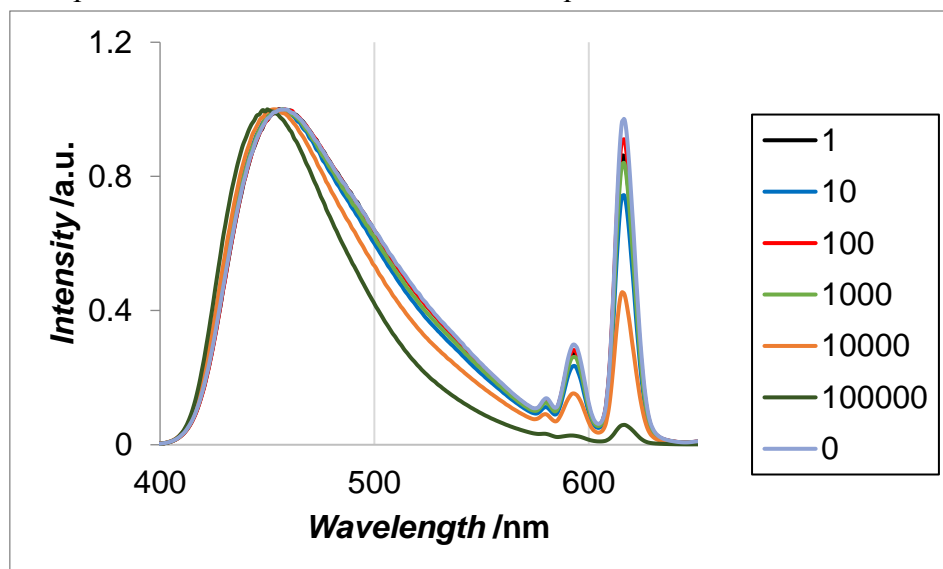


Fig. 60 Normalized PL spectra of **Eu-LBF₂** added 0-100000 equivalent of DMF

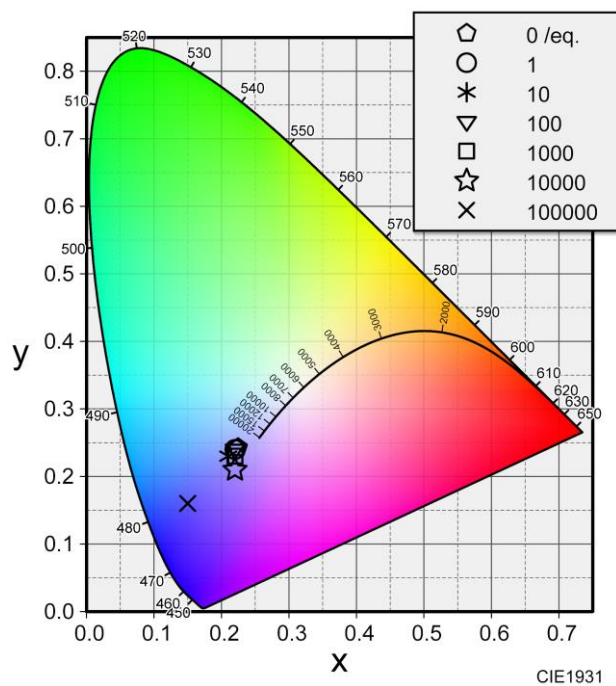


Fig. 61 Color diagram of **Eu-LBF₂** added 0-100000 equivalent of DMF

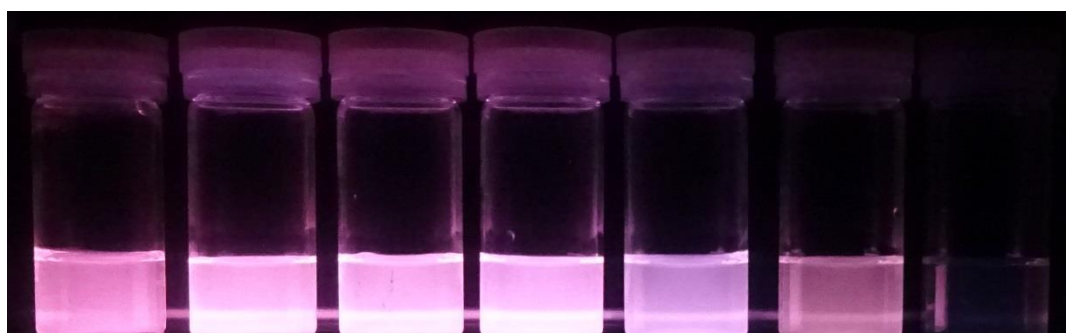


Fig. 62 Under UV irradiation of 20 μmol/L MeCN solution of **Eu-LBF₂** added 0-100000 equivalent of PhOH.

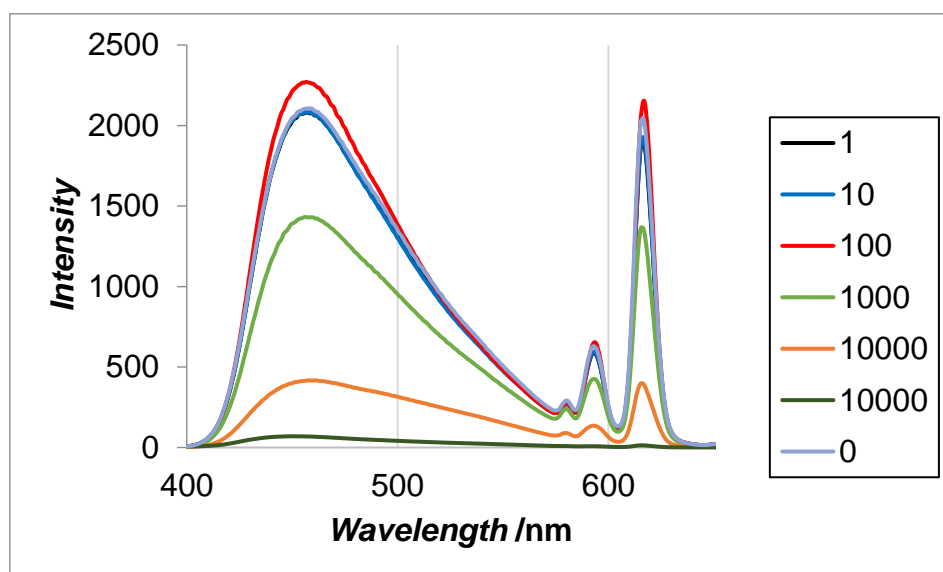


Fig. 63 PL spectra of **Eu-LBF₂** added 0-100000 equivalent of PhOH.

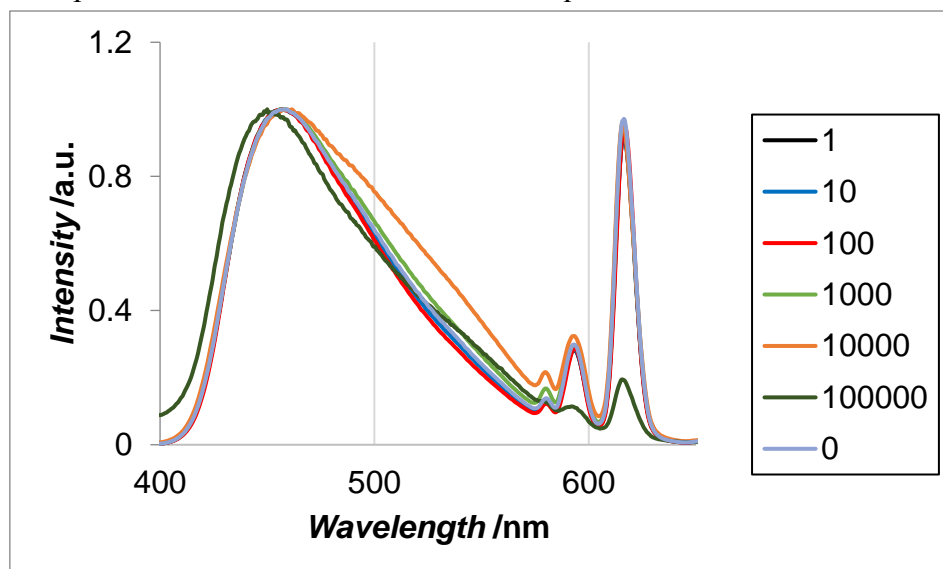


Fig. 64 Normalized PL spectra of **Eu-LBF₂** added 0-100000 equivalent of PhOH.

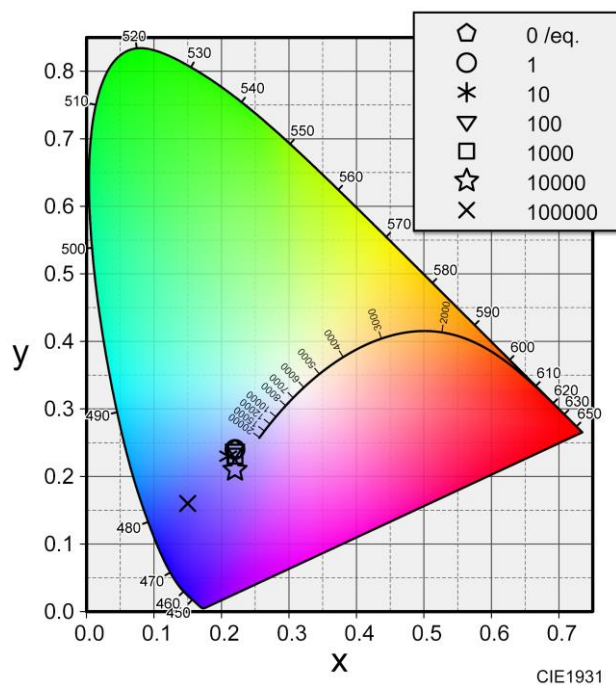
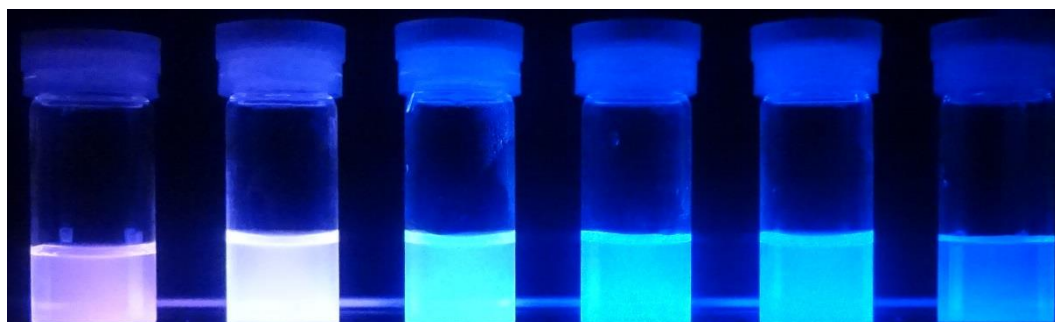


Fig. 65 Color diagram of **Eu-LBF₂** added 0-100000 equivalent of PhOH.



0 eq. 1 eq. 10 eq. 100 eq. 1000 eq. 10000 eq.

Fig. 66 Under UV irradiation of 20 $\mu\text{mol/L}$ MeCN solution of **Eu-LBF₂** added 0-10000 equivalent of catechol.

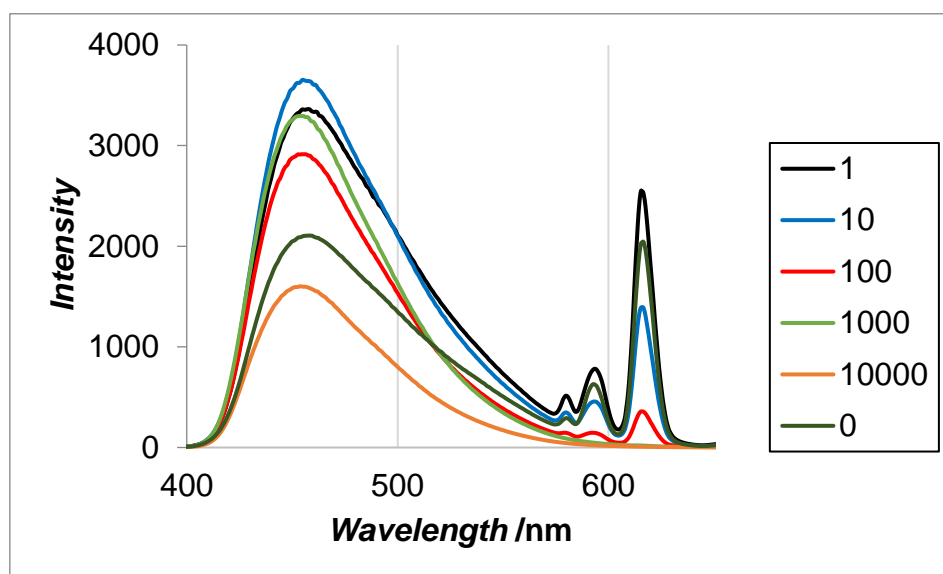


Fig. 67 PL spectra of **Eu-LBF₂** added 0-100000 equivalent of catechol.

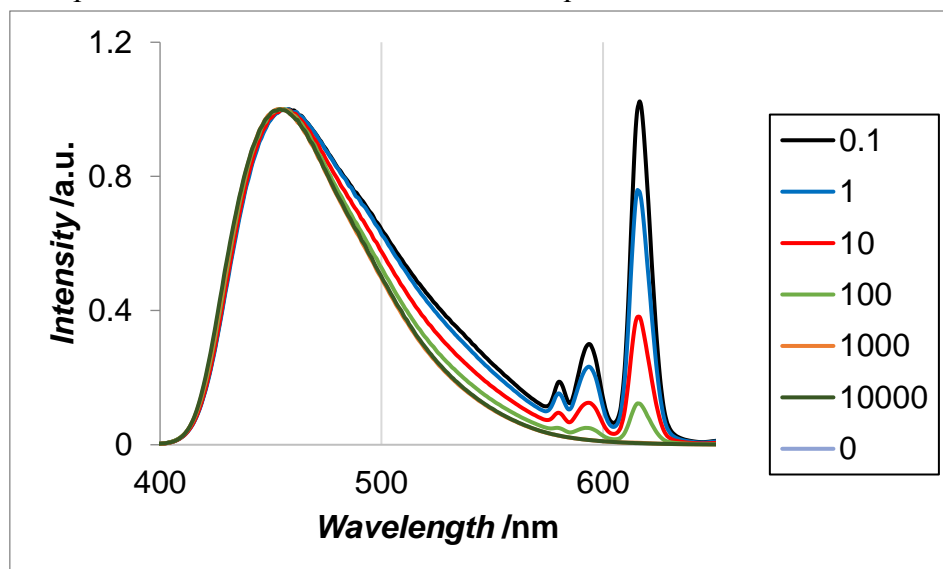


Fig. 68 Normalized PL spectra of **Eu-LBF₂** added 0-100000 equivalent of catechol.

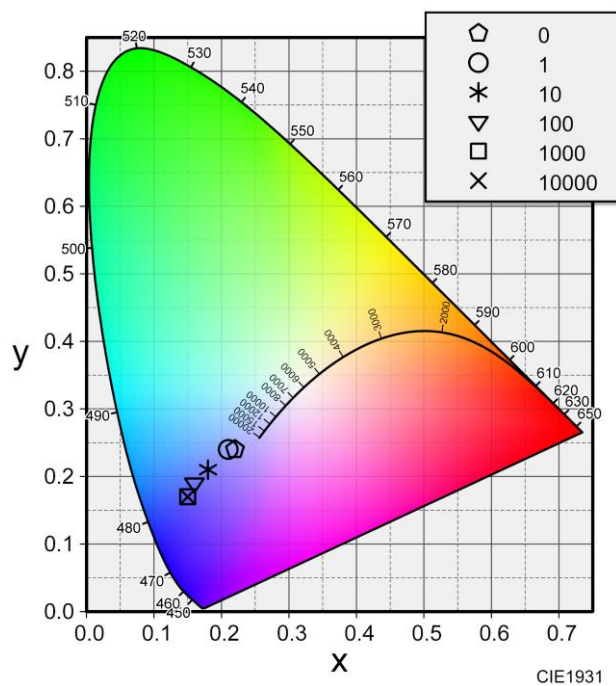


Fig. 69 Color diagram of **Eu-LBF₂** added 0-100000 equivalent of catechol.

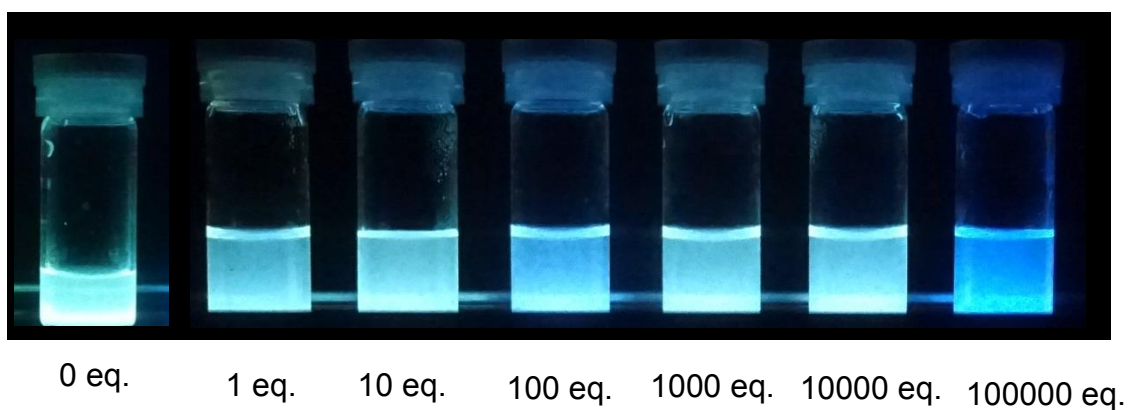


Fig. 70 Under UV irradiation of 20 $\mu\text{mol/L}$ MeCN solution of **Gd-LBF₂** added 0-100000 equivalent of EtOH.

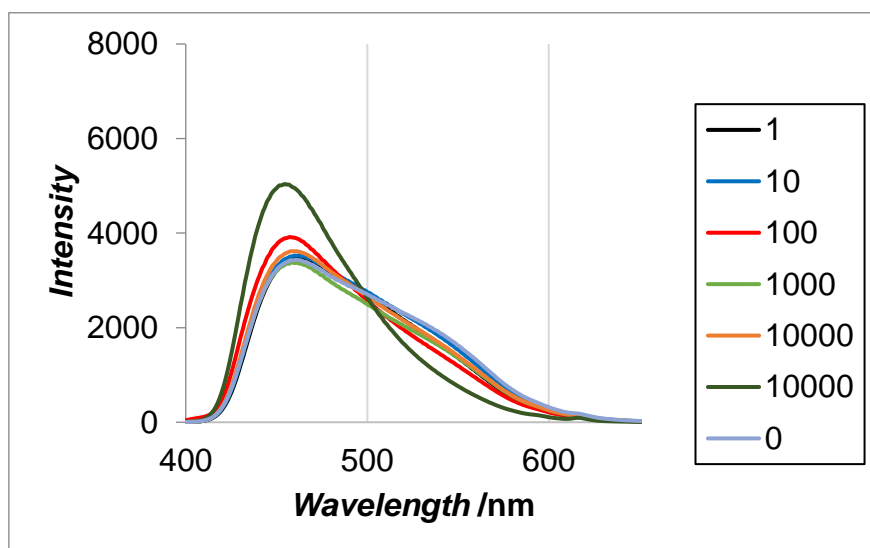


Fig. 71 PL spectra of **Gd-LBF₂** added 0-100000 equivalent of EtOH.

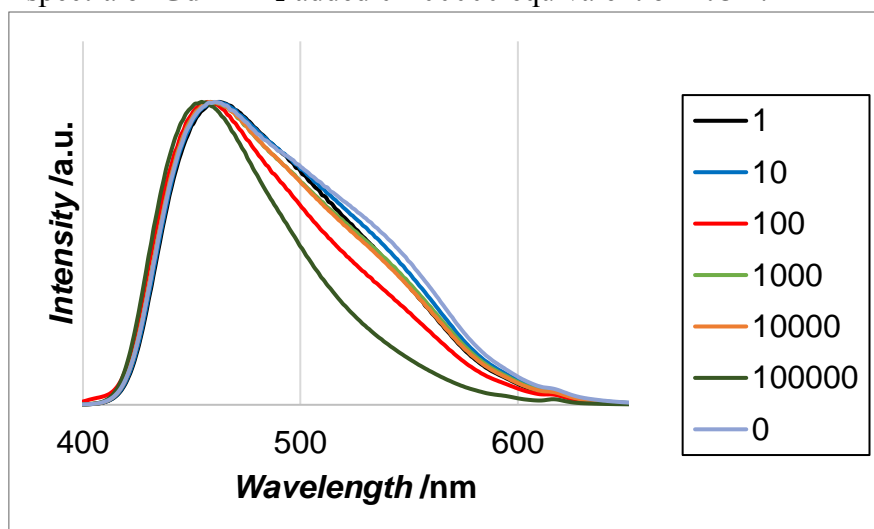


Fig. 72 Normalized PL spectra of **Gd-LBF₂** added 0-100000 equivalent of EtOH.

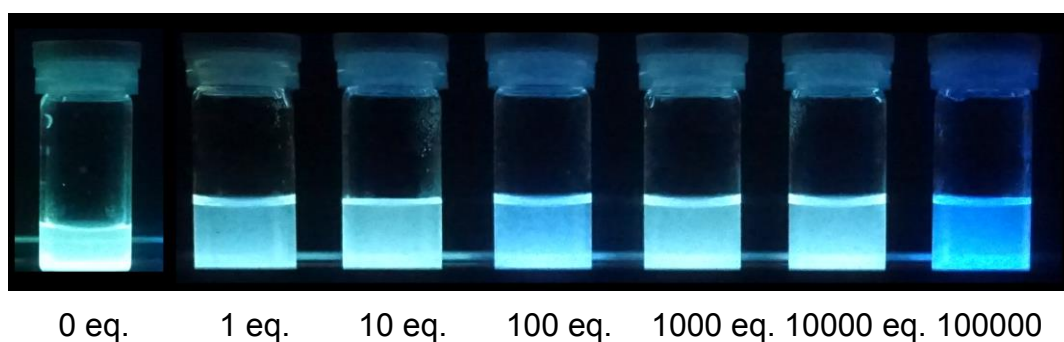


Fig. 73 Under UV irradiation of 20 $\mu\text{mol/L}$ MeCN solution of **Gd-LBF₂** added 0-100000 equivalent of DMF.

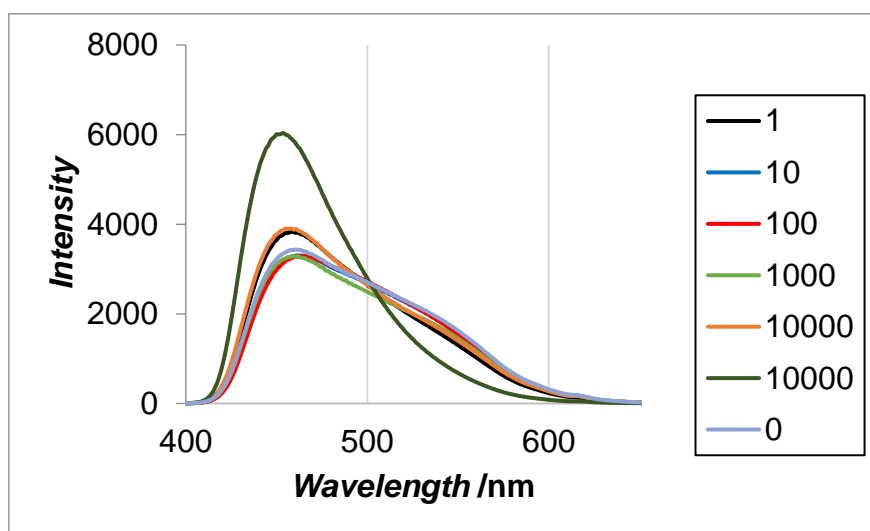


Fig. 74 PL spectra of **Gd-LBF₂** added 0-100000 equivalent of PhOH.

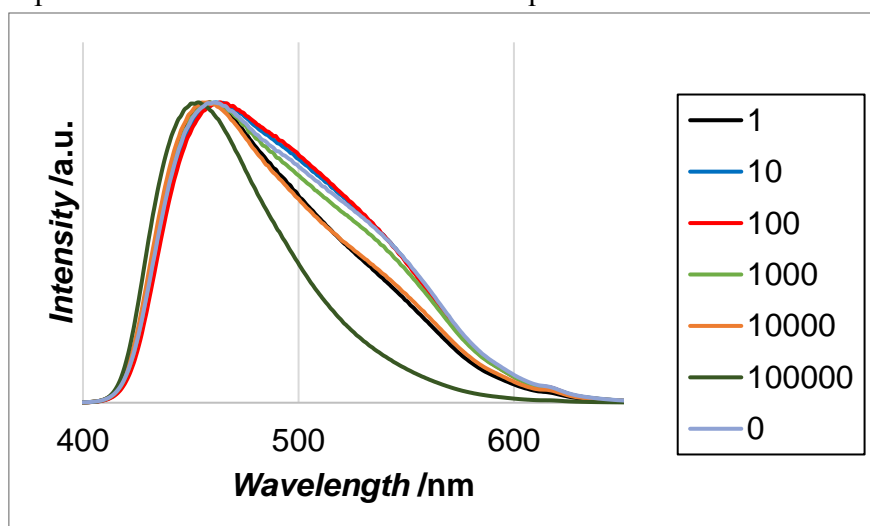


Fig. 75 Normalized PL spectra of **Gd-LBF₂** added 0-100000 equivalent of PhOH.

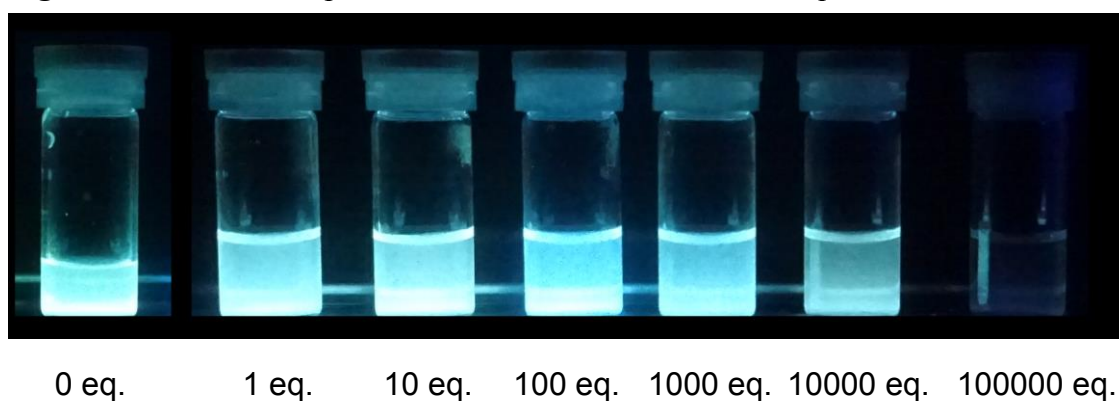


Fig. 76 Under UV irradiation of 20 $\mu\text{mol/L}$ MeCN solution of **Gd-LBF₂** added 0-100000 equivalent of PhOH.

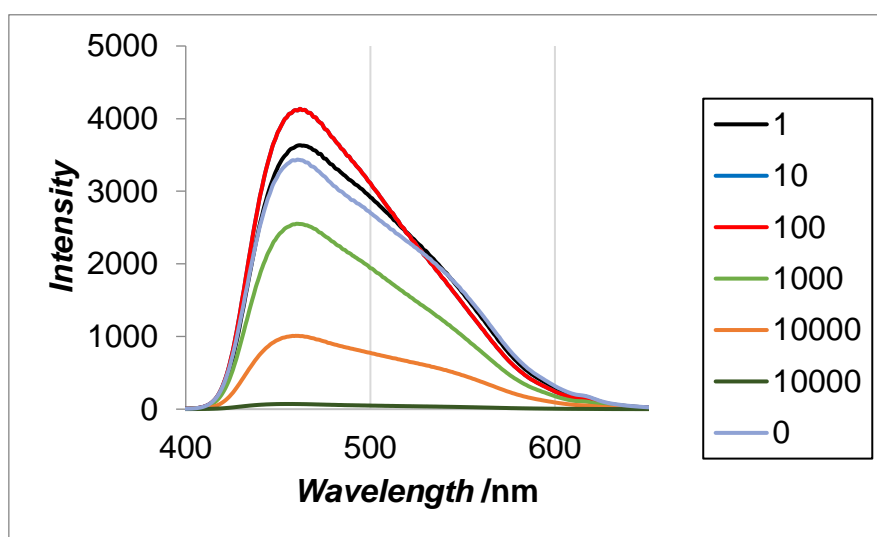


Fig. 77 PL spectra of **Gd-LBF₂** added 0-100000 equivalent of PhOH.

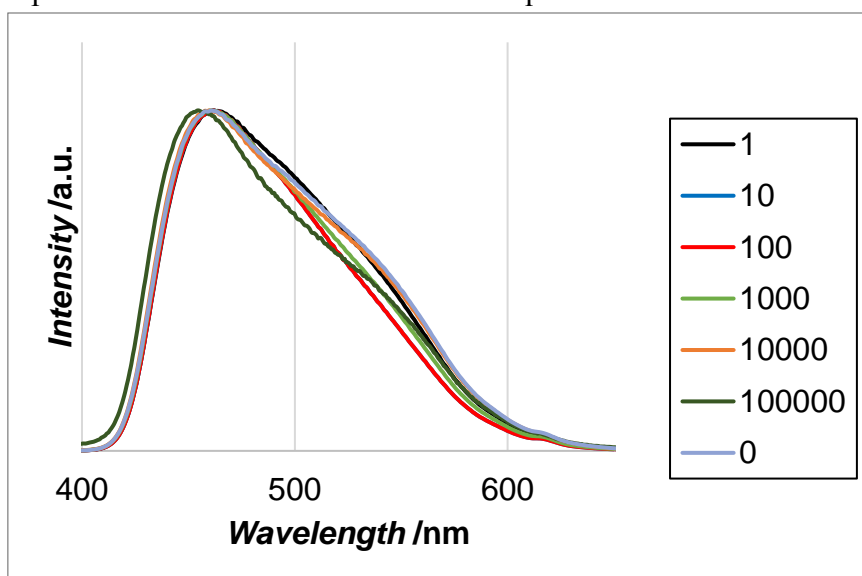


Fig. 78 Normalized PL spectra of **Gd-LBF₂** added 0-100000 equivalent of PhOH.

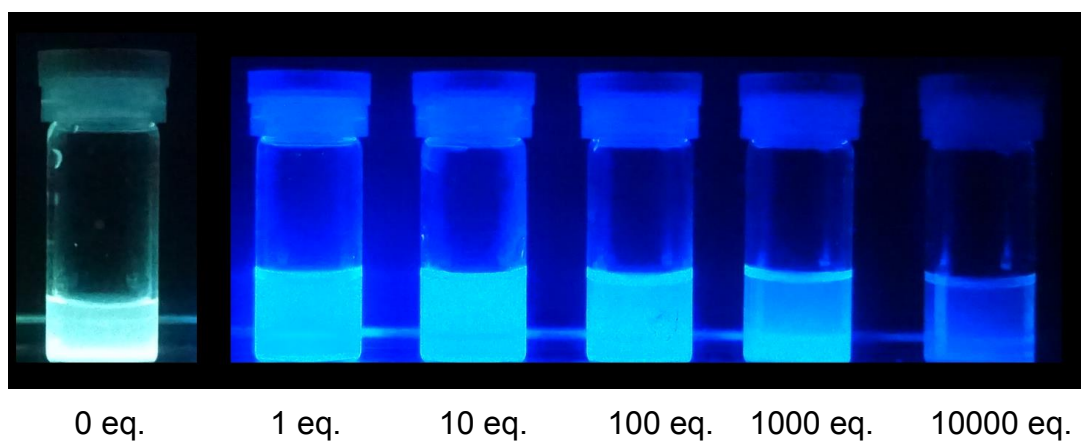


Fig. 79 Under UV irradiation of 20 $\mu\text{mol/L}$ MeCN solution of **Gd-LBF₂** added 0-10000

equivalent of catechol.

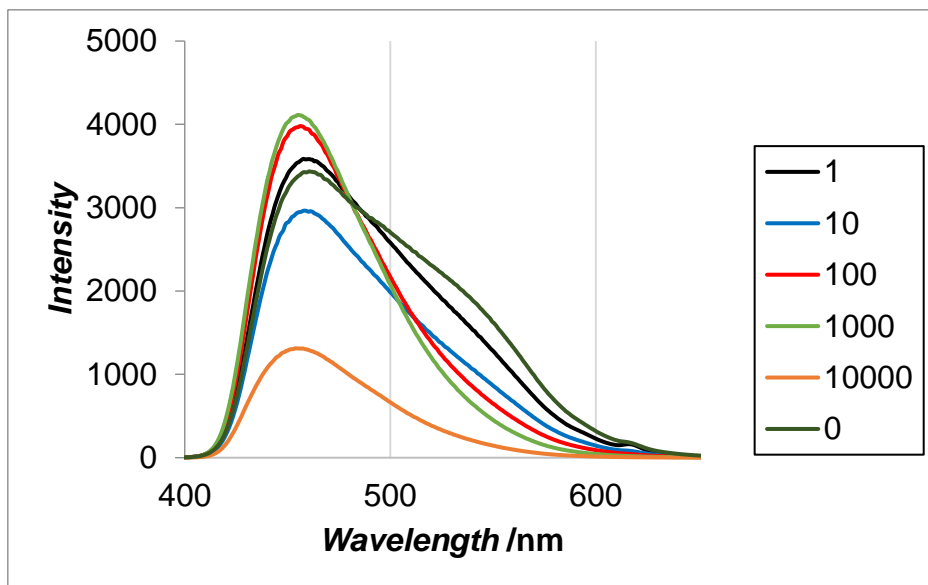


Fig. 80 PL spectra of **Gd-LBF₂** added 0-10000 equivalent of catechol.

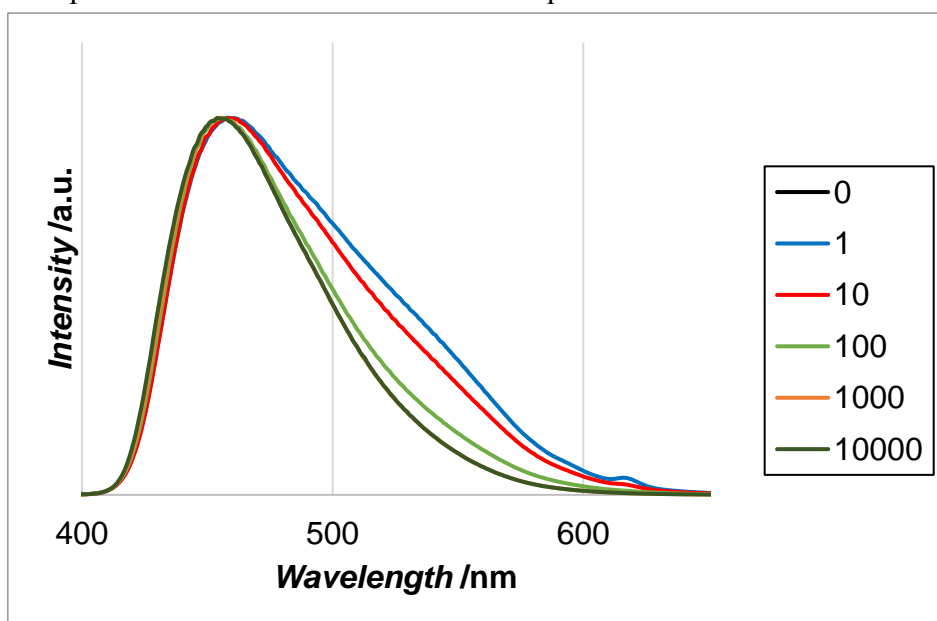


Fig. 81 Normalized PL spectra of **Gd-LBF₂** added 0-10000 equivalent of catechol.

In summary, Coordinative guests interact with **Eu-LBF₂** and change its luminescence properties. To change luminescence properties, effective factors are steric hindrance, strong of coordination ability, and interaction with boron complex.

Conclusion

In summary, novel lanthanide-boron hetero-nuclear complex (**Ln-LBF₂**) was successfully prepared by using boron-complex-ligand **HLBF₂**. **Eu-LBF₂** showed multi-emission originated from Eu(III) ion and boron complex. Furthermore, **Eu-LBF₂** showed solvent dependent luminescent properties based on the coordination ability of solvent. In the cases of non-coordinating solvents, **Eu-LBF₂** showed red emission of Em^{Eu} as a main component. On the other hand, in the cases of coordinating solvents, **Eu-LBF₂** showed blue emission of Em^{BSI} as a main component. The mechanism of solvent dependence was considered with **Gd-LBF₂** as a reference analog. **Gd-LBF₂** showed a new emission band around 525 nm in the non-coordinating solvent. The emission band is attributed to phosphorescent of boron complex (Em^{BT1}). The interaction between boron complex and lanthanide ion relaxed the inter system crossing, which promoted the intra-molecular energy transfer from T1 state of boron complex to T1 state of Eu(III) and enhanced the red emission of Em^{Eu} . This solvent dependence emission was also observed with coordinatable guest molecule in the non-coordinating solution of **Eu-LBF₂**. **Eu-LBF₂** changed emission color from red to blue by addition of guest molecules. Especially, **Eu-LBF₂** sensitively responded to the multi-dentate molecule having strong coordination ability.

The emission color change with high visibility is achieved by the hetero-nuclear complex having different luminescent centers. The emission intensities of each luminescent centers correlate to each other through intermolecular energy transfer, which allows markable emission color change with mixing two emission colors. This concept of multi-emission response is expected to show more interesting stimuli responsible luminescent such as mechanochromism and vapochromism. This is the first trial for construction of the multi-emission hetero-nuclear complex system. To achieve more sensitive sensing with higher visibility, more sophisticated molecular design especially for chromophore, guest interactive site, energy transfer pathway and molecular arrangement are necessary.

Reference

1. M. Mazzeo, V. Vitale, F. Della Sala, M. Anni, G. Barbarella, L. Favaretto, G. Sotgiu, R. Cingolani and G. Gigli, *Adv. Mater.*, 2005, **17**, 34-39.
2. W.-C. Wu, W.-Y. Lee and W.-C. Chen, *Macromol. Chem. Phys.*, 2006, **207**, 1131-1138.
3. T.-R. Chen, *Journal of Molecular Structure*, 2005, **737**, 35-41.
4. J. L. Bricks, A. Kovalchuk, C. Trieflinger, M. Nofz, M. Büschel, A. I. Tolmachev, J. Daub and K. Rurack, *J. Am. Chem. Soc.*, 2005, **127**, 13522-13529.
5. Z. M. Hudson and S. Wang, *Acc. Chem. Res.*, 2009, **42**, 1584-1596.
6. K. Zhang, H. Zhou, Q. Mei, S. Wang, G. Guan, R. Liu, J. Zhang and Z. Zhang, *J. Am. Chem. Soc.*, 2011, **133**, 8424-8427.
7. G. Zhang, G. M. Palmer, M. W. Dewhirst and C. L. Fraser, *Nat Mater*, 2009, **8**, 747-751.
8. K. Miyata, Y. Konno, T. Nakanishi, A. Kobayashi, M. Kato, K. Fushimi and Y. Hasegawa, *Angew. Chem. Int. Ed.*, 2013, **52**, 6413-6416.
9. Y. Kurishita, T. Kohira, A. Ojida and I. Hamachi, *J. Am. Chem. Soc.*, 2010, **132**, 13290-13299.
10. K.-C. Tang, M.-J. Chang, T.-Y. Lin, H.-A. Pan, T.-C. Fang, K.-Y. Chen, W.-Y. Hung, Y.-H. Hsu and P.-T. Chou, *J. Am. Chem. Soc.*, 2011, **133**, 17738-17745.
11. Z. Xie, C. Chen, S. Xu, J. Li, Y. Zhang, S. Liu, J. Xu and Z. Chi, *Angew. Chem. Int. Ed.*, 2015, **54**, 7181-7184.
12. Y. Gong, L. Zhao, Q. Peng, D. Fan, W. Z. Yuan, Y. Zhang and B. Z. Tang, *Chemical Science*, 2015, **6**, 4438-4444.
13. Y. Hasegawa, M. Yamamuro, Y. Wada, N. Kanehisa, Y. Kai and S. Yanagida, *J. Phys. Chem. A*, 2003, **107**, 1697-1702.
14. G. H. Dieke and H. M. Crosswhite, *Appl. Opt.*, 1963, **2**, 675-686.
15. X. Rao, T. Song, J. Gao, Y. Cui, Y. Yang, C. Wu, B. Chen and G. Qian, *J. Am. Chem. Soc.*, 2013, **135**, 15559-15564.
16. Y. Cui, H. Xu, Y. Yue, Z. Guo, J. Yu, Z. Chen, J. Gao, Y. Yang, G. Qian and B. Chen, *J. Am. Chem. Soc.*, 2012, **134**, 3979-3982.
17. J. Rocha, L. D. Carlos, F. A. A. Paz and D. Ananias, *Chemical Society Reviews*, 2011, **40**, 926-940.
18. D. Parker, *Coord. Chem. Rev.*, 2000, **205**, 109-130.
19. S. V. Eliseeva and J.-C. G. Bunzli, *Chemical Society Reviews*, 2010, **39**,

- 189-227.
20. G. Ulrich, R. Ziessel and A. Harriman, *Angew. Chem. Int. Ed.*, 2008, **47**, 1184-1201.
 21. A. Loudet and K. Burgess, *Chemical Reviews*, 2007, **107**, 4891-4932.
 22. A. Kamkaew, S. H. Lim, H. B. Lee, L. V. Kiew, L. Y. Chung and K. Burgess, *Chemical Society Reviews*, 2012, **42**, 77-88.
 23. G. Zhang, J. Lu, M. Sabat and C. L. Fraser, *J. Am. Chem. Soc.*, 2010, **132**, 2160-2162.
 24. H. N. Kim, W. X. Ren, J. S. Kim and J. Yoon, *Chemical Society Reviews*, 2012, **41**, 3210-3244.

Concluding Remarks

In this thesis, the author studied on rational synthesis of oligo-nuclear complexes and their magnetic and photophysical properties. Although numerous oligo-nuclear complexes which showed interesting magnetic, electronic, and luminescent properties have been reported by other groups so far, we developed new method to form oligo-nuclear structure with luminescent properties rationally.

In chapter 1, binuclear complexes $[M_2(HL)_2(NO_3)_2(H_2O)_2]$ (**M₂(HL)₂**; $M^{II} = Mn, Co, Zn$) and octa-nuclear complexes $[M_8(L)_6(\mu_3-O)_2]$ (**M₈L₆**; $M^{II} = Mn, Co, Zn$) were prepared selectively by controlling pH with a linear multidentate type ligand 2,6-di(acetoacetyl)pyridine (H_2L). The binuclear complexes **M₂(HL)₂** were irreversibly transformed to the octa-nuclear ones **M₈L₆** with liberation extra L^{2-} by addition of base. The unique structural conversion yields significant information about the formation process of the cluster structure in solution, which is expected to apply rational design and property control for oligo-nuclear complexes. Such well-designed oligo-nuclear complexes would be a good secondary building units (SBUs) of functional metal-organic frameworks (MOFs).

In chapter 2, new trinuclear lanthanide complexes $[Ln_3L_2(NO_3)_5(MeOH)_4] \cdot nsolv$ (**Ln₃L**; $Ln = La, Ce, Pr, Eu$) were prepared by using the linear multidentate ligand H_2L systematically. **Ln₃L** formed a trinuclear structure in V-shaped arrangement, in which the central Ln(III) has a different coordination environment from the side ones. **Eu₃L** showed quite weak emission, because of deactivation by molecular vibration e.g. C-H oscillators in the ligand. Analogous compound $[Eu_3L^F_2(NO_3)_5(H_2O)_3(MeOH)] \cdot 3MeOH$ (**Eu₃L^F**) using 2,6-di(1,1,1-trifluoroacetoacetyl) pyridine (H_2L^F) showed much stronger emission than **Eu₃L**, in which the C-F bonds contributed to suppress the oscillation. In addition, energy transfer between Eu(III) ions would be another suppressing factor of emission. In the trinuclear complexes, metal ions are located closely, which intrinsically include the energy transfer problem due to metal-to-metal interaction. Hetero-lanthanide complexes would be one of the proposed candidates to solve the energy transfer problem and to withdraw unique luminescent properties of oligo-nuclear system.

In chapter 3, novel lanthanide-boron hetero-nuclear complex $[Ln(LBF_2)_3(solv)_n]$ ($Ln(III) = La, Eu, Gd$; **Ln-LBF₂**) were prepared by a new linear multidentate ligand 3-(3-(4-methoxyphenyl)-3-oxopropanpyl)benzoic acid (H_2L). H_2L formed a boron complex ($HLBF_2$), which was used as a luminescent complex-ligand. **Eu-LBF₂**

provided two luminescent modules, Eu(III) and boron complexes, and showed multi emission property based on the modules. The emission color of **Eu-LBF₂** was changed depending on solvent, concentration, and guest molecules in solution state. The multi-color luminescent **Eu-LBF₂** successfully exhibited guest-dependent color change with high visibility. Comparative studies of emission properties using **Eu-LBF₂** and **Gd-LBF₂** revealed that the well-linked multi-color emission is based on the energy transfer from the excited T1 term of B generated by intersystem crossing to the excited T1 term of Eu(III). The mechanism allows to change the luminescent color with modulating intensity of emissions from excited S1 term of B and T1 term of Eu(III) through the energy transfer from B to Eu(III). The lanthanide-boron heteronuclear complex successfully presented a new concept for multi emission material. This series of compounds are expected to apply for sensing and imaging materials superior in visibility.

These works highlighted rational strategies for controlling structure, increasing luminescent efficiency, and delivering multi-emission with oligo-nuclear complexes, which would give useful information for designing functional, in particular luminescent, oligo-nuclear complexes and significant insight how to link the properties of individual functional modules.

Acknowledgement

The study in this thesis has been carried out under the direction of Professor Masaaki Ohba at during April 2012- March 2018 at the Department of Chemistry, Graduate School of Science, Kyushu University.

The author would like to express the deepest appreciation to Professor Masaaki Ohba for his guidance and encouragement. The author could research liberally in the study due to his generosity. The author could learn a lot of things not only science but also design and thinking faculty for him. The author thanks to Assistant Professor Tomomi Koshiyama for guidance.

The author expresses his gratitude to Professor Hong-Cai Zhou (Texas A&M University) and Dr. Yu Fang (Postdoctoral Researcher of Texas A&M University) for accepting me as visiting scholar and careful guidance, and valuable discussion.

The author would like to thank Advanced Graduate Course on Molecular Systems for Devices. The author was supported his finance for studying abroad, competing meeting by this course. The author could study a lot of things not only science but also business knowledge.

Finally, the author gives a special thanks to all members of Ohba group and Zhou group for their kind support.

Tatsuo Togo
Department of Chemistry
Graduate School of Science
Kyushu University
March 2018

List of Publications

1. Structural Conversion and Selective Synthesis of Di- and Octa-nuclear Mn(II), Co(II) and Zn(II) Complexes

T. Togo, T. Koshiyama, M. Ohba

(accepted to *Chemistry Letters*)

2. Synthesis and Luminescence Properties of Lanthanide Trinuclear Complexes with Linear Multidentate Ligands

T. Togo, T. Koshiyama, M. Ohba

(to be submitted)

3. Synthesis and Multi Emission Properties of Lanthanide-Boron Hetero Complex.

T. Togo, T. Koshiyama, M. Ohba

(to be submitted)

Other Publication

1. Ultra-Small Face-Centered-Cubic Ru Nanoparticles Confined within an Anionic Porous Coordination Cage for Catalytic Dehydrogenation of Ammonia Borane

(Submitted to *Chem*)

(Yu Fang, Jialuo Li, Tatsuo Togo, Fang-Ying Jin, Zhifeng Xiao, LuJia Liu, Hannah Drake, Xizhen Lian, Hong-Cai Zhou)